UNIVERSITAT DE BARCELONA

Hydrodynamic effects on active colloidal suspensions

Eloy Navarro Argemí

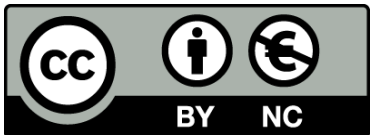

Hydrodynamic effects on active colloidal suspensions

Eloy Navarro Argemí

UNIVERSITAT DE BARCELONA

Hydrodynamic effects on active colloidal suspensions

Memòria per optar al grau de doctor per la Universitat de Barcelona

Programa de doctorat en Física

Autor: Eloy Navarro Argemí

Director: Dr. Ignacio Pagonabarraga

Tutor: Dr. Giancarlo Franzese

UNIVERSITAT DE BARCELONA

Agraïments

"De bien nacidos es ser agradecidos", encara que el meu part va ser complicat i potser algun escodrinyador de tesis alienes acaba decebut amb aquesta secció. Voldria començar-la agraïnt a l'Eduardo Mendive, que ja fa gairebé sis anys va fer-me notar que la facultat tenia més de dos pisos, m'animés a anar parlar amb l'Ignacio Pagonabarraga per veure si em podia dirigir un treballet de màster. En aquell moment no acabava d'estar convençut de què la reunió pogués acabar de manera exitosa, molt menys encara imaginar que la nostra col·laboració s'hagi extès durant tant de temps i s'hagi culminat amb aquesta tesi doctoral.

Durant aquest temps també he pogut treballar amb en Pietro Tierno i la Chantal Valeriani. De la col·laboració amb el primer surten, de manera directa o indirecta, els capítols 2, 3 i 4 de la tesi, mentre que el capítol 5 neix de la col·laboració amb ella. També hem publicat articles plegats, i espero que en surtin més aviat. A més, m'han demostrat la seva voluntat de voler ajudar-me amb el meu futur, quelcom que els agraeixo. També vull mencionar els seus subalterns, amb els que he acabat col·laborant més estretament: en Fernando Martínez i l'Helena Massana del grup d'en Pietro Tierno, i en Francisco Alarcón del de la Chantal Valeriani.

Aquest darrer a part ha estat membre del nostre grup durant molt de temps i hi he compartit despatx durant bona part del doctorat. El seu ajut ha estat cabdal per ensenyar-me a fer el tractament de dades quan n'acumules gigues i gigues, que m'ha sigut d'ajuda no només per al capítol on hem col·laborat conjuntament. En aquest aspecte, també voldria destacar el nom d'en Joan Codina.

Durant aquest doctorat, he pogut fer ús de les instal·lacions del laboratori de física estadística del nostre departament i del súper-ordinador Mare Nostrum del Barcelona Supercomputing Center. En el primer cas, voldria agrair a en Miguel Rubí que em permetés utilitzar el *seu* clúster d'ordinadors, i a en David Reguera i els diferents tècnics que han anat passant, Luis Expósito i Joan Pol Alexandre, el seu manteniment. Al BSC, a part dels milions d'hores de càlcul que hi he emprat i la celeritat del seu servei tècnic a contestar correus electrònics per a qualsevol fotesa, m'agradaria poder-los agraïr tenir un polo blau amb el seu logotip al meu armari, però el mèrit de la seva adquisició correspon a en Dani Gallart.

Voldria fer constar també el suport financer que he rebut durant aquest temps. Agraïnt primer a l'Ignacio Pagonabarraga que m'ajudés a aconseguir alguns contractes durant l'any de màster i el meu primer any aquí per anar fent, i després a la Universitat de Barcelona, que ha finançat tres anys de la meva recerca amb un Ajut al Personal Investigador en Formació.

L'obtenció d'aquesta beca no ha estat exempta de contrapartides *para/con* la universitat en forma d'hores de docència. Voldria agraïr a en David Reguera, Matteo Palassini, Federico Mescia, Aurora Hernández, Jordi Soriano, Carmen Miguel, Jaume Casademunt i Joan Codina la seva ajuda en aquests menesters, i al departament la seva comprensió lliurant-me'n durant aquest darrer any.

Seria un oblit imperdonable no mencionar que al nostre departament (primer de Física Fonamental, ara de Física de la Matèria Condensada), comptem amb un equip de secretàries simpàtiques i eficients: l'Olga Tomás, Beatriz Fernández, Elena Pons i Cristina Egusquiza, ara ascendida un parell de pisos més a dalt, que ens fan la vida més fàcil a tothom. Igualment valuosa ha sigut la labor de l'Iván Linares.

Per últim, voldria agraïr el suport d'aquelles persones que han estat amb mi durant aquest temps no perquè fos la seva feina, n'esperessin cap contrapartida o tinguessin la fortuna de compartir temporalment el seu lloc de treball amb mi, sinó per l'afecte i l'amor que ens tenim. Gràcies als meus amics i la meva família.

Contents

Outline of the thesis

The goal of this thesis is studying the role of hydrodynamic effects in systems of active interactive colloids. In order to do so, we have recurred to both numerical simulations, employing the lattice-Boltzmann method, and analytical approaches, introducing dynamic equations for systems of colloids dependent on the flow created by surrounding particles in the system. The systems that have driven our interest are magnetic rotating colloids and patchy squirmers. Both systems are formed by particles that can self-propel and that present anisotropic interactions between them.

These two features are characteristic of *active matter*. In this thesis introduction, we give a brief overview on this field. We also discuss the hydrodynamic interactions the micro-swimmers dealt in this thesis can exert on each other, and introduce the simulation method we have employed.

The means used by magnetic colloids to self-propel are not trivial, as this motion comes from the coupling of the rotation induced by an external magnetic field with a system asymmetry created by an interface in the fluid they are contained in. In chapter 2 we start from the very beginning, describing the origin of the rotation of a single bead submerged in a fluid from a torque balance equation, as well as characterize the interactions magnetic colloids are subjected to: magnetic, hydrodynamic and gravitational. We introduce the dimensionless parameters used to estimate the relative importance of these interactions.

Magnetic dipole-dipole interaction tends to align magnetic colloids in arrays. In chapter 3 we introduce several arrays of magnetic colloids that can be observed, and under which conditions, characterized by the parameters introduced in the previous chapter, they are favoured.

One of the most attractive feature of the arrays observed in the previous chapter is that they can form spontaneously in a self-assembly process. In chapter 4 we study this phenomenon by performing a systematic computational study of the different balances of forces at which colloidal suspensions can be subjected to analyse which structures can self-assemble in each scenario.

In chapter 5 we change the system from magnetic colloids to patchy squirmers. We perform another systematic computational study of which conditions are required to self-assemble ordered structures in a quasi two-dimensional (as fluid flows in the third dimension are allowed) suspension of these particles. For this system, the control parameters are the balance between hydrodynamic and

interaction forces, the sign of the interaction between particles (whether they swim with an attractive patch in front of them or in their back) and the kind of flow they create as they self-propel.

Finally, the conclusions and future perspectives are presented in chapter 6.

Chapter 1

Introduction

Facts are stubborn things; and whatever may be our wishes, our inclinations, or the dictates of our passions, they cannot alter the state of facts and evidence.

John Adams

In this introductory chapter, we will provide the reader with the basics on the topics developed through the whole text. We begin by introducing the field of active matter. Active matter is an exciting branch of non-equilibrium physics which is becoming a hot topic of research in recent years. We present the state of the art on the field, by briefly exposing the systems it deals with and the approaches taken to study them, putting more emphasis on active colloidal systems, as they are the object of study in this thesis. Understanding the role of hydrodynamics in this kind of systems is the main goal of this thesis, thus we have added a more fundamental section dealing with hydrodynamics at low Reynold's number, beginning with the very basics of defining what is the Reynold's number and the fundamental equations that describe continuous media, to then introduce the flow created by microswimmers and the basic dynamic equations that describe their motion in a far-field approximation. Finally, there is a third methodological section in which we give a brief overview on the available computational methods to deal with this kind of systems, focusing on the lattice-Boltzmann method we have mainly used.

1.1 Active matter

As Heraclitus of Ephesus (535 BC - 475 BC) put out, *everything changes and nothing stays still*. Universe is ever changing. One of the easiest changes to notice is the variation of the position of a body, what is usually called movement. Explaining movement has been one of the foundational motivations of physics. Newton's laws offer a satisfactory explanation to the movement of a body in our everyday classical world. However, at that very same scale we are surrounded by complex systems, whose movement cannot be described by a simple dynamic equation, but whose properties are the result of the emergent collective behaviour of the many interacting units conforming it.

In figure 1.1 we display some examples of these complex systems. All of them can be labelled as examples of *active matter*. A commonly accepted definition of active matter is that of a system formed by a large number of self-driven units, active particles, capable of systematically transforming internal or ambiental free energy into movement. A defining treat that differentiates active systems from other non-equilibrium examples is that the energy input that drives the system out of equilibrium is local, as each particle individually consumes and dissipates energy in a cycle that usually leads to its self-propulsion, instead of being dragged by a global field.

Collective behaviour is a topic inherently related to active matter. Interactions between its components and the medium surrounding them can give rise to a highly correlated motion of active particles, and the emergence of orientational order in active systems. Active particles can also merge into mesoscopic aggregates, with a large variety of morphologies, from crystals to arrays going through more disordered structures. Other non-equilibrium phenomena that can be studied in active systems are non-equilibrium order-disorder transitions, unusual mechanical and rheological properties, bizarre fluctuation statistics and wave propagation and sustained oscillations even in inertia-free media [Marchetti et al., 2013].

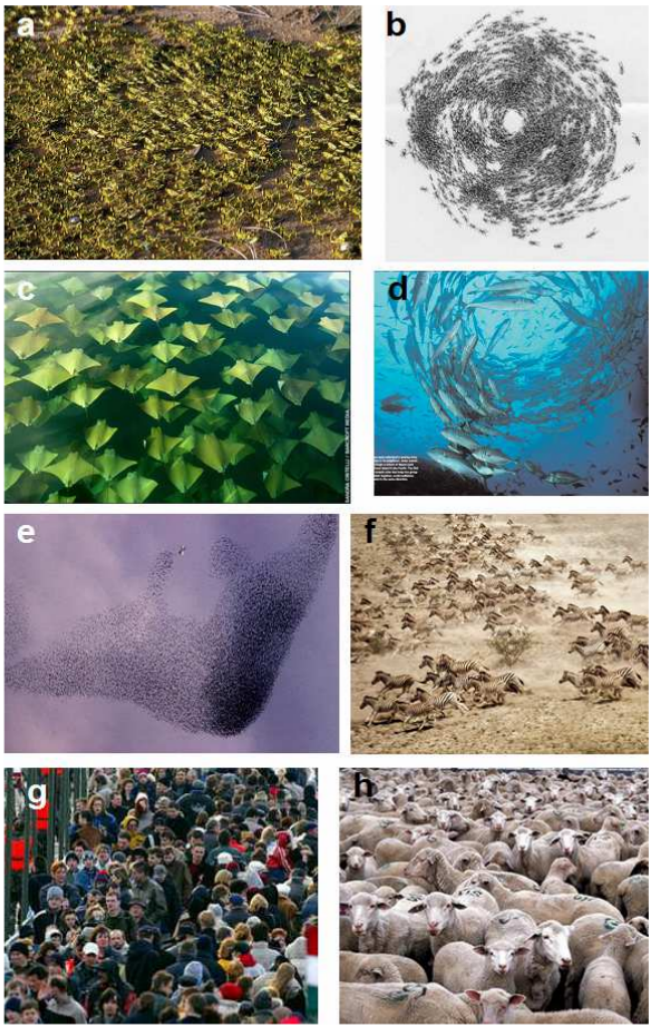

Figure 1.1: Typical gallery with images of collective motion in biological active systems taken from [Vicsek and Zafeiris, 2012]. **(a):** Locusts. **(b):** Ants. **(c):** Manta rays. **(d):** More fish. **(e):** Starlings flying away from a predator. **(f):** Zebras. **(g):** People in crowded urban areas. **(h):** Sheep.

One of the present challenges in the field active matter is obtaining a generic description capable of capturing this full phenomenology. It is reasonable to hope that self-propelled particles, which interact via standard equilibrium forces (attraction, repulsion, alignment, etc.), might form a coherent subclass of non-equilibrium systems that can be described by a common theoretical framework [Cates and Tailleur, 2015]. However, the complexity of active systems and the large number of parameters relevant to their description makes the task specially hard, thus most of the research done is focused on understanding the behaviour of concrete systems. Measuring standard thermodynamic quantities

in active systems, such as pressure, already poses a challenge, as no standard definition for it exists [Takatori et al., 2014, Takatori and Brady, 2015, Solon et al., 2015b, Winkler et al., 2015]. There have also been attempts at determining whether a state equation exists for active systems [Solon et al., 2015a].

Active matter can be classified into *dry* and *wet* systems [Marchetti et al., 2013]. Technically speaking, this classification looks at whether the physical description given to the system conserves momentum (wet) or not (dry). However, as may be deduced by the names given to each case, they are typically used to deal with different kind of physical systems as well.

A dry description of the system focuses more on the interactions between active agents and it is more suitable to describe macroscopic systems. Among the systems that admit this description we can find bacteria gliding in a solid substrate [Wolgemuth et al., 2002], animal herds on land [Toner and Tu, 1998] and several examples of granular particles on a plate [Ramaswamy et al., 2003, Yamada et al., 2003, Aranson and Tsimring, 2006, Narayan et al., 2007, Kudrolli et al., 2008, Deseigne et al., 2010]. This approach has also been used to describe systems that would usually fit into wet active systems [Drescher et al., 2011, Liverpool, 2003]. Besides these examples, the most iconic case of dry systems is given by Vicsek's model [Vicsek et al., 1995]. This minimal model aimed to describe the motion of flocks of birds and schools of fishes, assumes individuals tend to align in the direction of their neighbours. It is controlled only by two parameters, particle density and noise to this alignment rule, and predicts an order-disorder phase transition. While Vicsek's model is more suitable to describe macroscopic systems, there are dry models aimed at describing active matter at the microscopic scale. The two main models for this task are *run and tumble* [Schnitzer, 1993] and *active brownian particles* (ABP) [Romanczuk et al., 2012]. Run and tumble is motivated to describe bacteria like *Escherichia coli*. It assumes the particle displaces alternating straight and constant velocity runs with instantaneous tumbles in which it instantaneously changes its orientation randomly. For ABP, velocity smoothly decorrelates via rotational diffusion. This rotation is typically thermal, hence the Brownian label. At long time and length scales both models lead to diffusive motion.

On the other hand, for wet systems solvent mediated hydrodynamic interactions are also important, thus the dynamics of the suspending fluid must be incorporated explicitly to the model. Momentum must be conserved in the composite system of active particles and surrounding fluid. Phenomena like bacterial turbulence [Dombrowski et al., 2004] or the emergence of a new phase "zooming bionematic" (similar to a nematic liquid crystal, but for bacillus) [Cisneros et al., 2007] can be explained with this approach. From a more theoretical point of view, the main goal of the wet description is studying the concrete role of hydrodynamic interactions in systems of microswimmers. In this regard, we would like to bring up the squirmer model to describe swimming motion (see section 1.2.7 for further details). Our group has an extensive experience performing simulations with microswimmers modelled as such using the lattice-Boltzmann method (see section 1.3 for a method description) [Llopis and Pagonabarraga, 2010, Pagonabarraga and Llopis, 2013, Alarcón and Pagonabarraga, 2013, Alarcón et al., 2017], and we may add a new example in chapter 5 of this thesis. We should

highlight the work of Ishikawa and Pedley as the pioneers at computationally implementing this model (using Stokesian dynamics), beginning with the study of hydrodynamic interactions between two squirmers [Ishikawa et al., 2006], and extending it to suspensions in three [Ishikawa and Pedley, 2007, Ishikawa et al., 2008] and two dimensions [Ishikawa and Pedley, 2008].

Comparatives of ABP results with models with explicit solvent dynamics are recurrent. ABP predicts a motility induced phase separation (known as MIPS) [Cates and Tailleur, 2015]. Similar results can be found at low concentration of particles [Llopis and Pagonabarraga, 2006, Ishikawa and Pedley, 2008], but hydrodynamic interactions hinder the formation of finite size aggregates at high concentrations [Matas-Navarro et al., 2014, Zöttl and Stark, 2014].

As we have seen, active matter is a transversal field intimately related to biology. In this regard, an alternative classification between *live* and *artificial* systems is possible. Colloidal systems are the paradigmatic example among artificial swimmers. Colloidal suspensions are defined as multiphase materials in which a solid phase, consistent of micrometric particles, is dispersed into a fluid phase. Several biological fluids, such as milk and blood, are actually colloidal suspensions, and they also have many applications in many fields of industry and technology [Aranson, 2013]. Colloidal suspensions can self-assemble into a large variety of morphologies, from disordered glasses, to gels and colloidal crystals. Out of equilibrium suspensions offer advantages over their equilibrium counterpart, as the formed structures can self-propel [Dreyfus et al., 2005, Tierno et al., 2008, Martinez-Pedrero et al., 2015], self-repair [Kumacheva et al., 2003, Osterman et al., 2009] and be used to manipulate other bodies [Snezhko and Aranson, 2011, Massana-Cid et al., 2017]. In order to displace colloids, colloidal suspensions may be subjected to an external field or have self-propelling units. In the former case, colloids may be driven by an electric or magnetic field, or by hydrodynamic flows, which exert a force or torque directly on the particles. As for the later case, particles are usually driven by chemical reactions, which create local force dipoles responsible of their self-propulsion [Aranson, 2013].

Among the methods available to displace colloids in a suspension, we would like to highlight a few examples. Acoustic fields can be used as a non-invasive way of manipulating particles suspended in a fluid. The study of incompressible particles under the effect of acoustic fields dates back to 1934 [King, 1934]. The analogous study for compressible particles was presented in [Yosioka and Kawasima, 1955], and a general theory summarizing both cases in [Gor'kov, 1962]. More recently, Bruus introduced a second-order theory [Settnes and Bruus, 2012] to explain the emergence of acoustic radiation forces. A particle in a fluid in which there is an applied acoustic wave will scatter the incoming flow (figure 1.2 (a)). The interference of the incoming wave ϕ_{in} with the scattered flow ϕ_{sc} gives rise to an effective force $\vec{F}^{rad}$, which can either attract or repeal particles from the wave nodal planes depending on their compressibility, characterized by a parameter Φ (figure 1.2 (b)). New pizoelectric materials, which can be coupled to microfluidic devices to create acoustic waves in them, have motivated the interest in the applications of this phenomenon.

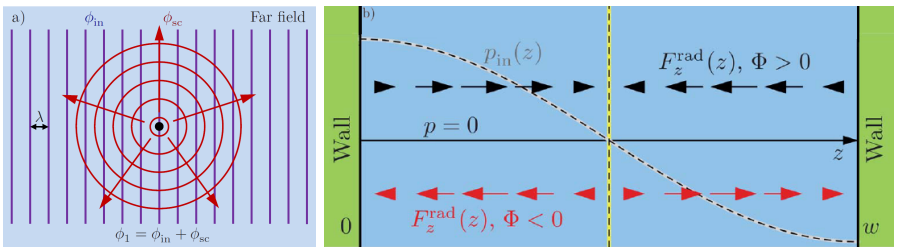

Figure 1.2: **(a)**: Sketch of the far-field scattering of an incoming acoustic wave ϕ_{in} (blue lines) of wavelength λ by a small particle (black dot) with radius $a \ll \lambda$, leading to the outgoing scattered wave ϕ_{sc} (red circles and arrows). **(b)**: Cross-sectional sketch of a straight, hard-walled (green) water-filled channel (blue) of width w with a transverse standing ultraound $\lambda/2$-pressure resonance $p_{in}(z) \propto \cos(kz)$ (grey dashed line). Radiation force $F_z^{rad}(z)$ period is doubled. For $\Phi > 0$, $F_z^{rad} \propto \sin(2kz)$ (black arrows), and for $\Phi < 0$, $F_z^{rad} \propto -\sin(2kz)$, which leads to motion towards and away the nodal plane (yellow dashed line), respectively. Figures taken from [Bruus, 2012].

The use of magnetic fields is another non-invasive technique for particle manipulation. In this case we do not need to directly perturbate the fluid, thus making the experimental set-up simpler and offering more possibilities than acoustic fields, with the drawback of being limited to dealing with colloids possessing a magnetic moment, be it permanent (ferromagnetic) or induced by the field (paramagnetic). In both cases, magnetic moments tend to couple to applied external fields. Oscillatory fields can be used to directly apply torques to magnetic colloids. A magnetic rotor in a fluid creates a vortical flow around itself, which can be used to self-propel or to propel surrounding passive particles. Anisotropy is very present in magnetic systems. It can come from particle anisotropy (due to non-spherical shape, preferred directions of magnetization due to their crystalline structure or an inhomogeneous composition), as well as the directional magnetic dipole-dipole interaction between magnetic moments [Tierno, 2014]. Chapters 2, 3 and 4 are dedicated to this topic and we will deal with it more thoroughly there.

Finally, among the examples of self-propelled artificial swimmers, Janus particles deserve a special mention. Janus swimmers are colloids with two faces with differentiated physical and/or chemical properties. This difference can lead to the appearance of local gradients of pressure, electrical charge, chemical potential, etc., which eventually leads to the self-propulsion of the particle. In [Paxton et al., 2006, Paxton et al., 2004], it is reported that rods half made of gold and platinum submerged in hydrogen peroxide can self-propel by self-induced electrophoretic flow powered by the catalytic decomposition of hydrogen peroxide at the gold-platinum junction. Polystyrene beads coated with platinum and also submerged in hydrogen peroxide can self-propel as well due to the gradient of osmotic pressure due to the inhomogeneous reduction of hydrogen peroxide into water and oxygen at both sides of the particle [Howse et al., 2007]. Similar chemical reactions can be induced to photosensitive colloids [Palacci et al., 2013], now catalysed by the application of light to the suspension.

Janus was the Roman god of duality. However, he made it into physics through colloidal science instead of quantum mechanics.

1.2 Hydrodynamics at low Reynolds' number

Wet active matter is characterized by the interaction of its components with the medium surrounding them. Usually, this medium is a fluid. In this section, we will give a description of fluids as continuous media. We will introduce the basic equations that describe the basic properties of a fluid, *i.e.* the time evolution of its velocity, pressure, and density fields. The former two are given by the Navier-Stokes equation, which can be rewritten in a dimensionless form that depends only on a dimensionless parameter called the Reynolds' number. Besides that, the Reynolds' number has a deeper physical meaning, allowing us to distinguish between turbulent and laminar flows, being the later the ones we are interested in and we will focus on. Once we know the mechanical properties of a fluid, we will be able to introduce hydrodynamic interactions. The origin of this interaction lies on the fact that the presence of a particle in a fluid distorts the flow around it, which in turn affects neighbouring particles. We will introduce the basic flows created by the kind of swimmers we will deal with in the following chapters, and how these flows are distorted in the presence of a solid interface. Finally, we will introduce the dynamic equations for a system of swimmers hydrodynamically interacting in a far-field approximation.

1.2.1 Fluids as continuous media

A fluid is a material whose shape can vary due to the effect of applied forces or stresses. Even though at the molecular scale fluids are just a collection of molecules, they can be described through a continuous approach, which treats them as a material characterized by a velocity, pressure and density fields. The basic equation that describes the behaviour of fluids is the *Navier-Stokes* equation, which is the equivalent of Newton's law for discrete bodies.

The equations that describe a fluid are associated to conservation laws of mass, energy and momentum. In a general form, a conserved quantity $\phi(\vec{x})$[1]

[1]It may be either scalar or a vector.

given by the integral of its density over a volume $\int_V \phi dV$, will follow a continuity equation:

$$\frac{\partial \phi}{\partial t} + \vec{\nabla} \cdot (\phi \vec{u}) + s = 0 \tag{1.1}$$

where $\vec{u}$ is the flow velocity and s accounts any possible sources of this quantity. When integrating equation (1.1) over a volume, we can infer that the variation of this quantity in the volume will be given by its flow through it and the sum of what is generated by any source inside it. We can replace the generic ϕ for the mass density ρ to deal with mass conservation:

$$\frac{\partial \rho}{\partial t} + \vec{\nabla} \cdot (\rho \vec{u}) + s = 0 \tag{1.2}$$

Most of the fluids we will be dealing with in this thesis will be liquids (water mainly), which is highly incompressible, *i.e.* even if it flows its density remains constant in its whole volume. Applying this condition to equation (1.1), and considering a case with no sources of fluid, we obtain the incompressibility condition:

$$\vec{\nabla} \cdot \vec{u} = 0 \tag{1.3}$$

Dealing with incompressible fluids does not only simplifies the problem at shortening the equations, but will also make unnecessary a state equation that relates pressure and density in the fluid.

When applying the continuity equation (1.1) to momentum conservation, we recover Newton's second law for continuous media.

$$\rho \left[\frac{\partial \vec{u}}{\partial t} + \vec{u} \cdot \vec{\nabla} \vec{u} \right] = \vec{f} \tag{1.4}$$

where the force density $\vec{f}$ acts as the source of momentum, and we have already considered an incompressible medium, thus ρ is constant. Forces can be divided in external body forces, such as gravity, and internal surface forces. The later can be expressed in terms of the stress tensor $\boldsymbol{\sigma}(\vec{x}, t)$. The internal force on a fluid volume is given by integrating the stress tensor over the volume's surface ∂V:

$$\vec{F}^{int} = \oint_{\partial V} \boldsymbol{\sigma}(\vec{x}, t) \cdot d\vec{S} = \int_V \vec{\nabla} \cdot \boldsymbol{\sigma}(\vec{x}, t) dV \tag{1.5}$$

where the Gauss' theorem has been used to obtain the second equality. Hence, the internal force density is simply:

$$\vec{f}^{int} = \vec{\nabla} \cdot \boldsymbol{\sigma} \tag{1.6}$$

The stress tensor can be divided into an isotropic contribution, which is proportional to the fluid pressure, and a non-isotropic one, which depends on the deformation rate of the fluid, characterized by the strain tensor $\boldsymbol{e}$; it depends on the molecular structure of the fluid. For simple fluids, among which we

can include water, there is a linear relation between $\boldsymbol{\sigma}$ and $\boldsymbol{e}$; they are called *Newtonian* fluids. In that case, the stress form is:

$$\boldsymbol{\sigma} = -p\hat{\mathbf{1}} + 2\eta\boldsymbol{e} \tag{1.7}$$

with $\boldsymbol{e} = \frac{1}{2}\left(\nabla\vec{u} + (\nabla\vec{u})^T\right) - \frac{1}{3}(\vec{\nabla}\cdot\vec{u})\hat{\mathbf{1}}$ in its most general form.

Combining (1.7) with (1.4), the Navier-Stokes equation for an incompressible Newtonian fluid can be written:

$$\rho\frac{\partial\vec{u}}{\partial t} = -\vec{\nabla}p + \eta\nabla^2\vec{u} + \vec{f}^{ext} \tag{1.8}$$

1.2.2 Deriving Navier-Stokes from Boltzmann's equation

We have derived the Navier-Stokes equation for an incompressible Newtonian fluid using a continuous description of the fluid and applying conservation principles. Navier-Stokes equation can also be derived from a more microscopic approach: the *Boltzmann equation*. The Boltzmann equation deals with the distribution function $f(\vec{x},\vec{v},t)$, which describes the fraction of fluid particles moving at velocity compressed between $\vec{v}$ and $\vec{v}+\delta\vec{v}$ at a position between $\vec{x}$ and $\vec{x}+\delta\vec{x}$ at a time between t and $t+\delta t$. Distribution f represents the density of a conserved quantity, the number of particles N, hence it follows a continuity equation (1.1), using f as ϕ and $\vec{w} \equiv (\vec{v},\dot{\vec{v}})$ instead of $\vec{u}$ (because f is a phase-space $(\vec{x},\vec{v})$ function, and not just a physical space $\vec{x}$ function):

$$\frac{\partial f}{\partial t} + \vec{\nabla}\cdot(f\vec{w}) + s = 0 \tag{1.9}$$

with the ∇ operator acting on the six components of the phase space.

If we develop the second term in this equation, we can simplify it until getting the well-known Boltzmann equation.

$$\frac{\partial f}{\partial t} + \vec{v}\cdot\vec{\nabla}f + \frac{\partial\vec{v}}{\partial t}\cdot\frac{\partial f}{\partial\vec{v}} + s = 0 \tag{1.10}$$

In this case, the source term s does not only include the spontaneous creation or annihilation of particles, but also collisions between particles, accounted in a term expressed as $-\left(\frac{df}{dt}\right)_{collisions}$. Collisions are responsible of discontinuities in the phase space due to sudden changes of velocity and that is why they must be counted apart.

We can compute momenta from the distribution function f to obtain some interesting continuous fields we saw in the previous section. The general procedure will be integrating the product of a function $Q(\vec{v})$ times the distribution function $f(\vec{x},\vec{v},t)$ to obtain a function $\phi(\vec{x},t)$ which represents a continuous density field. Three of the most common $Q(\vec{v})$ are 1, m and $m\vec{v}$, from which we obtain the particle density $n(\vec{x},t)$, mass density $\rho(\vec{x},t)$ and momentum flux density $\rho(\vec{x},t)\vec{u}(\vec{x},t)$, respectively, with $\vec{u}(\vec{x},t) = \langle\vec{v}(\vec{x},t)\rangle$.

$$\begin{aligned} n(\vec{x},t) &= \int f(\vec{x},\vec{v},t)d^3\vec{v} \\ \rho(\vec{x},t) &= \int mf(\vec{x},\vec{v},t)d^3\vec{v} \\ \rho(\vec{x},t)\vec{u}(\vec{x},t) &= \int m\vec{v}f(\vec{x},\vec{v},t)d^3\vec{v} \end{aligned} \tag{1.11}$$

By multiplying the Boltzmann equation (1.10) by a function $Q(\vec{v})$ and integrating it we can obtain equations that describe the conservation of the quantities whose density is given by $\phi(\vec{x},t)$. The general procedure will look like this:

$$\int Q(\vec{v})\left[\frac{\partial f}{\partial t} + \vec{v}\cdot\vec{\nabla}f + \frac{\partial \vec{v}}{\partial t}\cdot\frac{\partial f}{\partial \vec{v}}\right]d^3\vec{v} = \int Q(\vec{v})\left(\frac{df}{dt}\right)_{col} d^3\vec{v} \tag{1.12}$$

For the $Q(\vec{v})$ we have listed, the right term of this equation is zero. They are called *collisional invariants*. The number of particles, their mass and their momentum are conserved in collisions. We can now integrate separately each term of the remaining integral to obtain the following equation:

$$\frac{\partial}{\partial t}n\langle Q\rangle + n\vec{\nabla}\cdot\langle Q\vec{v}\rangle - \frac{\partial \vec{v}}{\partial t}n\left\langle\frac{\partial Q}{\partial \vec{v}}\right\rangle = 0 \tag{1.13}$$

It is pretty straightforward to obtain continuity equation (1.2) replacing $Q(\vec{v})$ for m. Using $m\vec{v}$ as Q, we can obtain through a more convoluted procedure the Navier-Stokes equation (1.8) by using the definition of the strees tensor of equation (1.7) and considering the term $\rho\frac{\partial \vec{v}}{\partial t}$ a force density $\vec{f}^{ext}$.

1.2.3 Reynold's number

We can write a dimensionless version of the Navier-Stokes equation (1.8) using the quantities $\tilde{u} \equiv u/v$, $\tilde{r} \equiv r/a$, $\tilde{t} \equiv \frac{t\eta}{\rho a^2}$, $\tilde{p} \equiv \frac{pa}{\eta v}$, $\tilde{f}^{ext} \equiv \frac{f^{ext}}{a}^2 \rho v$, where a and v are characteristic length and velocity. The resulting dimensionless Navier-Stokes equation becomes:

$$\frac{\partial \tilde{\vec{u}}}{\partial t} + Re\ \tilde{\vec{u}}\cdot\tilde{\vec{\nabla}}\tilde{\vec{u}} = \tilde{\nabla}^2\tilde{\vec{u}} - \tilde{\vec{\nabla}}\tilde{p} + \tilde{\vec{f}}^{ext} \tag{1.14}$$

which only depends on the dimensionless quantity $Re \equiv \frac{\rho v a}{\eta}$: the *Reynold's number*.

It means that as long as we keep constant this relation of parameters, the resulting flow will be equivalent when measured in the dimensionless parameters we defined. This fact is used in wind tunnels, in which the aerodynamics (which are ruled by the Navier-Stokes equation for compressible fluids) of a vehicle can be tested using a miniature of it with its same shape, as long as other parameters (*e.g.* the air velocity) are accordingly modified to keep Re constant. This is consistent with the fact that fluids do not possess any intrinsic length scale, thus as long as the continuous description is valid (which molecular dynamics

simulations carried out in [Alder and Wainwright, 1970] showed already occurs for a few hundred molecules), only the Reynold's number will be relevant to describe the flow.

The physical meaning of Re goes beyond the simple scaling of Navier-Stokes equation. It is also a quotient between inertial and viscous forces in a fluid. It separates two very differentiated behaviours for a fluid depending on whether its value is high or low, corresponding the former to turbulent flows and the later to laminar flows. In this thesis we will be interested in the low Re regime, since it is the scenario that arises at the microscale. However, as depicted in table 1.1, the everyday metric scale at which we move corresponds to high Re, thus some phenomena occuring at the low Re might seem counterintuitive.

Cetacea	$10^7 \sim 10^8$
Human swimmer	$10^4 \sim 10^5$
Goldfish	10^2
Plankton	10
Microorganisms	$10^{-5} \sim 10^{-4}$

Table 1.1: Some examples of approximate values of Re for several systems.

1.2.4 Stokes equation

If we make $Re \ll 1$ in equation (1.14), we can suppress the non-linear term in the velocity from the Navier-Stokes equation. The resulting equation becomes:

$$\vec{\nabla} p - \eta \nabla^2 \vec{u} = \vec{f}^{ext} \tag{1.15}$$

which is known as the *Stokes equation*.

Stokes equation describes a pure laminar flow, *i.e.* the fluid is constituted of layers which displace independently without mixing. This physical behaviour is mathematically explained from the time reversibility of the Stokes equation. The concept of time reversibility can be easier to understand for the case of a free fall under the effect of gravity. If we throw a body with an initial velocity pointing up, it will decelerate due to the effect of gravity until it reaches null velocity at the zenith of its trajectory; from there, it will fall with an increasing velocity due to gravity again. If we take a snapshot of the body measuring solely its position and the magnitude of its velocity, we will not be able to tell whether it is raising or falling. Taking $t = 0$ at the zenith of the trajectory, both $x(t) = x(-t)$, thus there is time reversibility.

The full Navier-Stokes equation (1.8) is not time reversible due to the presence of the term $\eta\nabla^2\vec{u}$, which is not present in the Stokes equation (1.15). Actually, the Stokes equation does not depend explicitly of time, thus time reversibility will appear as long as we also invert the external forces.

Time irreversibility is often associated to the action of friction and other dissipative forces. In the first example, the effect of friction in air would have led to the body reaching a limit velocity when falling, which would not match with its accelerated motion when raising. The motion of a viscous fluid described by Stokes equation is precisely characterized by the dominant role of friction, yet it still is time reversible if we remember to also invert the forces.

Time reversibility makes swimming at low *Re* a challenge that could explain why for billions of years life did not evolve past simple bacteria. In order to displace in a fluid, a swimmer must deform its body in such a way that it is able to self-propel. To displace long distances, it will need to perform this motion repeatedly. Finding a suitable cyclical pattern that in the end leads to a net motion is not trivial. A simple cycle in which the swimmer performs a stroke forward and returns to its original position by performing the same exact sequence in reverse, will result in a stroke back to the initial position, no matter how fast it tries to strike forward or how slow it tries to go back, since Stokes equation is not time dependent. These ideas were first introduced by Purcell [Purcell, 1977], in which he jokingly named the *scallop theorem* precisely to indicate that the swimming strategy of a scallop by just opening and closing its shell would not be effective to displace at low *Re*.

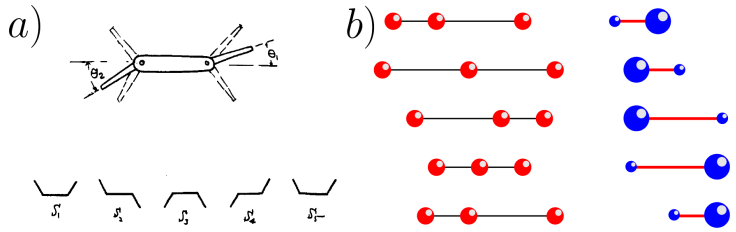

Figure 1.3: (a): On top, schematic view of the Purcell swimmer. On bottom, the cycle which allows its propulsion. Figure taken from [Purcell, 1977]. **(b):** Four-step cycle of the three-linked sphere swimmer [Najafi and Golestanian, 2004], in red spheres, and the *pushmepullyou* swimmer [Avron et al., 2005], in blue spheres. Figure taken from [Avron et al., 2005].

Purcell also proposed in [Purcell, 1977] a very simple model of microswimmer, consistent of a rigid rod body with two mobile arms at its extremes (see figure 1.3 (a)), capable of overcoming low Reynolds' time reversibility in a four step cycle. This mechanism is similar to the one employed by some microorganisms [Berg, 2002]. Alternative models have been proposed in this quest for finding the simplest possible microswimmer. Golestanian and Najafi proposed a one-dimensional model of three spheres united by links with variable length [Najafi and Golestanian, 2004]; its cycle is depicted in red in figure 1.3

(b). The *pushmepullyou* microswimmer, consistent of two spheres of variable volume united by an extensible link, offers an improved performance per cycle respect the previous model [Avron et al., 2005]; its cycle is depicted in blue spheres in figure 1.3 (b).

1.2.5 Flow past a sphere

As professor Wilson Poon once told us at a summer school, a good model system for active matter must consist of spherical particles to make the job easier for theoreticians who want to compare their models with experiments. Active matter usually deals with mobile units with non isotropic shapes which favour the motion in some privileged directions. From a practical point of view, working with colloidal systems usually makes spherical swimmers more accessible to experimentalists. From a mathematical point of view, most of the calculations presented in this section are doable thanks to spherical symmetry, which greatly simplifies them. Looked from far enough, a sphere can be treated as an even simple shape: a point singularity. Given a punctual force density $\vec{f}^{ext} = \vec{F}_0\delta(\vec{x}-\vec{x}_0)$ located at $\vec{x}_0$, the flow it will create is known as *stokeslet*. Making use of the linearity of the Stokes equation (1.15), it will be of the form:

$$\vec{u}(\vec{x}) = \boldsymbol{T}(\vec{x}-\vec{x}_0)\vec{F}_0 \tag{1.16}$$

where $\boldsymbol{T}$ is the *Oseen tensor*, which connects a point force at $\vec{x}_0$ with the flow it creates at an arbitrary point in space $\vec{x}$. It depends on the distance between the singularity and the point where we want to compute the flow, which we can define with translated coordinates as $\vec{r} \equiv \vec{x}-\vec{x}_0$. The Oseen tensor is then given in Cartesian coordinates by:

$$T_{ij} = \frac{1}{8\pi\eta}\left(\frac{\delta_{ij}}{r} + \frac{r_i r_j}{r^3}\right) \tag{1.17}$$

Given a spherical swimmer that translates with velocity $\vec{v}$ and rotates with angular velocity $\vec{\omega}$, we can assume the fluid will fulfil stick boundary conditions aka no-slip boundary conditions, *i.e.* the fluid displaces with the same velocity that the solid boundary. This can be expressed as:

$$\vec{u}(\vec{x}) = \vec{v} + \vec{\omega}\times(\vec{x}-\vec{x}_0),\ \forall\vec{x}\in\partial V \tag{1.18}$$

where $\vec{x}_0$ is the center of the sphere and ∂V its surface. In an unbound fluid, we may tie this condition with the vanishing of the flow at large distances $\vec{u}(\vec{x}) = 0 \Leftrightarrow |\vec{x}| \to \infty$. Computing now the integral:

$$\vec{u}(\vec{x}) = \oint_{\partial V} \boldsymbol{T}(\vec{x}-\vec{x}')\cdot\vec{f}(\vec{x}')dS' \tag{1.19}$$

with the proper choice of $\vec{f}$ we will obtain the flow field generated by a single sphere. We are interested in two scenarios: a sphere displacing at constant velocity, and a sphere rotating at constant angular velocity.

For the first case, we need a force density $\vec{f} \propto \vec{v}/4\pi a^2$, with the proportionality constant being the Stokes friction $6\pi\eta a$ for the case $\omega = 0$. The created flow, given in Cartesian coordinates will be:

$$u_i = \left[\frac{3}{4}\frac{a}{r}\left(\delta_{ij} + \frac{r_i^2}{r^2}\right) + \frac{1}{4}\left(\frac{a}{r}\right)^3\left(\delta_{ij} - \frac{3r_i^2}{r^2}\right)\right] v_j \tag{1.20}$$

Integrating this force density along the surface of the sphere, we recover the well-known Stokes law $\vec{F} = 6\pi\eta a\vec{v}$. Alternatively, we could have recovered this result from integrating the stokeslet along the surface of a sphere of radius a centered at $\vec{x}_0$.

For a sphere rotating at constant angular velocity, the suitable choice of a force density is $\vec{f}(\vec{x}') \propto \frac{1}{4\pi a^2}\vec{\omega} \times (\vec{x} - \vec{x}_0)$, with the proportionality constant being $8\pi\eta a^3$ for $v = 0$. Evaluating it at (1.19), we obtain the following flow:

$$u_i = \left(\frac{a}{r}\right)^3 \varepsilon_{ijk}\omega_j r_k \tag{1.21}$$

The torque $\vec{\tau}$ created by a rotating sphere can also be computed:

$$\vec{\tau} = \oint \vec{f}(\vec{x'}) \times (\vec{x} - \vec{x}_0) dS' = 8\pi\eta a^3\omega \tag{1.22}$$

from where we get the Stokes friction coefficient for a rotating sphere.

1.2.6 Wall effects

There are no truly unbound fluids in experimental set ups, and in some cases the boundaries can be close enough to the fluid volume we are interested in studying the role they may have at distorting the flow. This fact is specially relevant in the field of microfluidics, in which the fluids are usually confined in volumes of a few cubic microns. The effect of solid boundaries was first addressed by Blake [Blake and Chwang, 1974]. We present the flows we previously introduced when an interface at height h in the z direction is present. We distinguish solid from fluid boundaries through the binary parameter ξ, whose value is 1 for the solid case and 0 for the fluid interface. The stokeslet now becomes:

$$\begin{aligned} u_i =& \frac{F_j}{8\pi\eta}\left[\left(\frac{\delta_{ij}}{r} + \frac{r_i r_j}{r^3}\right) - \left(\frac{\delta_{ij}}{R} + \frac{R_i R_j}{R^3}\right)\right. \\ &\left. + 2h\xi(\delta_{j\alpha}\delta_{\alpha k} - \delta_{jz}\delta_{zk})\frac{\partial}{\partial R_k}\left\{\frac{hR_i}{R^3} - \left(\frac{\delta_{iz}}{R} + \frac{R_i R_z}{R^3}\right)\right\}\right] \end{aligned} \tag{1.23}$$

where $\vec{R} \equiv (x - x_0)\hat{x} + (y - y_0)\hat{y} + (z + h)\hat{z}$.

While for the case of a sphere of radius a rotating at constant angular velocity $\vec{\omega}$, the flow it creates is given by:

$$\frac{u_i}{a^3} = \frac{\varepsilon_{ijk}\omega_j r_k}{r^3} - \frac{\varepsilon_{ijk}\omega_j R_k}{R^3} + 2h\xi\varepsilon_{kjz}\omega_j\left(\frac{\delta_{ik}}{R^3} - \frac{3R_i R_k}{R^5}\right) + 6\xi\varepsilon_{kjz}\frac{\omega_j R_i R_k R_z}{R^5} \tag{1.24}$$

where $\boldsymbol{\varepsilon}$ is the Levi-Civitta symbol.

1.2.7 Squirmers

As stated before, swimming at low *Re* requires smart strategies that can overcome the time reversibility associated to Stokes flow. Even though we are interested in describing the motion of spherical swimmers, the first attempts at describing the motion of microswimmers have been historically associated to elongated structures that resemble flagella. Taylor [Taylor, 1951] was the first to study how the undulation and distortion of flagella could lead to motion and how hydrodynamic cooperation affected the velocity associated to this mechanism.

That very same year, Lighthill [Lighthill, 1951] proposed the *squirmer* model, an alternative to describe the motion of microorganisms that do not possess flagella. In the case of biological swimmers, it would correspond to a cell covered by cilia. These cells are described as deformable spheres, whose surface can change its shape in order to displace. This model was further developed by Blake [Blake, 1971] two decades later.

It solves Stokes equation (1.15) for an incompressible fluid imposing a slip boundary condition in the surface of the spherical swimmer of radius a. The flow created is axisymmetric, and can be described with a radial and azimuthal component, with $\theta = 0$ corresponding to the direction of propulsion of the particle and the origin $r = 0$ being at the center of the squirmer.

$$\begin{aligned} u_r(r=a) &= \sum_{n=0}^{\infty} A_n P_n(\cos\theta) \\ u_\theta(r=a) &= \sum_{n=1}^{\infty} B_n V_n(\cos\theta) \end{aligned} \tag{1.25}$$

where P_n is a Legendre polynomial, $A_n(t)$ and $B_n(t)$ can be functions of time and $V_n = \frac{2}{n(n+1)} \sin\theta \frac{d[P_n(\cos\theta)]}{d\cos\theta}$. The solution is:

$$\begin{aligned} u_r =& -U\cos\theta + A_0\frac{a^2}{r^2}P_0 + \frac{2}{3}(A_1+B_1)\frac{a^3}{r^3}P_1 + \\ & \sum_{n=2}^{\infty}\left[\left(\frac{1}{2}n\frac{a^n}{r^n} - \left(\frac{1}{2}n-1\right)\frac{a^{n+2}}{r^{n+2}}\right)A_nP_n + \left(\frac{a^{n+2}}{r^{n+2}} - \frac{a^n}{r^n}\right)B_nP_n\right] \\ u_\theta =& U\sin\theta + \frac{1}{3}(A_1+B_1)\frac{a^3}{r^3}V_1 + \\ & \sum_{n=2}^{\infty}\left[\left(\frac{1}{2}n\frac{a^{n+2}}{r^{n+2}} - \left(\frac{1}{2}n-1\right)\frac{a^n}{r^n}\right)B_nV_n + \frac{1}{2}n\left(\frac{1}{2}-1\right)\left(\frac{a^n}{r^n} - \frac{a^{n+2}}{r^{n+2}}\right)A_nV_n\right] \end{aligned} \tag{1.26}$$

It is also imposed that the origin moves relative to the fluid with velocity

$$U = \frac{1}{3}(2B_1 - A_1) \tag{1.27}$$

in order to ensure the motion has finite total energy.

The squirmer model we will be using introduces further simplifications to Blake's solution. First, we consider the swimmer creates a flow with only azimuthal component of the velocity. It physically means the particle does not vary its volume in its displacement by contracting or expanding itself. Mathematically, it makes $A_n = 0\ \forall n$. Additionally, we truncate the expansion in u_θ from equation (1.25) to $n = 2$. The term B_1 will give us the self-propulsion velocity of the swimmer (equation (1.27)), while the second is associated to the stress the swimmer causes to the fluid as it displaces. The ratio between B_2 and B_1 is defined as β:

$$\beta \equiv \frac{B_2}{B_1} \tag{1.28}$$

Depending on the sign of β, the squirmer can either be a *puller* when $\beta > 0$, or a *pusher* when $\beta < 0$, which as their names indicate, displace by either pulling the fluid in front of them or pushing the fluid back behind them respectively. A colour map with the different flows created by these two different type of swimmers is shown in figure 1.4. The special case $\beta = 0$ corresponds to a swimmer that displaces without exerting any stress on the fluid.

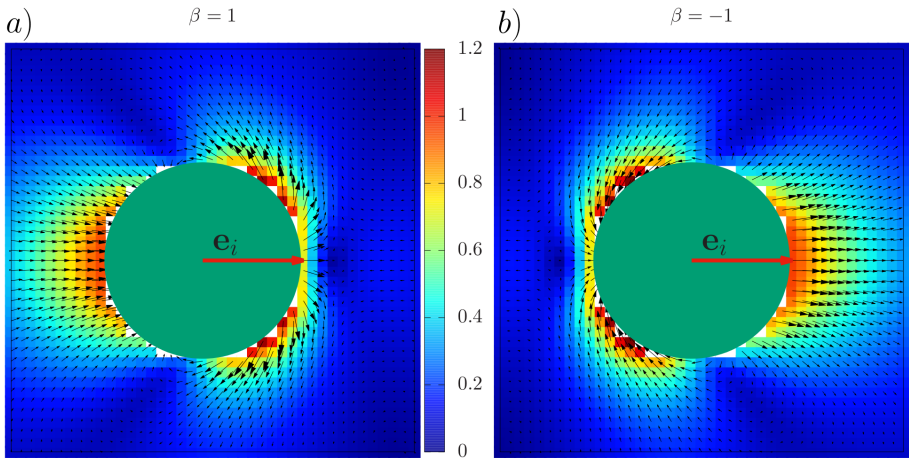

Figure 1.4: Coloured stream map with the flow created by: **(a):** Puller ($\beta = 1$). **(b):** Pusher ($\beta = -1$). Direction of propagation of the squirmer marked with a red arrow. Figures obtained by Francisco Alarcón using lattice-Boltzmann simulations.

1.2.8 Dynamic equations for interacting swimmers

We will often deal with systems formed by a collection of swimmers. We can be interested in writing the dynamic equations that describe these systems, to either solve them directly in those cases in which that is possible, or even just to identify dimensionless parameters similar as Re that measure the relative importance of all the interactions involved in the system. With what we have seen, we can now write a general form of the dynamic equations a system of

interacting swimmers obeys. Given N swimmers, we can write a Newton's equation for each of them:

$$M_i \ddot{\vec{x}}_i = \gamma(\vec{u}(\vec{x}_i) - \dot{\vec{x}}_i) + \sum \vec{F}^{ext} \tag{1.29}$$

where M_i is the particle mass, $\vec{x}_i$ its position, $\dot{\vec{x}}_i$ its velocity and $\ddot{\vec{x}}_i$ its acceleration; $\vec{u}(\vec{x}_i)$ is the fluid velocity at its position, $\sum \vec{F}^{ext}$ is the sum of all the external forces acting on the particle and γ is a friction coefficient, which we will usually take as Stokes coefficient $\gamma = 6\pi\eta a$, which is valid to describe spheres in an unbound fluid. Since we are working at low Re, inertia can be neglected and therefore $\ddot{x} = 0$.

In the simplest possible case, in which there are no external forces at all, equation (1.29) is greatly simplified and just becomes:

$$\dot{\vec{x}}_i = \vec{u}(\vec{x}_i) \tag{1.30}$$

i.e. each particle will move with a velocity given by the flow created by its neighbours.

In case any forces were present in the system, which could have its origin in additional interactions between the particles (*e.g* electrostatic forces) or be caused an external field that acts on all particles (*e.g.* gravity), the equation would then become:

$$\dot{\vec{x}}_i = \vec{u}(\vec{x}_i) + \frac{1}{\gamma} \sum \vec{F}^{ext} \tag{1.31}$$

External forces are associated to the generation of stokeslets by the neighbouring particles, which must be included in $\vec{u}$ in addition to the flows created by the intrinsic motion of the swimmers.

1.3 Simulation methods

With the advances in the field of computation, *simulations* in science, a new methodology that lies midway between theory and experiments, have grown in importance. We could set the first precedent of a simulation work in the Metropolis article [Metropolis et al., 1953], which introduced what is now known as Monte Carlo (MC) methods and also the use of periodic boundary conditions. That article dealt with the ferromagnetic to paramagnetic transition in a two dimensional Ising lattice, a task that nowadays undergraduate students can perform in their laptops in a matter of minutes (if we just take into account computation time) while wasting most of the machine resources in leisure activities. Here we will not introduce a history of the technological breakthroughs that have made this possible, but congratulate ourselves they are available to us as most of the work contained in this text is the result of simulations. The high power of computation have allowed us to propose more elaborate models to describe systems of overgrowing complexity, *i.e.* containing more degrees of freedom and more interactions among their elements. A clear example on this complexity increase is the study of complex fluids, among which we can find

As three-legged stools are the most robust, good science relies on three legs too: experimental observations, theoretical models and simulations.

colloidal suspensions and polymers. These fluids have the peculiarity of introducing an intermediate scale between the microscopic description of individual fluid molecules and the macroscopic description given by continuous fields; for the particular case of colloids, it would correspond to the size of the colloidal particles, which range from fractions of microns to hundreds of them. These fluids still admit a continuous description, although its rheological properties will be far different from those of a Newtonian fluid. However, when treating the problem at the scale of the colloid, we can consider them as solids submerged in a solvent which we can treat as a simple fluid. This intermediate scale is known as the *mesoscale*. In this thesis we will look at colloidal suspensions with this zoom level.

We can classify simulation methods for fluid dynamics based on the size scale at which they operate. At the smaller scale, we can treat a fluid as a collection of molecules and solve the basic dynamic equations for each of them individually, which is known as molecular dynamics (MD). MD can be useful to study small volumes of fluid, specially in very confined systems. However it is not the most appropriate way to deal with complex fluids, since they possess the additional length scale of other particles suspended in the solvent, and it can take very long to couple the behaviour at both scales and obtain relevant results at a larger macroscopic scale. On the other extreme, we can treat the fluid as a continuous medium, as we have already introduced in section 1.2. In the case of being interested on solving the dynamics of a colloidal particle suspended in the fluid, we would need to solve equations of the form of (1.31), which in the end is a procedure similar to MD but starting at a larger scale. Even though we have used this method in some cases, the expressions of the flux created by a swimmer are always approximate. Properly dealing with finite size effects already requires the refinement of the flow equations we use, while using particles with non-trivial shapes or having the fluid confined by non-planar boundaries

are unaffordable challenges from the analytical point of view.

An intermediate approach becomes necessary to overcome the limitations of the previously exposed methodologies. Several coarse-grained methods have been developed to fit different needs. Two of the most popular ones are Brownian dynamics (BD) and dissipative particle dynamics (DPD). In BD the solvent is represented implicitly by random forces and frictional forces. It solves a simplified version of the Langevin equation in which particle inertia is neglected. BD does not conserve momentum, thus hydrodynamics are not present [Ermak and McCammon, 1978]. DPD [Hoogerbrugge and Koelman, 1992, Groot and Warren, 1997] explicitly solves solvent dynamics. The fluid is described as a collection of coarse particles with continuous positions and velocities. These fictitious particles interact with each other through soft potentials, which allow DPD simulations to reach time scales orders of magnitude larger than those of MD. Español and Warren [Español and Warren, 1995] added a correction to the fluctuation-dissipation relation to DPD to preserve hydrodynamics. A third method at this scale, which is the one we have used, is Lattice-Boltzmann (LB). LB solves a discrete version of the Boltzmann equation (1.10). As we have seen, it does not deal with continuous fields such as velocity, density and pressure, but with a local distribution function of the number of particles and their velocity at a given time; computing the momenta of this distribution, we can recover the aforementioned fields.

1.3.1 The Lattice-Boltzmann method

Lattice-Boltzmann (LB) is a simulation method that solves a discrete version of Boltzmann equation (1.10). Historically, it was developed as a spin-off of lattice gas cellular automata methods (LGCA), originally introduced in 1973 [Hardy et al., 1973]. These methods discretize the space as a lattice whose nodes can be either empty or occupied by a gas particle. In 1986, Frisch [Frisch et al., 1986] changed the original rectangular lattice for an hexagonal one, recovering the Navier-Stokes macroscopic behaviour; it was considered an Ising model for turbulence. However, LGCA had several flaws, listed in [Succi, 2001]: lattice discreteness leads to lack of Galilean invariance and anomalous velocity dependence of the fluid pressure; additional drawbacks from phase-space discretization are statitiscal noise, high viscosity (*i.e.* difficulties to simulate high Re flows), the complexity of the method itself (which leads to non-competitive computation times) and the apparition of spurious invariants. LB was introduced shortly after [McNamara and Zanetti, 1988, Higuera and Jiménez, 1989] as an alternative to solve those flaws. It is based on a similar idea, but solving the dynamics of the distribution function $f(\vec{x}, \vec{v}, t)$ instead of that of individual particles. This way we lose the possibility of having an Ising model for fluid problems, but gain instead a competitive simulation method.

LB works in a discretized phase space: not only the positions are limited to a lattice, but there is also a limited set of m possible velocities, $\vec{c}_i$. The dynamics is based on a two-step process, with a stream phase in which the distribution functions are translated moving the fraction of particles associated to each node with their correspondent velocity, and a collision step that simulates the real particle collision that would occur if two or more of them arrived at

the same position at the same time instant. Both stream and collision steps are completely local, which facilitates the parallelization of the code. We can write the algorithm as:

$$f_i(\vec{x}_i + \vec{c}_i\Delta t, t + \Delta t) = f_i(\vec{x}, t) + \Delta[f_j(\vec{x}, t)] \tag{1.32}$$

where f_i is an abbreviated form of writing the fraction of particles with velocity $\vec{c}_i$, $f(\vec{c}_i)$, and Δ_i is the collision operator. Writing a collision operator capable of describing accurately the particle collision is key in the success of a LB code; most of the development done to LB has been finding the simplest possible collision operator capable of recovering sensible physics.

Δ_i is a non-linear operator. However, for simplicity it can be replaced by a linearized collision matrix [Higuera et al., 1989], $\mathcal{L}_{ij}$. The distribution function f_i can be expressed as the sum of the equilibrium term f_i^{eq} and a non-equilibrium deviation f_i^{neq}, $f_i = f_i^{eq} + f_i^{neq}$. The collision matrix sets the relaxation of f_i towards its equilibrium value.

$$\Delta_i[f_j(\vec{x}, t)] = \mathcal{L}_{ij} \sum_{j=1}^{m} [f_j(\vec{x}, t) - f_j^{eq}(\vec{x}, t)] \tag{1.33}$$

We can ensure the collision matrix respects mass and momentum conservation by imposing some of its eigenvalues are zero, concretely $\sum_j \mathcal{L}_{ij} = 0$ and $\sum_j \mathcal{L}_{ij}\vec{c}_j = 0$.

Further simplification can be imposed to the collision matrix working with a single-time relaxation operator, which turns $\mathcal{L}_{ij}$ into a diagonal matrix with a single value $\mathcal{L}_{ij} \propto \delta_{ij}$. This idea is taken from the Bhatnagar-Gross-Krook (BGK) theory [Bhatnagar et al., 1954]. Therefore, equation (1.33) becomes:

$$\Delta_i[f_i(\vec{x}, t)] = \frac{f_i^{eq} - f_i}{\tau} \tag{1.34}$$

where τ is the relaxation time. We can relate it to the fluid shear and bulk viscosity [Cates et al., 2004]:

$$\begin{aligned} \eta_s &= \left(\tau - \frac{\Delta t}{2}\right) c_s^2 \\ \eta_b &= \frac{2\eta_s}{3} \end{aligned} \tag{1.35}$$

where $c_s = \frac{1}{\sqrt{3}}\frac{\Delta x}{\Delta t}$ is the speed of sound in the lattice. Typically, Δx and Δt are set to the unity. The fluid density ρ is also typically set to 1 for a quiescent fluid.

Another pending choice is the discretization of the phase space, both the positions lattice geometry and the set of allowed velocities. Lattices are usually rectangular or simple cubic, while there is more freedom in the velocities choice. The notation D_nQ_m introduced in [Qian et al., 1992], where n stands for the system dimension (two or three), and m for the number of allowed velocities, has become the standard to define that choice.

Precisely in [Qian et al., 1992], it is exposed that for a three-dimensional lattice, 15 velocities (D_3Q_{15} in their notation we just introduced) suffice to get an excellent agreement between numerical simulations and theory. In this thesis, we have used the now more popular D_3Q_{19} geometry. These two sets of velocities are represented in figure 1.5. It is possible to work with more velocities, although they do offer little gain for the computational cost they have.

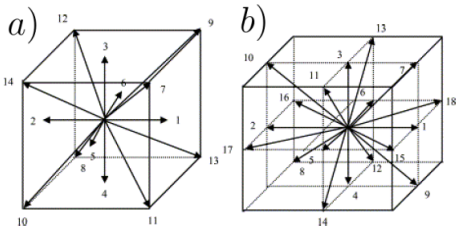

Figure 1.5: Representation of the velocities $\vec{c}_i$ chosen for the **(a):** D_3Q_{15} case, and **(b):** D_3Q_{19} case. Velocities are numbered from 0 to $m-1$, with 0 corresponding to null velocity. Figure taken from [Llopis, 2010].

Even though LB was initially introduced as a method suitable to simulate high Re conditions [Succi, 2001], it has found applications in many other fields. One of those fields that has made it a very suitable method for this thesis is the simulation of colloidal suspensions.

1.3.2 Introducing colloids into lattice-Boltzmann

In order to simulate the hydrodynamic interactions between solid particles in suspension, LB must be modified to incorporate the boundary conditions imposed on the fluid by solid particles. Historically, they were first introduced in lattice-gas simulations by replacing the usual collision rules at nodes corresponding to solid boundaries by a "bounce-back" collision rules [Frisch et al., 1987], in which incoming particles are reflected back towards the nodes they came from.

In LB we use the "link-bounce-back" rules introduced by Ladd [Ladd, 1994a]. Solid particles are defined by a boundary surface, which could be any size or shape; in figure 1.6 we display a circle. The boundary surface cuts some of the links between lattice nodes, and fluid moving along these links interact with the solid surface at boundary nodes placed halfway along the links. Thus we obtain a discrete representation of the particle surface, which becomes more precise as the particle gets larger. At both sides of the boundary there is fluid. At each boundary node there are (at least) two incoming distributions $f_i(\vec{r}, t_+)$ and $f'_i(\vec{r}+\vec{c}_i, t_+)$, corresponding to velocities $\vec{c}_i$ and $\vec{c}'_i = -\vec{c}_i$ parallel to the link connecting $\vec{r}$ and $\vec{r}+\vec{c}_i$, and the notation $f_i(\vec{r}, t_+) = f_i(\vec{r}, t) + \Delta_i(\vec{r}, t)$ is used to indicate the post-collision distribution. These distributions are reflected back, so that

$$\begin{aligned} f_i(\vec{r}+\vec{c}_i, t+1) &= f_i'(\vec{r}+\vec{c}_i, t_+) \\ f_i'(\vec{r}, t+1) &= f_i(\vec{r}, t_+) \end{aligned} \tag{1.36}$$

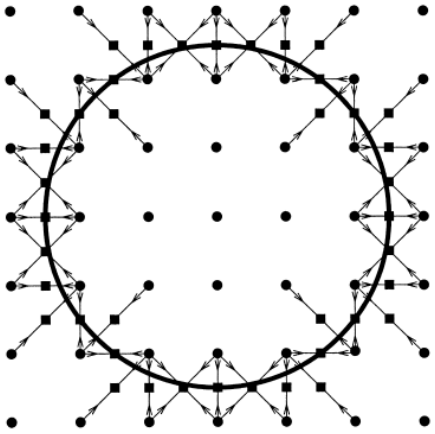

Figure 1.6: Location of the boundary nodes for a circular object of radius 2.5 lattice spacings. The velocities along links cutting the boundary surface are indicated by arrows. The locations of the boundary nodes are shown by solid squares and the lattice nodes by solid circles. Figure taken from [Ladd, 1994a].

In case the solid boundary is moving (*e.g.* a moving colloid), velocity of the fluid at the boundary node $\vec{u}_b$ is determined by the solid particle velocity $\vec{U}$, angular velocity $\vec{\Omega}$ and center of mass $\vec{R}$:

$$\vec{u}_b = \vec{U} + \vec{\Omega} \times \left(\vec{r} + \frac{1}{2}\vec{c}_i - \vec{R} \right) \tag{1.37}$$

In that case, there in addition to reflection, population density is transferred across the boundary node, and part of the fluid enters to the particle according to:

$$\begin{aligned} f_i(\vec{r}+\vec{c}_i, t+1) &= f_i'(\vec{r}+\vec{c}_i, t_+) + \frac{2\rho\vec{u}_b \cdot \vec{c}_i}{c_s^2} \\ f_i'(\vec{r}, t+1) &= f_i(\vec{r}, t_+) - \frac{2\rho\vec{u}_b \cdot \vec{c}_i}{c_s^2} \end{aligned} \tag{1.38}$$

For spherical particles, there are optimal radius values which minimize discretization effects [Nguyen and Ladd, 2002]: 1.25, 2.3, 3.7 and 4.77 are the smallest ones. In this thesis we have been using 2.3 and 3.7; we will indicate the chosen value in every case. Even when using these optimal values, there might be still divergences between the nominal radius we impose to the particle and the hydrodynamic radius it effectively behaves as. It has been shown [Ladd, 1994b] that the hydrodynamic radius depends only on particle size and fluid viscosity, but not on the particle configuration, flow geometry or Reynolds number. Thus,

it is a well-defined physical parameter that can be determined by a single calibration experiment. In section 2.3 we present a method we found to calibrate it.

Surface forces are calculated from the momentum transfer at each boundary node and summed to give the force and torque on each object [Ladd, 1994a]. Bounce-back involves changes in the velocity distribution functions which lead to a force and torque acting locally on the fluid. The opposite force and torque are exerted on the particle. Hence, the overall fluid momentum exchange through bounce-back determines the net force and torque acting on the rigid particle, which are used to update the particle linear and angular velocities at each time step. These velocities are then used to update the particle position and direction; the motion of suspended particles is, hence, determined by the force and torque exerted on it by the fluid, and is resolved by a MD like algorithm [Lowe et al., 1995]. With this method, we ensure a correct description of the dynamic coupling between the collective modes of the solvent and the suspended particles. In contrast to finite-difference and finite-element methods, where local surface normals are required to integrate the stresses over the particle surface, the bounce-back rule eliminates these complications by directly summing the surface forces [Ladd and Verberg, 2001].

1.3.3 Parallelization of lattice-Boltzmann

The numerical resolution of the dynamics of a system of particles described by equations of the form of equation (1.31) can quickly scale with the number of particles involved and become unsolvable. For the case of interacting particles, if they interact with each other, it should scale like $\sim N^2$. Additionally, the flow at position $\vec{x}_i$ depends on the force felt by all particles j, thus they must be computed beforehand, forcing the repetition of the loop, thus it scales like $\sim 2N^2$. The long range of hydrodynamic interaction also makes parallelization harder/impossible.

LB solves this last issue by locally solving all hydrodynamic interactions, which depend only on the information from immediate neighbours, thus parallelization is doable. Due to the cubic symmetry of the space lattice, a regular decomposition is possible for fluid-only problems. The presence of colloids requires of a slightly different strategy based on the concept of a cell list [Stratford and Pagonabarraga, 2008]. A schematic view on how the system decomposition works when parallelizing LB with colloids is shown in figure 1.7. The system is decomposed in subdomains (solid line), which are operated by independent processors. Each subdomain is then divided in an integer number of cells (dashed line), whose length marks a cut-off for the short range interactions between colloids. Besides the subdomain, each processor also deals with the halos (shaded squares), which contain a copy of the neighbouring cells to the subdomain in order to be capable of computing all the interactions between neighbouring subdomains.

Particles which lie between more than one subdomain or which change from one to another during their propagation make the parallelization more complicated. Taking this into account, the basic algorithm once the code has been

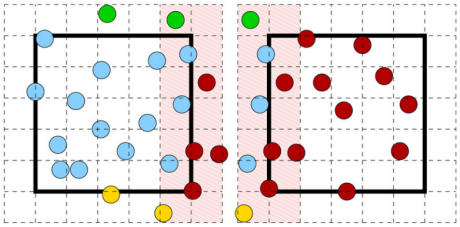

Figure 1.7: Schematic view of the decomposition of a 2D LB system with colloids (coloured circles). Subdomains are delimited with solid lines, cells with dashed lines and the halos are shaded. Figure taken from reference [Stratford and Pagonabarraga, 2008].

parallelized consists of [Stratford and Pagonabarraga, 2008]:

1. Communication of halo information.
2. Particles in the halos are identified and their information is communicated to the the corresponding processor.
3. Boundary links are constructed. Actions arising from changes in particle shape are performed.
4. Cell list search on each process to identify and compute short-range interactions between close particles.
5. Collision stage for fluid sites within each subdomain is computed.
6. Communication of post-collision distributions in the halo regions.
7. Communication of particle partial sums for interaction forces and corrections arising from changes in shape are performed.
8. First computation of forces and torques on particles (applying bounce-back rules).
9. Communication of those results.
10. Particle velocity and position updates are performed for all particles on all processes.
11. A second computation of forces and torques on particles is performed to update the distributions at the appropriate fluid sites.
12. Propagation stage.

In total, there are five stages at which there is communication between processors. Parallel LB simulations scale $\sim l^3$, where l is the subdomain size; however, communication between processors only depends on the area of the subdomains, therefore those steps scale $\sim l^2$.

The LB code we employ is *Ludwig* [Desplat et al., 2001, Stratford and Pagonabarraga, 2008], a code developed for years at the University of Edinburgh to which our group has access, and whose performance has been thoroughly tested and optimized.

Chapter 2

Dynamic equations for magnetic rotors

The highest form of human excellence is to question oneself and others.

Socrates

This is still a pretty theoretical chapter in which we introduce the fundamentals that will be used in the following two chapters. Magnetic rotating colloids have been the basic active unit of the systems used there. Therefore, it is important to have a previous knowledge of their motion and the interactions between them. In section 2.1, we describe the rotation of an isolated magnetic colloid in a viscous fluid. After studying the motion of an isolated particle, we study their collective behaviour in section 2.2, by introducing how magnetic colloids interact with each other. This allows us to write the dynamic equations for a system of magnetic rotors, and introduce the dimensionless parameters we use to characterize the different conditions they can be subjected to. Finally, in section 2.3 we describe the simulation methods we have employed to describe this kind of systems.

2.1 A magnetic rotor in a viscous fluid

When we apply a circularly oscillatory magnetic field to a particle that possesses a magnetic moment, we will induce a rotation to it. This fact makes magnetic colloids an ideal experimental system to study the behaviour of rotors immersed in a fluid. A qualitative explanation typically given is that the magnetic moment of the particle tends to align with the magnetic field and rotate in solidarity with it, which in turn pushes the particle to perform the same rotation. This happens until a critical frequency of the magnetic field Ω_C is reached, above which the magnetic moment is unable to follow the magnetic field, hence the particle no longer rotates with a constant angular velocity. These two distinct regimes are called synchronous and asynchronous. This behaviour can be described by a nonuniform oscillator equation [Strogatz, 1994]. Experimental systems that can be described this way have been widely reported [Helgesen et al., 1990, Bacri et al., 1995, Yellen et al., 2007, Agayan et al., 2008, Straube and Tierno, 2013]. In [Helgesen et al., 1990], a minimal theoretical model backed by simulations and experimental measurements for ferromagnetic particles is provided. They found how the angular velocity ω varies with the applied frequency Ω above the critical value, observing a decay given by $\langle\omega\rangle = \Omega(1 - \sqrt{\Omega^2 - \Omega_C^2})$. Similar behaviours are described for systems of paramagnetic particles [Yellen et al., 2007]. However, we could also find works that take into account more explicitly the nanometric structure of superparamagnetic materials [Janssen et al., 2009]. Paramagnetic materials response can be highly size-dependent once domains reach sizes small enough. Some colloids can be filled by nanometric superparamagnetic particles, which despite their small size may play an important role at determining the macroscopic response of the colloid to a rotating magnetic field. In [Janssen et al., 2009], a very detailed model which took into account the magnetic domain size distribution to compute the angular velocity commercial magnetic colloids "Dynabeads®" would develop under the effect of a circularly rotating magnetic field is proposed and tested. In this section we will introduce magnetic models that take into account the coupling between the hydrodynamic torque and the magnetic torque in an isolated colloid submerged in an unbound fluid. We will deal separately with the ferromagnetic and paramagnetic case; in the later case, we will first solve the case of a single domain particle before dealing with a more realistic particle with an inhomogeneous distribution of

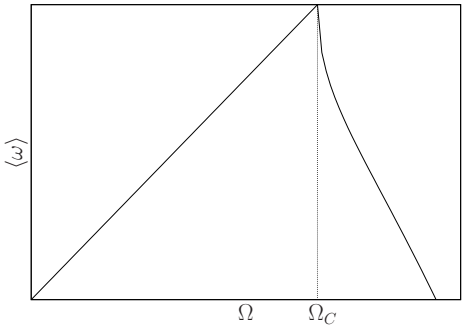

Figure 2.1: Average angular velocity $\langle\omega\rangle$ as a function of field frequency Ω for a ferromagnetic colloid. Dashed line at $\Omega = \Omega_C$ separates the synchronous regime, at which the particle rotates with constant angular velocity, from the asynchronous regime, in which it is not.

paramagnetic domains.

The models we introduce are based on two main equations: torque balance on the magnetic colloid and the dynamics of its magnetic moment. We consider the colloid to be a spherical particle of radius a with a magnetic moment $\vec{m}$ in a fluid of viscosity η. Its angular velocity $\vec{\omega}$ will vary due to two torque contributions: on the one hand, the magnetic torque $\vec{m} \times \vec{B}$, with $\vec{B}$ being the applied magnetic field, and on the other hand the hydrodynamic friction given by $8\pi\eta a^3\vec{\omega}$. At the steady state, the particle will rotate with a constant angular velocity at the steady state, thus these two contributions will balance each other.

$$\vec{m} \times \vec{B} = 8\pi\eta a^3\vec{\omega} \tag{2.1}$$

The dynamics of the magnetic moment will vary depending on whether the material is ferromagnetic or paramagnetic. However, due to the particle rotation, the magnetic moment will also rotate in solidarity with the particle. This will always add a term to the magnetic moment evolution equation:

$$\dot{\vec{m}} = \vec{\omega} \times \vec{m} \tag{2.2}$$

This set of equations is general for any spherical magnetic colloid, but we will introduce its solutions for a particular geometry (figure 2.2), which we will use in the following chapters. The applied magnetic field is circularly oscillatory, with amplitude B_0 frequency Ω, on the XZ plane, therefore $\vec{B} = B_0(\cos\Omega t, 0, \sin\Omega t)$. We assume the magnetic moment of the particle will follow the external magnetic field, although with a phase shift Φ, with the resulting magnetic moment being of the form $\vec{m} = m_0(\cos(\Omega t + \Phi), 0, \sin(\Omega t + \Phi))$. This assumption allows us to analytically solve the full dynamics of the colloid (angular velocity and magnetic moment) for any synchronous solution[1]. From equation (2.1), we obtain that the particle will rotate with an angular velocity pointing in the y direction $\vec{\omega} = \omega\hat{y}$.

[1]Synchronization in this case is between the magnetic field and moment, and not necessarily between the angular velocity of the particle and the frequency of the oscillatory field, as explained in the opening paragraph of this section.

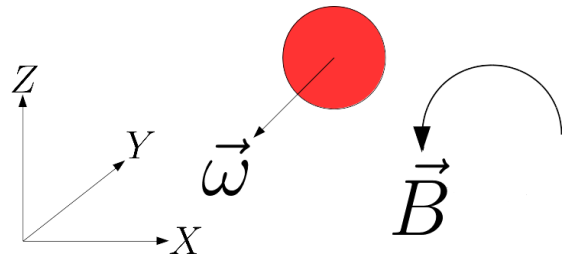

Figure 2.2: Scheme with the geometry of the applied magnetic field and the resulting colloid rotation.

2.1.1 Ferromagnetic rotors

A ferromagnetic material is characterized by having a magnetic moment of constant modulus m_0, even when no magnetic field is applied to it. For such material, we do not need to add any new term to equation (2.2) to already describe the evolution of the magnetic moment. Therefore, the only variables left are $\vec{\omega}$ and Φ. Their values turn out to be:

$$\begin{aligned} \vec{\omega} &= -\Omega\hat{y} \\ \Phi &= \arcsin\left(-\frac{8\pi\eta a^3\Omega}{m_0 B_0}\right) \end{aligned} \tag{2.3}$$

Hence, ferromagnetic particles will rotate with an angular velocity equal in modulus to the frequency of the applied field, but only if that frequency is below a threshold $\Omega_C = \frac{m_0 B_0}{8\pi\eta a^3}$. Applying our procedure we cannot predict the behaviour past Ω_C.

2.1.2 Paramagnetic rotors

Paramagnetic materials are characterized by having a magnetic moment induced by an external magnetic field; therefore, we can no longer assume the modulus of the magnetic moment has a fixed value, but it becomes a new variable to deal with. The magnetic moment relaxes to the value induced by the magnetic field following a Néel's process [Néel, 1949], which must be added to the rotation of the magnetic moment alongside the colloid rotation to obtain the full dynamic equation of the magnetic moment:

$$\dot{\vec{m}} = \vec{\omega} \times \vec{m} + \frac{\chi\vec{H} - \vec{m}}{\tau} \tag{2.4}$$

with χ being the product of the magnetic susceptibility of the particle times the volume of the magnetic domain, τ being Néel's relaxation time and $\vec{H}$ being the other magnetic field, which we will simply relate with $\vec{B} = \mu\vec{H}$.

The value of τ allows us to distinguish two limiting cases. When $\tau \to 0$, the magnetic moment relaxes immediately to the magnetic field and it becomes

independent of the particle rotation. On the other hand, when $\tau \to \infty$, we can suppress the relaxation term from equation (2.4) we recover the ferromagnetic model (equation 2.2).

Combining equations (2.1) and (2.4) alongside the form of the magnetic field, with our unknowns being m_0, ω and Φ, we obtain this set of three independent equations:

$$\begin{aligned} \omega &= \frac{m_0 B_0}{8\pi\eta a^3} \sin\Phi \\ \tan\Phi &= -\tau(\Omega + \omega) \\ m_0 &= \chi H_0 \cos\Phi \end{aligned} \tag{2.5}$$

Combining these three equations, we end up obtaining a cubic equation for $\tan\Phi$:

$$\tan^3\Phi + \tau\Omega\tan^2\Phi + \tan\Phi\left(1 + \frac{\chi\mu H_0^2\tau}{8\pi\eta a^3}\right) + \tau\Omega = 0 \tag{2.6}$$

This equation has at least a real solution for any positive value of Ω, hence the particle will be capable of rotating with a constant angular velocity for all the frequency domain. Unlike for the ferromagnetic model, this angular velocity will not be equal to the frequency of the external magnetic field. Curves $\omega(\Omega)$ always present a maximum, but are not necessarily continuous, since there can be discontinuous jumps between the three solutions of the cubic equation.

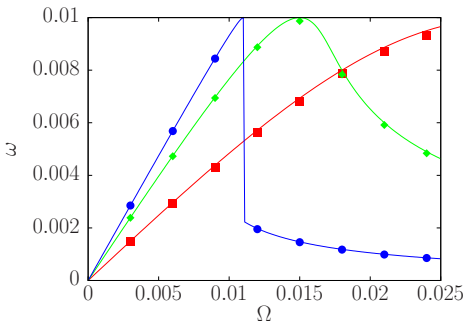

Figure 2.3: Angular velocity ω as a function of external field frequency Ω for $\tau = 50$ (red), $\tau = 200$ (green) and $\tau = 1000$ (blue). LB points are represented as solid figures, while our model predictions are represented in solid lines. Results are expressed in LB units.

In figure 2.3 we can see three representative curves $\omega(\Omega)$ varying the value of τ. For low values of τ (red curve), the particle rotates much slower than the applied magnetic field, and presents its maximum at a very high value of the frequency. For high values of τ (blue curve), the particle rotates with an angular velocity very close to that of the applied magnetic field, until it reaches a maximum and there is a sudden discontinuity; however, in contrast to the ferromagnetic case, at high frequencies the particle keeps rotating with a constant,

though very small angular velocity. For the intermediate case (green curve), there is also a change in the solution of the cubic equation (2.6) we take past the maximum, but unlike for the blue curve it is continuous.

2.1.3 Magnetic rotors with superparamagnetic domains

The presence of several paramagnetic domains in "Dynabeads®" colloids, with different τ associated to each one, allows them to have an interesting response to a rotating magnetic field, resulting from a mixture of the behaviours we have exposed. In plain words, they can rotate with $\omega \simeq \Omega$ for low frequencies of the applied field, and eventually reach an almost constant angular velocity at high frequencies. These inhomogeneities in relaxation times are due to size inhomogeneities of the magnetic domains inside particles; τ is proportional to the domain volume [Néel, 1949]. We can consider that the size of the paramagnetic domains follows a log-normal law [Janssen et al., 2009] and use this continuum description to characterize the magnetic material inside each colloid.

Using this model, $\vec{m}$ in equation (2.1) turns into $\vec{m} = N \int \vec{m}(r) f(r) dr$, where N is the number of domains into the system, $f(r) = \frac{1}{r\sigma\sqrt{2\pi}} \exp\left(-\frac{(\ln r - \ln \bar{r})^2}{2\sigma^2}\right)$ a log-normal distribution, characterized by the mean radius of the particles $\bar{r}$ and a standard deviation σ. Equation (2.4) must now be applied individually to each domain. Not only $\vec{m}$ is a function of the domain size, but also $\chi(r) = \chi_0 4\pi r^3/3$, which we already defined as a product of the magnetic susceptibility χ_0 times the domain volume, and the relaxation time, given by Néel's expression $\tau(r) = \tau_0 \exp\left(\frac{KV}{k_B T}\right)$, with τ_0 being an attempt time, V the domain volume, K the anisotropy constant, and $k_B T$ the thermal energy, which we can simply rewrite as $\tau(r) = \tau_0 \exp(\alpha r^3)$. Combining this set of $N+1$ equations, we obtain an implicit equation for the angular velocity of the particle:

$$\omega = -\frac{\mu H_0^2 N}{8\pi\eta a^3} \int \frac{f(r)\chi(r)\tau(r)(\Omega+\omega)}{1+\tau^2(r)(\Omega+\omega)^2} dr \tag{2.7}$$

We can work with a dimensionless version of equation (2.7) using the following parameters: $\tilde{r} \equiv r/\bar{r}$, $\tilde{\alpha} \equiv \alpha \bar{r}^3$, $\Omega^\star \equiv \mu H_0^2 N \chi_0 \bar{r}^3/6\eta a^3$, $\tilde{\omega} \equiv \omega/\Omega^\star$ and $\tilde{\tau}_0 \equiv \tau_0 \Omega^\star$.

$$\tilde{\omega} = -\int_0^\infty \frac{d\tilde{r}}{\sigma\sqrt{2\pi}} \frac{\tilde{r}^2 \tilde{\tau}_0 \exp(\tilde{\alpha}\tilde{r}^3)(\tilde{\Omega}+\tilde{\omega})}{1+\tilde{\tau}_0^2 \exp(2\tilde{\alpha}\tilde{r}^3)(\tilde{\Omega}+\tilde{\omega})^2} \exp\left(-\frac{(\ln \tilde{r})^2}{2\sigma^2}\right) \tag{2.8}$$

This model depends on a large number of parameters, which can affect the shape of the resulting $\omega(\Omega)$ curve. Reference [Janssen et al., 2009] provides most of the physical values of the involved quantities, summarized in table 2.1. With these values, $\tilde{\alpha} \approx 3$ and $\Omega^\star \approx 8.5 \cdot 10^7 B_0^2 \mathrm{s}^{-1}$ (B_0 given in Teslas (SI)). The quantity τ_0 is the inverse of the attempt frequency for superparamagnetic materials, which is of the order of gigahertz. We test it by comparing the experimental data presented in there with measurements provided by Fernando Martínez Pedrero and the numerical resolution of equation (2.8) in figure 2.4.

μ	$4\pi \cdot 10^{-7}$
$\bar{r}$	$3.8 \cdot 10^{-9}$
σ	0.26
ξ_0	0.64
α	$\approx 5 \cdot 10^{25}$

Table 2.1: Physical values of quantities involved in the model provided by [Janssen et al., 2009]. Non dimensionless quantities are provided in SI units.

Our model is capable of recovering the general behaviour found experimentally, with a first region where $\Omega \simeq \omega$ followed by a region of slower growth (which eventually reaches a maximum at very high frequencies). However, we cannot find the regime change for frequencies as high as the experimental ones choosing $\tilde{\alpha} = 3$, thus we tried higher values to find curves closer to the experimental data. Both pairs of data sets are coincidental with themselves once we reduce the frequency and angular velocity units, but differ from each other. Discussing the causes with Fernando Martínez Pedrero, he concludes the different experimental set-up, with the one he used being able to create more homogeneous magnetic fields but not reaching frequencies as high, would be the main source of discrepancy between both experiments. His curves have a shape closer to that of the ones we obtain with our model, which do not possess the first maximum observed in [Janssen et al., 2009] when there is the regime change. The behaviour at high frequencies observed by them though is qualitatively compatible with the model.

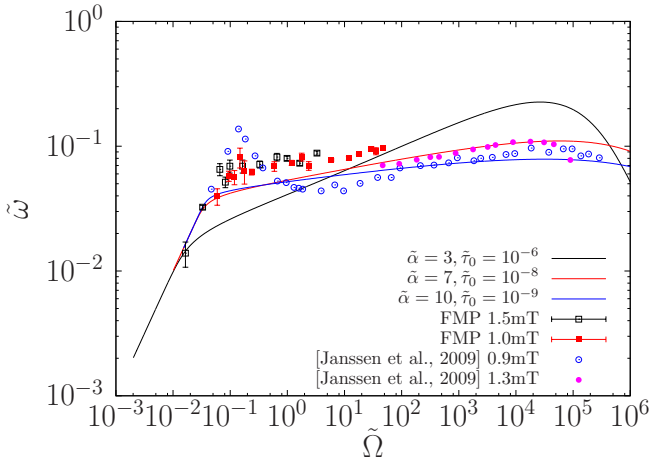

Figure 2.4: Dimensionless angular velocity $\tilde{\omega}$ as a function of dimensionless external field frequency $\tilde{\Omega}$. We display three curves obtained as solutions of equation (2.8), two experimental data sets for different applied magnetic fields provided by Fernando Martínez Pedrero and the two data sets at different applied magnetic fields found in [Janssen et al., 2009].

Overall, we can conclude that the nanoscopic structure of magnetic colloids has a critical effect on their mesoscopic motion. The approach we presented to describe the rotation of magnetic colloids can capture this fact.

2.2 Dynamic equations of a system of magnetic rotors

In section 1.2.8 we introduced the dynamic equations for a system of interacting point particles in a fluid in equation 1.31, which we reproduce below:

$$\dot{\vec{x}}_i = \vec{u}(\vec{x}_i) + \frac{1}{\gamma}\sum \vec{F}^{ext}$$

We will particularize it for a system of magnetic rotors. Let us consider a collection of N spherical magnetic rotors of radius a, at positions $\vec{x}_i = (x_i, y_i, h_i)$, immersed in a fluid with a solid boundary at $h = 0$, rotating with constant angular velocity ω. Each colloid possesses a magnetic moment $\vec{m}$, which for simplicity we will assume rotates synchronously with the magnetic field with an angular velocity Ω. As we saw in the previous section, ω and Ω do not necessarily need to have the same value.

Equation 1.31 states the velocity of a particle will be given by the flow $\vec{u}$ at its position plus a term proportional to the external forces acting on it. The velocity field at the particle position has two main contributions. Each rotor at position $\vec{x}_j$ creates a flow $\vec{u}_j^{rot}$ that due to the presence of a wall at height h is given by equation 1.24. Then, if those particles are subjected to any force, they will create an additional flow $\vec{u}_j^{for_k}$, given by equation 1.23; subindex k in superindex for takes into account that many forces can be acting on the same particle, each of them adding their own stokeslet contribution. Summing all flow contributions evaluated at $\vec{x}_i$, we obtain the velocity field at that position:

$$\vec{u}(\vec{x}_i) = \sum_{j\neq i}\left(u_j^{rot}(\vec{x}_i) + \sum_k u_j^{for_k}(\vec{x}_i)\right) \tag{2.9}$$

Forces acting on colloids do not only contribute to the flow they create, but also add an additional contribution to their velocity proportional to those forces and the colloid mobility, which in an unbound fluid is given by $(6\pi\eta a)^{-1}$. Let us discuss which forces can act on our colloids more thoroughly.

2.2.1 Forces acting on magnetic colloids

We can divide forces acting on magnetic colloids in two types: body forces acting individually on each particle, and interaction forces derived from a particle-to-particle potential acting on a pair of colloids.

Gravity is the main body force acting on colloids. For the case of particles immersed in a fluid, the gravity force is proportional to the density mismatch between the particle and the fluid $\Delta\rho$ and the particle volume $V = 4\pi a^3/3$, $F_g = \Delta\rho V g$. Magnetic colloids are typically denser than water and will sediment

to the solid substrate. There, we expect a repulsive electrostatic interaction $F_{es} = \frac{A}{\lambda}e^{-h/\lambda}$ arising from the charge of the particle and the bounding plate, with A being a prefactor that depends on the surface charge density and λ the Debye screening length. The force balance between gravity and electrostatic repulsion defines an equilibrium height h_0 at which colloids remain. For small displacements from h_0, we can derive an effective elastic force with a coupling constant given by $K = \frac{gV\Delta\rho}{\lambda}$. Therefore, the resulting force is:

$$\vec{F}_g = -K(h - h_0)\hat{z} \tag{2.10}$$

We use this vertical force as the effective confinement force magnetic colloids are subjected to.

Two magnetic moments will interact with each other via a dipole-dipole interaction. The dipolar force on a colloid i with magnetic moment $\vec{m}_i$ at position $\vec{x}_i$ due to the effect of colloid j with magnetic moment $\vec{m}_j$ at $\vec{x}_j$ is:

$$\begin{aligned}\vec{F}_{dp,i} = \frac{3\mu_0}{4\pi|\vec{r}_{ij}|^4}\left[(\hat{r}_{ij}\times\vec{m}_i)\times\vec{m}_j + (\hat{r}_{ij}\times\vec{m}_j)\times\vec{m}_i - 2\hat{r}_{ij}(\vec{m}_i\cdot\vec{m}_j)\right.\\ \left.+5\hat{r}_{ij}\left((\hat{r}_{ij}\times\vec{m}_i)\cdot(\hat{r}_{ij}\times\vec{m}_j)\right)\right]\end{aligned} \tag{2.11}$$

where $\vec{r}_{ij} = \vec{x}_j - \vec{x}_i$ is the relative position between both particles, $\hat{r}_{ij} = \vec{r}_{ij}/|\vec{r}_{ij}|$ the unitary vector along that direction and μ_0 the magnetic permeability. The dipolar force on colloid j due to colloid i will have the same value with opposite sign.

Magnetic dipolar force is highly anisotropic. In figure 2.5 we display the three components of the dipolar force for two particles with magnetic moments rotating synchronously with the magnetic field $\vec{m} = m_0(\cos\Omega t, 0, \sin\Omega t)$, during a field period. In panel (a), we consider the case in which both particles are aligned along the x direction. Components x and z of the force oscillate during the field period. On average, the z component is null while the x one is attractive, ensuring particles remain aligned this way. In panel (b), we consider both particles are aligned along the y direction. In that case, components x and z are null and particles repel from each other.

Quantifying the relative importance of each of these forces is crucial in order to know when one will be dominant over the other. In order to do so, we made up two dimensionless parameters, $F_{g/h}$ and $F_{m/h}$, which allow us to quantify their importance respect to hydrodynamic interactions. We have defined these quantities as:

$$\begin{aligned}F_{g/h} &= \frac{4K}{3\pi\omega\eta a}\\ F_{m/h} &= \frac{\mu_0 m_0^2}{32\pi^2\omega\eta a^6}\end{aligned} \tag{2.12}$$

$F_{g/h}$ offers an estimation of the degree of confinement of particles in the z direction. Viscous force is evaluated for a sphere moving in an unbound fluid

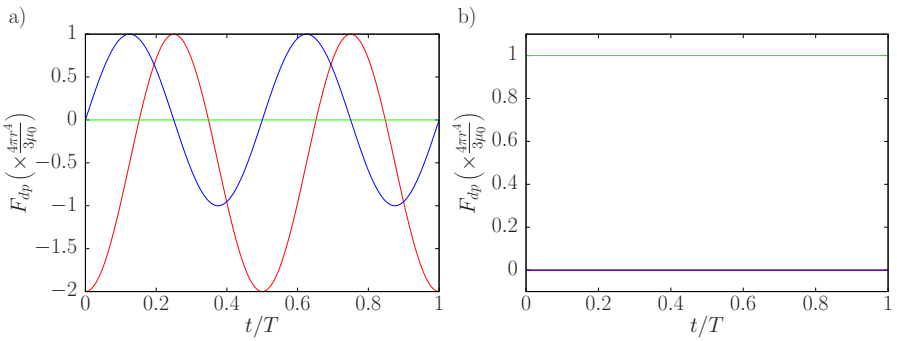

Figure 2.5: Temporal evolution during a field period of the magnetic dipolar force components (x in red, y in green and z in blue) for **(a):** Two particles aligned along the x direction. **(b):** Two particles aligned along the y direction. Negative (positive) sign indicates the force is attractive (repulsive).

with velocity $\omega a/8$ and the effective gravity for a particle that has displaced a distance a from its equilibrium height. These reference values are taken from approximations to results later found in the thesis (the velocity of a rotor moving close to a wall and the typical vertical displacement for a pair of them), which we arbitrarily take to make up this definition; this quantity is intended to have just an indicative estimation of the confinement in the system, and not a precise measurement of it.

$F_{m/h}$ can be related to the well-known Mason number, as it is just its inverse. Mason number was first introduced by Mason [Allan and Mason, 1962] to measure the ratio between viscous and electric forces in the study of the deformation and burst of liquid drops suspended in liquid dielectrics in an electric field. Later on, the same concept has been used on the field of magnetorheology [Melle et al., 2003, Klingenberg et al., 2007].

2.3 Simulating systems of magnetic rotors

In the previous section we introduced the dynamic equations for a system of magnetic colloids. The fact we need to not only solve the dynamics of the particles but also that of the magnetic moment doubles the complexity of the problem. As discussed in section 1.3, the numerical resolution of the dynamics of systems of interacting particles scales as $\sim 2N^2$ with the number of particles in the system N. Therefore, LB becomes the most suitable method to deal with the simulation of this kind of systems.

We begin this section by giving a brief explanation on how the magnetic models and the forces acting on the colloids have been included into our LB code. Then, we have carried out some tests on isolated particles to test their rotation and compare it to the models. For the case of ferromagnetic particles, we can test the behaviour of particles in the asynchronous regime, and check whether $\langle\omega\rangle$ follows the behaviour found in the literature [Helgesen et al., 1990].

These tests also have allowed us to make calibrations of the effective hydrodynamic radius of colloids in our LB code.

2.3.1 Introducing magnetism and interactions into LB

To introduce the magnetic models into our LB code we have to make it solve equations (2.1) and either equation (2.2) for ferromagnetic particles or (2.4) for paramagnetic ones. We attach to each colloid a new vectorial magnitude representing its magnetic momentum. By making the curl product of the magnetic moment with a magnetic field defined *ad hoc* for this application, we can compute the magnetic torque. The LB code is already prepared to deal with the computation of the hydrodynamic component of the torque (see section 1.3.1), thus we only had to add this newly computed magnetic component to the total torque experienced by each particle and let it operate normally. This deals with equation (2.1), although LB does not nullify inertial effects, which could be present with an inappropriate choice of Re. Once the resulting angular velocity of the particle is computed, it can be used to rotate the magnetic moment as described by equation (2.2). We introduce the extra term from Néel's relaxation process given by equation (2.4) by updating the magnetic moment before computing the magnetic torque.

Introducing forces in LB is pretty straight forward. Similarly as each colloid already had a torque vector associated, which was then used to rotate it through a molecular dynamics step, there is an equivalent for forces, which is used to update its position. Before computing its final value, we may add as many additional contributions as we wish. In this case, we introduce the vertical confinement force and the magnetic dipolar interaction, which depends on the magnetic moment of the colloid as well. The parallelization of LB does not allow us to have unlimited[2] reach for pair-wise forces, such as the dipolar interaction, as particles can only interact with those which fall a distance equal to the length of the cells we divide our system into. We do not consider this to be a big liability for the dipolar interaction, since it goes $\sim r^{-4}$.

2.3.2 Testing magnetic colloids in LB

In order to test the ferromagnetic model in our LB code, we fix the position of a single colloid of radius 3.7 and a magnetic moment of value 1 centred in a node of the lattice, with a fluid with viscosity 0.1 and an applied magnetic field of 3.6, which gives a threshold frequency $\Omega_C = 0.02$, which allows us to have enough temporal resolution.

In figure 2.6 (a) we show that our LB code is capable of recovering the predicted behaviour for $\omega(\Omega)$ in the synchronous region below Ω_C. However, the threshold frequency Ω_C we find with LB is $\sim 96\%$ of the expected value. We can attribute this small divergence to a not fine enough calibration of the hydrodynamic radius. For points above Ω_C, ω no longer has a constant

[2] As far as unlimited can go in a finite simulation system.

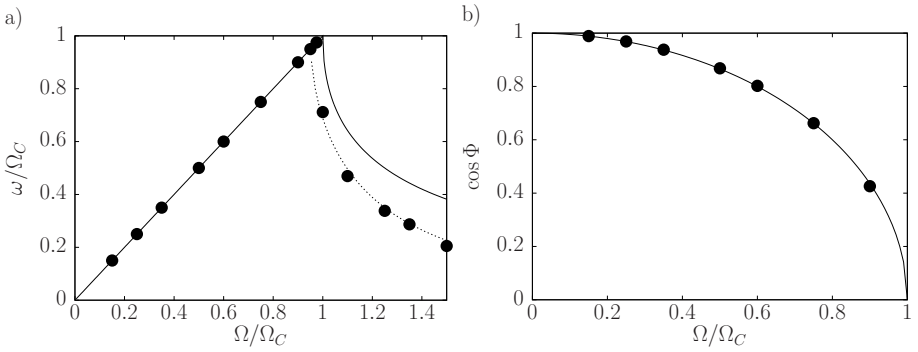

Figure 2.6: (a): Angular velocity ω as a function of external field frequency Ω. LB points are represented with dots, model prediction with solid line. Alternative fit for the asynchronous region plotted in dashed line. **(b):** Cosine of the phase shift $\cos\Phi$ as a function of external field frequency Ω. LB points are represented with dots, model prediction with solid line. All frequency units normalized respect Ω_C.

value and we represent the time average angular velocity of the particle instead. We compare this to the predicted behaviour in the asynchronous region $\langle\omega\rangle = \Omega(1 - \sqrt{1-(\Omega_C/\Omega)^2})$ [Helgesen et al., 1990]. The LB points clearly fall well below this prediction. An alternative fitting function $\langle\omega\rangle = \Omega_C(1 - \sqrt{1-(\Omega_C/\Omega)^2})$[3], offers a better agreement with the LB data. In figure 2.6 (b) we also represent the phase shift of the magnetic moment respect the magnetic field. This magnitude only makes sense when $\Omega < \Omega_C$ and ω is constant. For the chosen values of the simulation there is perfect agreement between theory and simulations.

However, if we vary the viscosity η of the fluid while keeping Ω_C constant, the agreement in the phase shift between the model and LB simulations vanishes. We can use this to calibrate the effective hydrodynamic radius of the colloids in the LB simulation as a function of the fluid viscosity, by attributing the discrepancy in the phase shift to a divergence between nominal and hydrodynamic radius. We made this calibration for colloids of nominal radius $a_0 = 3.7$. In figure (2.7)) we compare the results we obtained with Ladd's calibration [Ladd, 1994b] for spheres of nominal radius $a_0 = 4.5$ by measuring their drag coefficient. Overall there is a good matching between both data sets, which follow similar trends, indicating the goodness of our procedure to determine the hydrodynamic radius.

We have also tested the LB code for the simple paramagnetic model, as already shown in figure 2.3. Similarly as we did for the ferromagnetic model, we placed a fixed particle of radius 3.7 and $\chi = 0.278$ with its center in a node of the lattice, in a fluid of viscosity 0.1 and an applied magnetic field of amplitude 3.6. We take $\mu = 1$, so fields $\vec{B}$ and $\vec{H}$ are completely exchangeable in our simulations. We tested three values of τ, 50, 200 and 1000, which covered the spectre from the short relaxation time to long relaxation time behaviour. The

[3]Sometimes there are typos writing equations leading to results too good to be true.

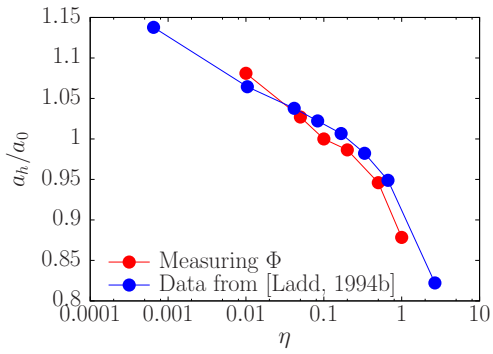

Figure 2.7: Effective hydrodynamic radius a_h normalized by nominal radius a_0 as a function of viscosity η (in LB units) for LB simulations. Method proposed measuring relative phase shift between magnetic moment and field in red, data from [Ladd, 1994b] in blue.

LB simulations are capable of recovering the predictions made by the model, and in general LB points fall on the theoretical curves, although agreement is slightly lost at the highest frequencies we tested, probably due to lack of temporal resolution.

2.4 Conclusions

We have introduced basic models to describe the rotation of a magnetic colloid, and the methods to better simulate them. For our future research goals, in which the magnetic properties of our colloids are not as important as the fact that they are capable of rotating with a constant angular velocity, the use of the ferromagnetic model is preferred to paramagnetic models, due to its simplicity. However, we should not overlook at the possibilities the introduction of paramagnetic particles can offer us; by tuning the relaxation time τ, we can obtain a collection of particles rotating with inhomogeneous angular velocities for the same applied field. Were this peculiarity interesting to study phenomena such as angular velocity synchronization, our LB code would be equipped to deal with it. The simulation of magnetic colloids in LB has allowed us to calibrate a more basic aspect of colloid simulations, as is the hydrodynamic radius, obtaining results comparable to the known literature [Ladd, 1994b].

Finally, we should not forget about the more analytical treatment we did in this chapter. The numerical resolution of equations of the form of equation 1.31 once there are interacting forces between particles has a very poor scaling with the number of particles N, thus making it ill advisable. Furthermore, in the case of magnetic colloids we should add the coupling of the magnetic moment to the particle motion, which increases the complexity even more. However, being able to write such equations explicitly can prove useful, as we will show in chapter 3. We also introduced the dimensionless parameters $F_{g/h}$ and $F_{m/h}$, which relate confinement and magnetic interactions to viscous forces. We will

use them throughout the rest of the thesis to estimate the relative importance of each force contribution to a system of magnetic colloids.

Chapter 3

Arrays of magnetic rotors

The simplification of anything is always sensational.

G. K. Chesterton

In the previous chapter, we introduced the magnetic dipolar force (equation 2.11), which acts between two magnetic moments. This force depends on the relative orientation between the magnetic moments and their relative positions, which makes it highly anisotropic. It favours the alignment of magnets when their moments are parallel to the vector giving their relative position. This fact can be used at the colloidal scale to form arrays, which in the case of the most simple spherical colloids will be straight chains [Zerrouki et al., 2008]. These arrays can then be used as model artificial micro-swimmers [Dreyfus et al., 2005]. In [Dreyfus et al., 2005], colloids are attached to each other through DNA links. However, as posterior works show, magnetic dipolar force is enough to keep them cohesive [Sing et al., 2010, Martinez-Pedrero et al., 2015]; we must highlight that in order to favour the motion of colloids, oscillating fields are used in these two works. In some cases, it has been reported a dependence on particle length with applied frequency [Snezhko et al., 2005, Morimoto et al., 2008, Sing et al., 2010]. Besides its length, the shape of the array is also variable. The applied fields in [Sing et al., 2010], [Martinez-Pedrero et al., 2015] and [Martinez-Pedrero et al., 2018] are equivalent (all three experiments can be described with the schematic view we introduced in figure 2.2), yet the observed structures are completely different. These differences can be attributed to changes in the force balances (given by equation (2.12)) acting in all three systems. The flow created by these swimmers is also an interesting topic on its own. Colloidal walkers assembled by Katz's group [Sing et al., 2010] can transport large non-magnetic particles on top of a collection of them; similarly, the flow created by a single array can be used to pull a non-magnetic colloid [Massana-Cid et al., 2017].

In this chapter we study these arrays of magnetic colloids and the flows they create. It is divided into three sections. In the first one we introduce magnetic colloidal worms [Martinez-Pedrero et al., 2015], an unidimensional structure formed by an array of colloids moving at a constant distance from the interface. We will review the theoretical fundamentals that describe the kinematics of this structure and test them computationally, in order to provide this third leg of simulations to a work which already combines neat experiments with a theoretical model to back them up. In a second section we introduce an array which moves with its particles aligned in the y direction, which we named ribbons in [Massana-Cid et al., 2017]. This structure is not favoured by the magnetic dipolar interaction, thus we pose a scenario in which it is not present to model it. We study the behaviour of a pair of particles under these conditions by solving the explicit dynamic equations (equation (1.31)) numerically [Martinez-Pedrero et al., 2018]. We also compute the flow created by such an array [Massana-Cid et al., 2017]. Finally, in the third section we conduct a computational study to quantify the role of the different forces present in the system in determining the shape and motion mechanism of the formed arrays.

3.1 Magnetic colloidal worms

We define magnetic colloidal worms (simply worms) as arrays of colloidal rotors dynamically assembled and driven in a viscous fluid due to the action of an external oscillating magnetic field. Due to the presence of a close interface,

flow symmetry is broken and colloids can develop a self-propulsion velocity. Worms are aligned in the direction they propel due to the effect of the magnetic dipole-dipole interaction between their particles. Due to the additivity of the flux created by the particles, an array of colloids rotates faster than a single particle. Let us introduce the fundamentals that explain the hydrodynamic behaviour of this structure.

A rotor of radius a will create a flow around itself $\vec{u}$ given by equation 1.24. We can estimate its self-propelling velocity $\vec{v}$ by integrating the flux through its surface, normalized by its area.

$$\vec{v} = \frac{1}{4\pi a^2} \oint_{r=a} \vec{u} \cdot d\vec{S} \tag{3.1}$$

Considering a rotor with an angular velocity $\vec{\omega} = \omega\hat{y}$, it will develop a velocity with a non-zero x component:

$$\vec{v} = \frac{\omega a^3}{4h^2} \left(-(1-\xi) + \frac{\xi}{2} \left(\frac{a}{h} \right)^2 \right) \hat{x} \tag{3.2}$$

where $\xi = 1(0)$ for a solid(fluid) interface. It is noteworthy that depending on the type of interface, the self-propelling velocity will change its sign.

From here, we can jump to the study of the motion of an array of such rotors. Let us consider an array of N units aligned along the X axis, with a separation between them Δ and a distance to an interface h which remain constant as the structure displaces. Each of those particles creates a flow given by equation (1.24), in the coordinates relative to the centre of each of them. The flow created by the worm will be just the sum of the flow created by each particle. To compute its velocity, we will consider that the velocity of each particle will be given by their own self-propulsion velocity plus the flow created by the other particles of the worm at their position, then average all velocities to obtain the velocity of the centre of mass of the worm. The obtained velocities using this method are, for a liquid interface:

$$v(N) = v_{fluid}(1) \left(1 + \frac{1}{N} \sum_{i=0}^{N-1} \sum_{j \neq i} \frac{1}{((i-j)^2\epsilon^2 + 1)^{3/2}} \right) \tag{3.3}$$

and for a solid interface:

$$v(N) = v_{solid}(1) \left(1 + \frac{6h^2}{a^2 N} \sum_{i=0}^{N-1} \sum_{j \neq i} \frac{(i-j)^2\epsilon^2}{((i-j)^2\epsilon^2 + 1)^{5/2}} \right) \tag{3.4}$$

with $\epsilon \equiv \Delta/2h$ and $v_{solid(fluid)}(1)$ the velocity for a single particle given by equation (3.2) with $\xi = 1(0)$.

This hydrodynamic model showed a pretty good agreement with experiments in [Martinez-Pedrero et al., 2015] despite its simplicity. In that work, they measured the velocity of several worms to obtain a curve $v(N)$, and from it deduced a value of ϵ they compared to light scattering experiment in [Blickle et al., 2005] to check its compatibility.

3.1.1 Simulating worms with LB

LB simulations offer us more control over all the geometric parameters of the system (a, h and Δ) and the angular velocity of the particles ω, so we can make a direct comparison of the computed $v(N)$ with the theoretical prediction given by equation (3.4)[1]. The excess velocity $v(N) - v(1)$ of the worm respect a single particle only depends on dimensionless parameters N and ϵ, thus we can work with LB units without losing generality. We have tested the model with colloids of radius $a = 3.7$, rotating with angular velocity $\omega = 0.002$ in a fluid of viscosity $\eta = 0.5$, thus the hydrodynamic effective radius is $a_h = 3.4$ (see figure 2.7), in a system with $L_y = L_z = 80$ LB nodes of section, and a variable length L_x depending on how long is the worm, with periodic boundary conditions in X and Y and solid boundaries in Z. Each colloid is centred at a node of the lattice, at distance $h = 5.5$ to the closest boundary and $\Delta = 9$ between their centres; this is the closest way to allocate them while leaving at least a free node of fluid between each colloid and the wall and between each other, which prevents us from dealing with lubrication effects. We do not update their positions at every time step in order to keep ϵ constant as the model assumes.

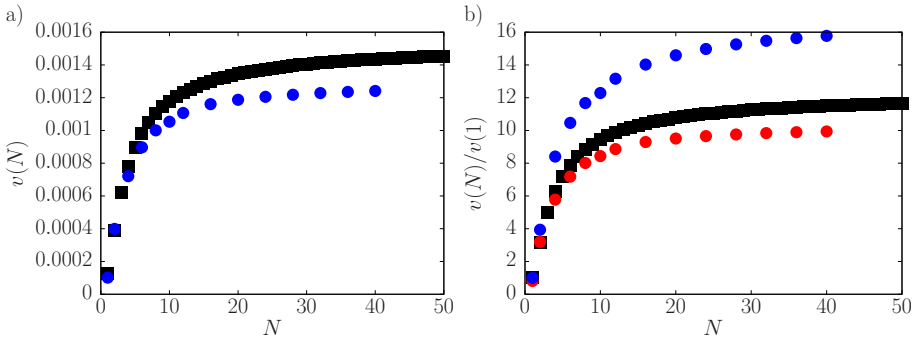

Figure 3.1: (a): Average velocity v of a worm as a function of its number of particles N. In black squares, theoretical prediction (equation (3.4)), in blue circles LB results. Results given in LB units. **(b):** Average velocity v of a worm as a function of its number of particles N normalized by the velocity of a single particle $v(1)$. In black squares, theoretical prediction, in red circles LB normalized by theoretical $v(1)$ (given by equation (3.2)), in blue circles normalized by $v(1)$ measured in LB simulations.

In figure 3.1 we can see that the simulation and the theory have the same qualitative behaviour, as both are monotonously growing curves with the worm length N which asymptotically saturate. However, there is a slight discrepancy between their numerical values. In panel (a) we consider the absolute value of the velocities; in that case, the theoretical prediction, given by equation (3.4) (black squares) throws a slightly larger value of the velocity of a worm than the ones we find in LB simulations (blue dots). Panel (b) gives us insight on the physical origin of this discrepancy, by plotting the normalized velocities. Paradoxically, in that case the simulated values (blue dots) reach larger values

[1] We will limit the LB simulations to the solid boundary.

than the theoretical prediction (black squares)[2]. LB results are more affected by the wall friction, therefore $v(1)$ reaches a lower value, while the hydrodynamic cooperative effects which lead to the worm increase of velocity are more intense than what the initial model predicts, thus the relative increase in velocity is larger.

In order to normalize LB data, we measured the velocity of a single particle in a system of the same size of the one we used to simulate the whole worm. We found a dependency $v(1)(L_x)$, and more concretely that it decreases with L_x, as seen in figure 3.2. A first hypothesis to explain this behaviour is attributing it to periodic boundary conditions in our simulation: the same phenomena that leads to an increase of the velocity of a worm respect to the velocity of a single particle, could make a particle separated a small L_x from the image system move faster than one located at a large L_x. We explore this fact more thoroughly in appendix A.

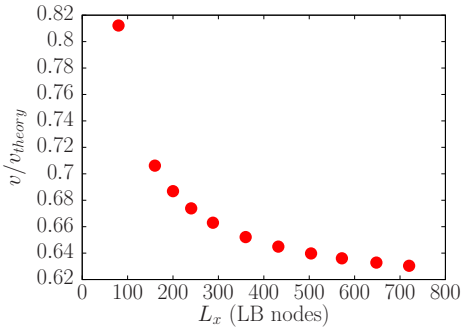

Figure 3.2: Velocity of a colloid in a system of size $L_x \times 80 \times 80$ normalized by the theoretical velocity (equation (3.2)).

Summarizing, LB simulations have allowed us to test the validity of the theory introduced in [Martinez-Pedrero et al., 2015] at giving a first explanation to the increase in the velocity at which an array of colloids can displace respect to an isolated colloid. That model (equations (3.2), (3.3) and (3.4)) is based on a far field theory, which should be capable of reproducing the asymptotic behaviour of the system. We can attribute the discrepancies observed between simulation and model mainly to near field effects simulations can capture, and partly to simulation finite system size effects. These discrepancies have resulted in an overestimation of the velocity of a single particle due to increased friction near the interface and an underestimation of the cooperative effect that accelerates worms.

[2]Red dots have been normalized by the theoretical velocity and their comparison to the theoretical curve is equivalent to the description we did of panel (a).

3.2 Magnetic colloidal ribbons

The assembly of worms is dominated by the alignment interaction due to magnetic dipole-dipole force between colloids. However, it is also possible to observe the assembly of similar structures due to hydrodynamic interactions. This is the case for what we have called magnetic colloidal ribbons (or simply ribbons), structures formed by an array of colloids aligned perpendicular to the direction of their movement (aligned in y using our coordinates convention). To study how hydrodynamic interactions favour the formation of this kind of aggregates, we have focused in the case of two particles, combining experiments and theory shown in [Martinez-Pedrero et al., 2018].

The experimental system we model is formed by ferromagnetic hematite microparticles driven above a plane by an external rotating magnetic field. These particles are "peanut" shaped, with a long (short) axis of length $a = 2.5\mu$m ($b = 1.4\mu$m). When diluted in highly deionized water, particles are heavy enough to sediment onto a solid glass substrate, and big enough to neglect the small Brownian motion they display. Despite we could initially suspect the shape of the particles could have an important role in the phenomena we will be exposing, we did not take it into consideration and it was just used to easily identify the direction of their magnetic moment, which is aligned along the short axis. A circularly oscillatory magnetic field as the one described in chapter 2 is applied to a suspension of such particles.

In order to form pairs of interacting particles, moderately large densities are required, at which close particles can interact due to magnetic and viscous forces. By varying the frequency of the applied magnetic field, the observed dynamic state of the system can be changed, distinguishing two separate regimes. At low frequencies ($\Omega \lesssim 125.7\text{rads}^{-1}$), the propellers tend to arrange parallel to the direction of their motion (worm-like), with their short axis aligned. At high frequencies, the pair exhibits a completely different bound state, in which particles align perpendicular to their direction of motion (ribbon-like), aligned along their long axis. The ferromagnetic nature of the particles sets an upper limit in frequency to this later regime, since there is a critical frequency above which the particles no longer rotate with constant angular velocity (see section 2.1.1).

The arrangement observed in the first regime is favoured by the magnetic dipolar interaction (see section 2.2.1), which should prevent the formation of the one observed in the second one. We can put forward a simple argument to explain these different arrangements from changes in magnitude of the competing forces acting on the pair. The balance between magnetic and viscous forces acting on the particle is given by the parameter $F_{m/h}$ introduced in section 2.2.1 (equation 2.12). This quantity is inversely proportional to the angular velocity the particles rotate with, thus indicating that for fast rotating particles, viscous forces will dominate over magnetic ones; therefore, the second arrangement is favoured by hydrodynamic interactions. To put up numbers, for $\omega \approx 30\text{s}^{-1}$, $F_{m/h} \approx 1$, while the experiments carried out in [Martinez-Pedrero et al., 2018] were performed with ω ranging between 125s^{-1} and 500s^{-1}.

We model the propelling couple as a pair of rotating solid spheres of radius a_i above a solid wall at distance h_i in the z direction rotating with a constant angular velocity ω_i pointing in the y direction. We can approximate the velocity of a colloid by the sum of its self-propulsion velocity (equation (3.2)) and the flow created by its neighbour, which we can compute using equation (1.24). We can as well define a new set of coordinates, $\vec{x}_{CM} \equiv \frac{\vec{x}_1+\vec{x}_2}{2}$ and $\vec{x}_{rel} \equiv \frac{\vec{x}_2-\vec{x}_1}{2}$, to measure centre of mass and relative positions and velocities instead of absolute ones. Then, if we consider identical particles (*i.e.* $a_i \equiv a$ and $\omega_i \equiv \omega \ \forall i$), the position of the centre of mass of the system and the relative semidistance of the two particles will evolve with velocities given by:

$$\begin{cases} v_{x,CM} = \dfrac{\omega a^5}{16}\left(\dfrac{1}{(z_{CM}-z_{rel})^4}+\dfrac{1}{(z_{CM}+z_{rel})^4}\right)+\dfrac{3\omega a^3 z_{CM}x_{rel}^2}{4(x_{rel}^2+y_{rel}^2+z_{CM}^2)^{5/2}} \\ v_{x,rel} = \dfrac{\omega a^5}{16}\left(\dfrac{1}{(z_{CM}+z_{rel})^4}-\dfrac{1}{(z_{CM}-z_{rel})^4}\right)+\dfrac{\omega a^3}{4}\left(\dfrac{3z_{rel}x_{rel}^2}{(x_{rel}^2+y_{rel}^2+z_{CM}^2)^{5/2}}+\right. \\ \qquad \left.\dfrac{z_{rel}}{(x_{rel}^2+y_{rel}^2+z_{rel}^2)^{3/2}}-\dfrac{z_{rel}}{(x_{rel}^2+y_{rel}^2+z_{CM}^2)^{3/2}}\right) \\ v_{y,CM} = \dfrac{3\omega a^3 x_{rel}y_{rel}z_{CM}}{(x_{rel}^2+y_{rel}^2+z_{CM}^2)^{5/2}} \\ v_{y,rel} = \dfrac{3\omega a^3 x_{rel}y_{rel}z_{rel}}{(x_{rel}^2+y_{rel}^2+z_{CM}^2)^{5/2}} \\ v_{z,CM} = \dfrac{3\omega a^3 x_{rel}z_{rel}z_{CM}}{(x_{rel}^2+y_{rel}^2+z_{CM}^2)^{5/2}} \\ v_{z,rel} = \dfrac{\omega a^3}{4}\left(\dfrac{x_{rel}}{(x_{rel}^2+y_{rel}^2+z_{CM}^2)^{3/2}}-\dfrac{x_{rel}}{(x_{rel}^2+y_{rel}^2+z_{rel}^2)^{3/2}}+\dfrac{3z_{CM}^2x_{rel}}{(x_{rel}^2+y_{rel}^2+z_{CM}^2)^{5/2}}\right) \end{cases} \tag{3.5}$$

Inspecting equation (3.5), we quickly realize that if the pair are at the same height ($z_{rel} = 0$) and are aligned along y ($x_{rel} = 0$), all the components of the relative position turn zero, thus only the centre of mass of the particle displaces along the x direction. This shows that the ribbon configuration is a steady point for the relative coordinates. However, a linear stability analysis of the system did not prove that this relative configuration was stable (see appendix B).

The numerical resolution of equation (3.5) reveals the formation of bound states resulting of the combination of the translation of the centre of mass of the system along x and a cyclic closed trajectory for the relative position of the particles. We display some of these trajectories in figure 3.3. As can be easily inferred from the equations, the closer the particles are to the wall, the faster they displace. As we already saw, the wall is necessary to ensure the translation of rotors, and the friction when approaching it and other near field effects are not considered. Despite that, we have observed that for cases in which the particles are very close to the wall, a non-zero $v_{CM,y}$ component appears. The amplitude of the periodic relative motion decreases with the angle the particles form when they are at the same height (which we use as our initial condition), and it vanishes when particles are aligned along the y direction and they remain in this relative position.

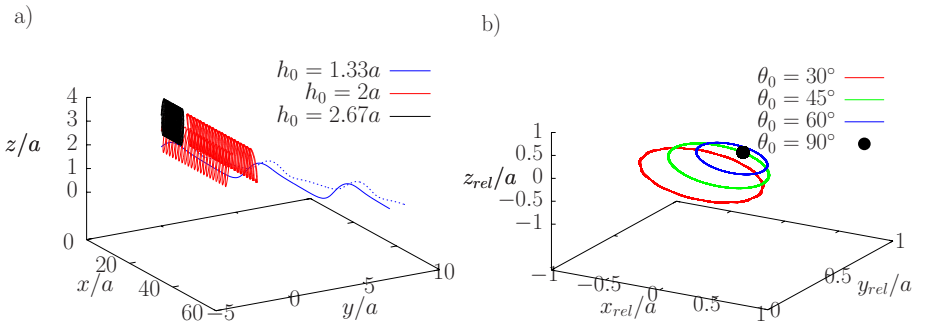

Figure 3.3: (a): Trajectories in absolute coordinates of the pair of particles at several starting heights ($h_0 = 1.33a$ in blue, $h_0 = 2a$ in red, $h_0 = 2.67a$ in black) depicting the leap frog motion for an initial condition with $\Delta_0 = 2.36a$ and a relative angle $\theta = 45°$. Black and red curves last the same amount of time, while blue curve has been cut. **(b):** Trajectories in relative coordinates of the pair of particles for several initial angles ($\theta_0 = 30°$ in red, $\theta_0 = 45°$ in green, $\theta_0 = 60°$ in blue and $\theta_0 = 90°$ in black) for an initial condition with $\Delta_0 = 2.36a$ and $h_0 = 2a$.

To experimentally test the model given by equation (3.5), the average translational speed $\langle v_{CM} \rangle$ of a pair of particle in a bound state was measured. More particularly, the components parallel ($\langle v_{CM,x} \rangle$) and perpendicular ($\langle v_{CM,y} \rangle$) to the propulsion direction (x-axis) imposed by the rotating field. Both quantities, normalized with respect to the speed of a single propeller $\langle v_0 \rangle$, are plotted versus the positional angle θ in figure 3.4, and at different center to center distances Δ. The image shows the comparison between the experimental data (symbols) and the analytical results (continuous line) which were plotted assuming that the conditions assumed for (3.5), *i.e* both particles have the same elevation, $h \sim 1\mu$m and rotate with the same angular velocity, $\omega_{1,2} = 502.6\,\text{rads}^{-1}$. The data and the fits show that along the propulsion direction, the pair of particles decreases their average speed with the angle θ, being the configuration where the relative position is perpendicular to the long axes of the particle the fastest one. The behaviour of the perpendicular component also illustrates the tendency of the pair to have a higher transversal velocity at intermediate angles, in agreement with the experimental observation where pair of propellers were found to speed up when placed at $\theta \sim 45^0$. Despite all the approximations made to obtain equation (3.5), we found quantitative agreement with the experimental data, as the model well captures the physical mechanism behind the hydrodynamic interactions in these bound states.

We also considered the effect of gravitational effects to the pair of particles with the treatment described in section 2.2.1 (which led to equation (2.10)). Gravitational effects must be included both as external forces and as an extra stokeslet term in equation (1.31), which describes the complete motion of the pair of particles. Their relative importance respect viscous forces is given by dimensionless parameter $F_{g/h}$ (equation (2.12)). We expect that given the small values of the density mismatch and the Debye length, the effective elastic

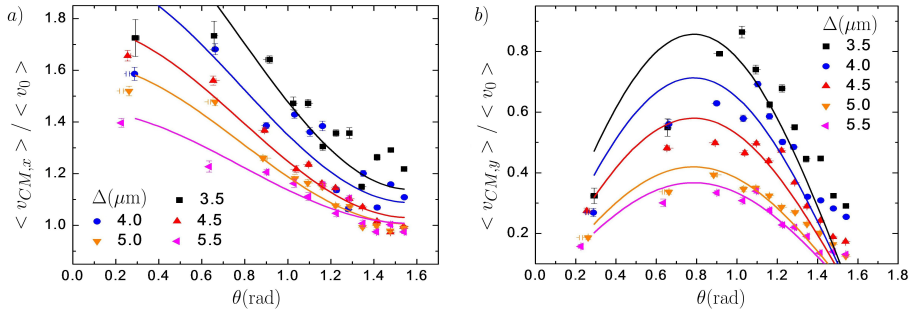

Figure 3.4: Comparison of the velocity (normalized by the self-propulsion velocity) between experiments (dots) and predictions of equation (3.5) (continuous line) as a function of the angle θ between the two particles measured for several distances Δ between them. **(a):** Component $v_{CM,x}$. **(b):** Component $v_{CM,y}$. Figure taken from [Martinez-Pedrero et al., 2018].

constant K we use to be low, thus $F_{g/h} \ll 1$, although its effect could still be relevant to the motion of particles. To test it, we tried several initial configurations, with the particles starting at an equilibrium height $h_0 = 1.33a$ with different separation and relative angle between them, for $F_{g/h} \sim 10^{-3}$. The results are resumed in figure 3.5. The first effect we wanted to test was whether gravity could enhance the alignment in the ribbon configuration between the pair. Indeed, particles tended to align forming an angle of 90° from initial angles different from that when there was enough separation between them. Particles can align this way from initial angles of 60° when the initial distance between them is $\Delta_0 = 3.33a$ (red curves), and the relative angle between them still moves towards 90° for lower initial angles, while they can reach 90° from an initial angle of 15° when the initial distance is $\Delta_0 = 5.33a$ (blue curves). However, for the initial distance $\Delta_0 = 2.67a$ (black curves), particles do not align towards 90°, but the trend is the opposite.

In panel (b) we measured the time evolution of the distance between the two particles. For the cases when $d_0 = 2.67a$, particles tend to separate slightly from each other. For greater initial gaps, particles tend to get closer to each other. We can clearly observe for the case of $d_0 = 5.33a$, the more they have to rotate to align, the more they approach each other, thus the alignment motion is associated to an effective attraction between the pair. Particles do not approach closer than $3.14a$ to each other, although in many cases their distance stabilizes for larger values, thus we cannot conclude there is an equilibrium distance between them. These effects appear despite no explicit finite size effects nor attraction or repulsion are present in the model.

We also studied the role of the intensity of the gravity $F_{g/h}$ in figure 3.5 (c). Gravity suppresses the relative periodic oscillatory motion between the pair of particles, as can be showed by the decrease on the amplitude of angular oscillations when increasing $F_{g/h}$. We observe that for the greatest value of $F_{g/h}$ the alignment is hindered, while already knowing that for a null gravity there is no alignment at all. Therefore, there must be an optimum value of gravity for

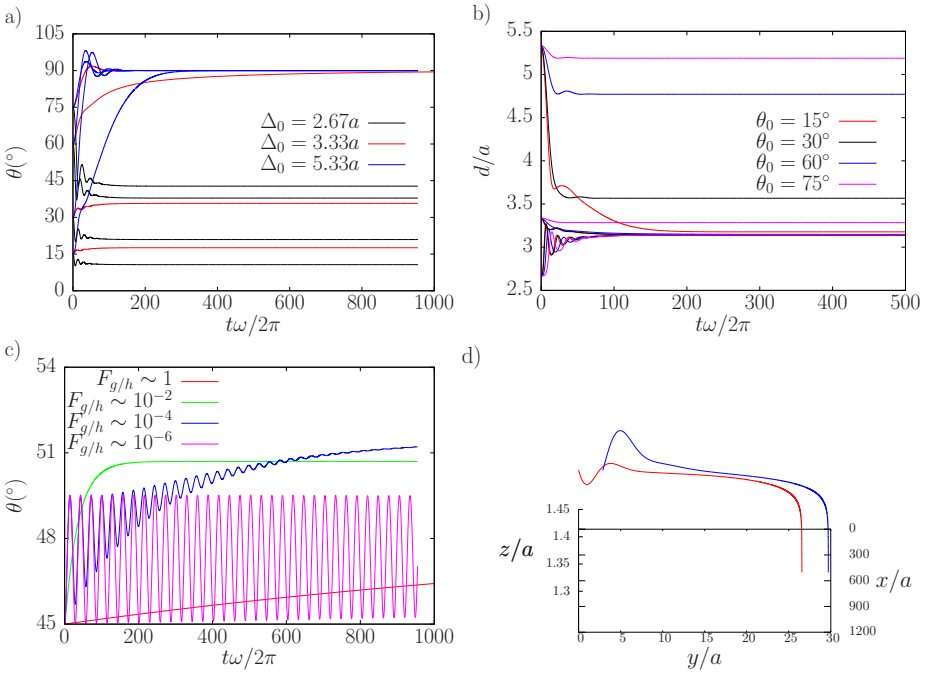

Figure 3.5: (a): Time evolution of the relative angle between the two particles for several initial distances and angles between them for $F_{g/h} \sim 10^{-3}$. **(b):** Time evolution of the relative distance between the two particles for several initial distances angles between them for $F_{g/h} \sim 10^{-3}$. **(c):** Time evolution of the relative angle between the two particles for several values of $F_{g/h}$, starting with the particles separated $\Delta_0 = 3.33a$ and forming an angle $\theta = 45^\circ$. **(d):** Trajectory of a pair of particles, with $F_{g/h} \sim 10^{-3}$, $\Delta_0 = 3.33a$. For all four panels $h_0 = 1.33a$.

which alignment is enhanced. Finally, in figure 3.5 (d) we showcase a trajectory for a pair of particles at $h_0 = 1.33a$, $\Delta_0 = 3.33a$ and an initial angle $\theta_0 = 60^\circ$. For particles so close to the wall, initially $v_{CM,y} \neq 0$; however, as particles align to form an angle of 90°, their translation is purely along the x-axis.

3.2.1 Flow created by a ribbon

Using our most simple analytical model (with no gravity, given by equation (3.5)), we can also compute the flow created by a ribbon as it displaces. Considering we have an array of N colloids aligned along the y-axis, at height h and distance Δ between them, the flux they create in their surroundings is given by:

$$
\begin{aligned}
u_x &= \sum_{i=0}^{N-1} a_i^3 \omega_i \left(\frac{z-h_i}{(x^2+(y-\Delta(\frac{N-1}{2}-i))^2+(z-h_i)^2)^{3/2}} + \right. \\
&\left. \frac{h_i-z}{(x^2+(y-\Delta(\frac{N-1}{2}-i))^2+(z+h_i)^2)^{3/2}} + \frac{6zx^2}{(x^2+(y-\Delta(\frac{N-1}{2}-i))^2+(z+h_i)^2)^{5/2}} \right) \\
u_y &= \sum_{i=0}^{N-1} a_i^3 \omega_i \frac{6zx\Delta(\frac{N-1}{2}-i)}{(x^2+(y-\Delta(\frac{N-1}{2}-i))^2+(z+h_i)^2)^{5/2}} \\
u_z &= \sum_{i=0}^{N-1} a_i^3 \omega_i \left(\frac{-x}{(x^2+(y-\Delta(\frac{N-1}{2}-i))^2+(z-h_i)^2)^{3/2}} + \right. \\
&\left. \frac{x}{(x^2+(y-\Delta(\frac{N-1}{2}-i))^2+(z+h_i)^2)^{3/2}} + \frac{6xz(z+h_i)}{(x^2+(y-\Delta(\frac{N-1}{2}-i))^2+(z+h_i)^2)^{5/2}} \right)
\end{aligned}
\tag{3.6}
$$

We represent the flow given by equation (3.6) for $N = 15$ particles in a stream map in figure 3.6 (a). The flow created by a ribbon is asymmetric when looked from the front or back side of the array. It tends to attract particles to the center of the structure when they are behind it, while it repels them to the sides when they are in front. The effect of this flow was tested experimentally in [Massana-Cid et al., 2017] by placing a non-magnetic colloid nearby a magnetic ribbon. The ribbon in this experiment was stabilized by introducing an additional magnetic field along the y direction besides the oscillating one in the XZ plane. In figure 3.6 (b) we can see the different behaviour whether the inert particle is in front or behind the ribbon; for the later case, it is attracted to the ribbon, while for the former it is repelled. To pass from one case to the other only the rotation sign of the oscillatory field had to be changed. In shorter ribbons, it is easier to observe the curvature of the flow, which leads to the ribbon not just repelling a colloid in front of it, but also pushing it to the side.

This section showcases the importance of solvent mediated interactions in colloidal dynamics. Another important aspect are the effects of symmetry breaks due to the presence of a close solid interface and/or gravity that lead to unexpected motion. In this particular subsection, this has led to two worth-publishing phenomena. The first one is the difference between front and behind respect to a moving ribbon, evidenced by the ability of the array to attract (repel) particles depending on whether they are behind (in front of) it. The second phenomenon is the reversibility breaking in the formation of a ribbon mediated by gravity. Even if being at Reynolds zero trajectories should be completely reversible, the effect of gravity aligning particles is not reversible, because it is a force whose sign cannot be reversed when making the particles move backwards.

3.3 Effect of the forces balance on arrays shape

So far, we have seen magnetic colloids under the effect of a circularly oscillating field being aligned in two possible ways. We have determined that the shape of these arrangements is dependent on the balance between magnetic, viscous and

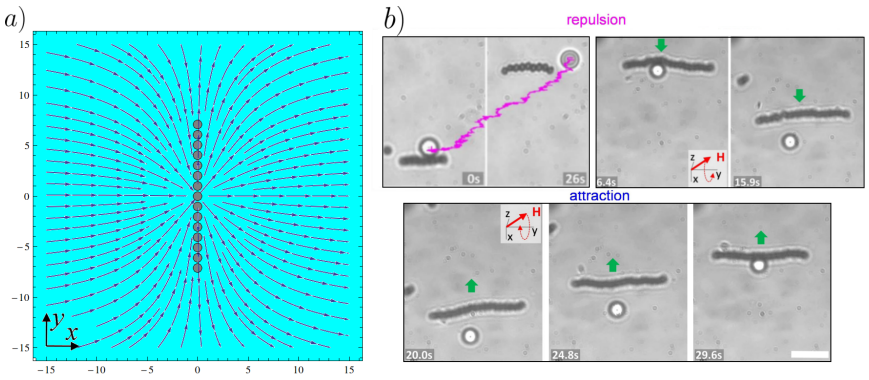

Figure 3.6: (a): Stream map of flow velocity created by a ribbon of $N = 15$ rotors with $\Delta = h$. **(b):** Snapshots of experimental systems consisting of a magnetic ribbon and a non-magnetic colloid. Top row depicts situations in which the ribbon repels the non-magnetic colloid, either by pushing it to the side (left) or forward (right). Bottom row depicts the ribbon attracting the non-magnetic colloid from its back side. Figures taken from [Massana-Cid et al., 2017].

gravitational forces acting on the colloids. We may add a third example to this list, reported as colloidal walkers in [Sing et al., 2010]. Walkers are based on the same mechanism that worms, as their particles remain united through the magnetic dipolar interaction between them and displace over a solid substrate. Unlike worms, they do not do so by "crawling" on the interface, but by a rotation of the whole array over it. This out of plane motion of particles in an array is favoured by the flow created by rotating particles and the non-null oscillating z component of the magnetic dipolar force. The velocity field around a rotating particle pushes up particles behind and sinks down particles in front. Even though the oscillating z component of the magnetic dipolar force is cancelled in a period, a period long enough combined with an intense interaction could lead to significant displacements in the vertical direction. These two effects have clearly different physical origins. We can measure its prevalence in the system through the Mason number, or its inverse $F_{m/h}$ we introduced in section 2.2.1 (equation (2.12)). On the other hand, gravity will obviously dampen vertical motion. We can measure its relative importance respect hydrodynamic forces through the other dimensionless parameter $F_{g/h}$ we introduced in equation (2.12). This presents a scenario in which there is a competition between three forces[3] that determines the shape of the colloidal arrangements that can be formed. In order to better understand the effect of the force competition present in the system on colloidal arrays, we have conducted a computational study in which we have subjected a test array to different conditions in which the balances between the involved forces in the system vary.

We have carried out LB simulations in which we have placed as our initial condition an array of N particles of radius $a = 3.7$ in a fluid of viscosity 0.1

[3]Considering that all body forces that act just on the height z are grouped under an "effective gravity" or "confining force".

rotating with constant angular velocity $\omega = 0.001$ at height $h = 5.5$. By varying the effective constant K and magnetic moment $\vec{m}$ of the colloid we can tune the dimensionless parameters $F_{g/h}$ and $F_{m/h}$. In the main set of simulations we ran, we took $N = 16$ aligned along the x direction in a system of size $240 \times 60 \times 120$. We also performed tests with 8 particles aligned the same way in a system of the same size and with 16 aligned along the y direction in a system of size $240 \times 240 \times 120$.

Starting from the configuration in which all particles are aligned in x at the same height, we have observed it can "deform" to give rise to four basic morphologies, depicted in figure 3.7. The basic configuration corresponds to the case in which the original arrangement remains in time as the whole array displaces, which we call *worm* (figure 3.7 (a)). A second possibility is that all particles remain aligned forming an unique structure which displaces by rotating over the substrate as a flexible rod, which we call *walker* (figure 3.7 (b)). The opposite situation is that particles remain at the original height, but the array does not remain in one piece, as it loses some of its particles; we have called this outcome *disaggregation* (figure 3.7 (c)). Finally, the original array can undergo more drastic changes, which do not limit to its fragmentation, but also to the bending of the remaining pieces over themselves and their subsequent rotation as a gear or *windmill*, as we have named this behaviour (figure 3.7 (d)).

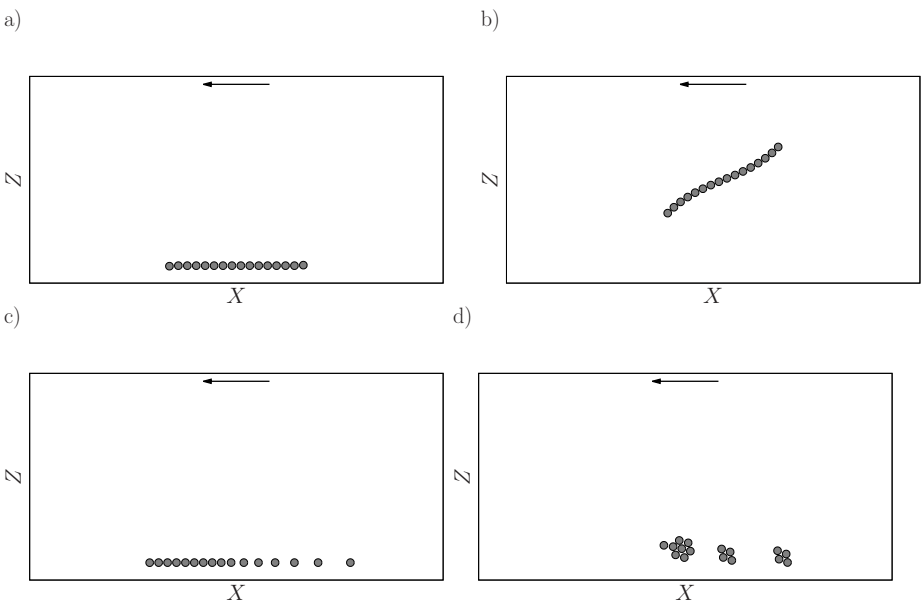

Figure 3.7: Schematic of the basic morphologies. **(a):** Walker. **(b):** Worm. **(c):** Disaggregation. **(d):** Windmill. Arrows indicate the direction of motion of the particles.

The worm morphology is observed for moderate values of the magnetic interaction and high values of gravity ($F_{g/h} > 10$); the greater the confinement, the stronger the magnetic forces can be before worms turn into walkers. For the same range of confinement values but low magnetic interaction ($F_{m/h} < 1$),

worms disaggregate. Walkers appear for high values of magnetic interaction ($F_{m/h} > 20$) for almost any value of gravity. We tested a very large value of $F_{g/h} \sim 1000$ to eventually find a curious phenomenon in which walkers try to form but instead the original worm structure is broken in pairs, which we have named *frustrated worm*. Finally, the behaviour described as windmill occurs for low values of both the magnetic interaction ($F_{m/h} \lesssim 1$) and the confinement ($F_{g/h} \lesssim 1$). Besides these four basic morphologies (plus the extra case of frustrated worms), there are some cases in which we observed an intermediate behaviour between two of the basic described behaviours. All of this information is summarized in figure 3.8.

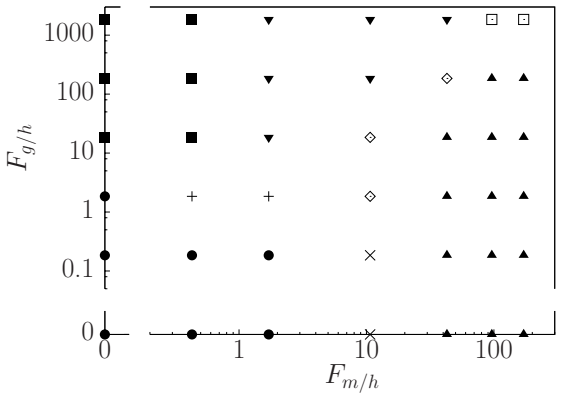

Figure 3.8: Confinement $F_{g/h}$ versus magnetic interaction $F_{m/h}$ diagram, with the observed morphologies. Different structures are: windmill (•), disaggregation (■), walker (▲), worm (▼), walker-worm mix (◇), worm-windmill mix (+), walker-windmill mix (×) and frustrated worm (□).

Besides predicting its formation, in [Sing et al., 2010] the length (given in number of particles) of walkers is also predicted based on the torque balance between the magnetic moment carried by the full array and the hydrodynamic torque of a rod with its shape and length. The expected length is the square root of the balance between magnetic and viscous forces, $N = \sqrt{F_{m/h}}$. We have tried to validate this prediction by measuring the length of the walkers we have observed when performing this computational study. Walkers are characterized by a continuous split and regrouping of particles, thus the size does not remain constant in time. We have measured its average length over a long period of time ($\sim$ 30 field periods); we represent its standard deviation as error bars in figure 3.9. Due to the periodically oscillating nature of the walker length, doing the average over more time will not reduce the dispersion in the displayed data. Overall, it is hard to tell from this figure whether the length of the walker adjusts to the theoretical prediction. We observe a slight trend of the length of the walker diminishing with the gravity, which is consistent with the shape of the walker region in the diagram we presented before (figure 3.8).

We repeated the same simulations for a system with 8 particles. The most significant difference is that morphologies resembling worms (either the pure

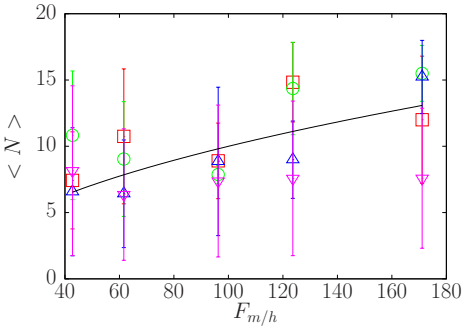

Figure 3.9: Average walker length $\langle N \rangle$ as function of magnetic interaction $F_{m/h}$ for several values of confinement $F_{g/h}$. [Sing et al., 2010] prediction appears as solid black line, with $F_{g/h} = 0$ as red squares ($\square$), $F_{g/h} \sim 10^{-1}$ as green circles ($\bigcirc$), $F_{g/h} \sim 1$ as blue triangles ($\triangle$) and $F_{g/h} \sim 10$ as pink triangles ($\triangledown$).

morphology or mixed ones) show up less often than for 16 particles, and require greater levels of confinement and magnetic interaction between particles. We can give a qualitative explanation to the observed differences. For low confinements, it is easier for small groups of particles to raise up, thus cases formerly qualified as mixed windmill-worm become simply windmills because of the lack of particles remaining in the equilibrium plane, so a greater confinement is required to keep particles in that plane. For high confinements, it is easy for particles that get lost as in disaggregation cases to never return to the worm due to the lack of particles pushing them from behind, so a greater dipolar interaction is required to keep the structure united. Therefore both effects are dependent on the number of particles in the system.

In order to test the stability of the ribbon phase, we also tested an initial configuration with 16 particles aligned along the y direction. This structure remained, admitting the loss of up to 3 particles, for the cases in which the dipolar interaction was null and $F_{g/h}$ between 10 and 1; for $F_{g/h} \sim 10^{-1}$ it split into two pieces of 8 particles each, while for greater and lower values of gravity we tested the structure eventually breaks up. When the dipolar interaction is present, particles tend to break the initial alignment and group into pairs aligned along x, as the magnetic interaction favours. For high values of this interaction pairs can later group and form longer walkers, as expected for that region of the diagram. Weaker magnetic interactions cannot group pairs of particles into longer structures, thus we cannot observe worms of length greater than 2 from this initial configuration.

3.4 Conclusions

In this chapter we have reviewed the formation of several arrays consisting of rotating magnetic colloids due to the effect of a circularly oscillatory magnetic field. In a first case, we have studied magnetic colloidal worms, which were

introduced in [Martinez-Pedrero et al., 2015]. We have introduced the hydrodynamic model which describes their movement. This has allowed us to show that the spacial symmetry breaking due to the presence of an interface leads to a net motion to an individual particle; the direction of the movement switches depending on whether the interface is with a solid or a fluid. This motion is enhanced when instead of an isolated particle there is an array of them, as the whole structure can displace faster, with a velocity that increases with the number of particles on it. We have tested this prediction with LB simulations. As already found with experimental comparison, this model is capable of qualitatively recovering the observed behaviour, a surprising feat for a theory based on a far-field approximation; the found discrepancies between theory and simulations are $\sim 10\%$, which speaks well of its worth.

This success encouraged us to use the same approach to describe systems of two particles whose relative positions can freely vary, but which are no subject to magnetic dipolar interactions, to study the possible formation of bound states [Martinez-Pedrero et al., 2018] capable of displacing aligned perpendicularly to their direction of displacement (a configuration which is not favoured by the magnetic dipolar interaction). This model has allowed us to describe the general motion of a pair of rotors whose angular velocity is parallel to the interface plane. They perform a composite motion consisting on a displacement of their centre of mass combined with a periodic oscillatory relative movement. There is a particular case when both particles are aligned along the direction perpendicular to their centre of mass motion for which they do not perform the relative oscillatory movement. Adding gravity to the system, the pair of particles can be pushed towards this particular configuration.

We have also studied the flow created by an array disposed perpendicularly to its direction of displacement, which we called a ribbon [Massana-Cid et al., 2017]. The flow created by this structure is anisotropic, being able to pull or push an inert particle depending on whether it is put behind or in front of it.

We also found reported a case which used an equivalent disposition of the magnetic field and an interface which led to the formation of arrays capable of displacing as rotating flexible rods, named walkers [Sing et al., 2010]. We attribute the great variety of shapes and motion mechanisms of systems formed of colloidal arrays to the underlying force competition between magnetic, viscous and gravitatory contributions. In order to clarify it, we conducted a systematic computational study exploring all possible ratios between them to find under which conditions each of these structures is stable. We found that worms are the preferred arrangement when gravity is strong and magnetic forces moderate; walkers when the magnetic forces dominate and for a wide range of gravities, preferably low ones, while ribbons remain stable for low magnetic interaction and moderate levels of gravity, which again suggests there is an optimal value of gravity which favours its existence. We also identified alternative shapes in which an array can be deformed under other regimes.

Chapter 4

Self-assembly of arrays

Had I been consulted on Creation, I could have provided some useful hints.

Alfonso X, *the Wise*

This chapter is closely related to the results presented in section 3.3. There, we studied under which conditions, characterized by the balances of forces acting on colloids, arrays were a stable structure and which shape they took. The fact that, starting from an initial array located parallel to a plane, an unidimensional structure could rearrange itself, moving in additional dimensions, to form new structures is just a minor example of a more interesting phenomenon we will focus on this chapter: self-assembly. Self-assembly is a very important phenomenon at many scales, from the formation of galaxies to atoms or life. At the nanoscale, it is behind several chemical engineering processes, in which it is not only important to control the composition of products, but their morphology. In our case, some of the structures we analysed in the previous chapter were already presented independently as cases of self-assembly [Sing et al., 2010, Martinez-Pedrero et al., 2015], which greatly simplifies its attainment and in turn makes them more appealing.

In this chapter we will study the self-assembly of these structures in initially disordered colloidal suspensions. Our goal is to provide a common framework that allows us to identify all the ensembles that can appear, and under which conditions, in a system that despite possessing a very concrete geometry (see figure 2.2) has led to the observation of different kind of arrays. For such an ambitious task, we will rely on a systematic computational study, evaluating the same scenarios (in terms of balances of forces) than in section 3.3, but now with a bigger system, employing our LB code. This method allows us to actually track the full process of self-organization, in contrast to other works which despite claiming they are studying self-assembly then are limited to studying the free energy of several configurations and praying the system will naturally evolve to the lowest energy one without getting trapped in any metastable state.

The structure of this chapter is pretty similar to a journal article, with a more concrete methodology description after this introduction, followed by the results exposition, its discussion and a section for conclusions.

4.1 Methodology

In order to study the self-assembly of arrays of magnetic colloids, we have conducted a computational study employing our LB code. We simulated systems consisting of 500 particles of radius $a = 2.3$, initially randomly distributed over a plane at height $h_0 = 5.5$, in a system filled with a fluid of viscosity $\eta = 0.1$ of size $480 \times 480 \times 240$, giving an initial planar density of 3.6%, which ensures the system is very dilute and it will be possible to observe the array structures we are interested in describing and not larger aggregates. We worked with ferromagnetic particles. We applied a circularly oscillatory magnetic field $\vec{B} = B_0(\cos\Omega t, 0, \sin\Omega t)$ with $B_0 = 0.61158$ and $\Omega = 0.001$. In order to vary the dipolar interaction between them we varied the modulus of their magnetic moment, between $m_0 = 1$, with an associated $\Omega_C = 0.02$ and $m_0 = 20$, with $\Omega_C = 0.4$ (thus ensuring $\Omega < \Omega_C$ in all cases); to simulate the cases with null magnetic dipolar interaction, we turned off and worked with $m_0 = 1$. We also added a confinement in height to the system modelled through an elastic potential $K(h - h_0)^2/2$ affecting all particles, whose values ranged between $K = 0$

and $K = 0.1$. Simulations ran for 1500000 LB time steps for $m_0 = 10, 15, 20$, for 3000000 for $m_0 = 0$ and for 4500000 for $m_0 = 1, 2, 5$, taking measurements every 1000 steps. All quantities in this paragraph are given in LB units.

The dimensionless parameters we have been typically using, $F_{m/h}$ and $F_{g/h}$, will range between 0.43 and 170 for $F_{m/h}$ and between 0.02 and 200 for $F_{g/h}$, plus the cases in which they are 0. The choice of values is the same we did in section 3.3[1], which will later allow us to do a one on one comparison with the results obtained there.

4.2 Analysis tools

Working with a single array of a few colloids it is easy to observe at first sight which arrangement they follow. However, for systems with a large number of particles this approach is not practical. Instead, we opt for a more quantitative approach over the qualitative one we presented in section 3.3.

First statistical measurement we can make is computing the mean aggregate size $\langle n \rangle$, using a distance criterion thoroughly explained in appendix C. Plotting its time evolution, we can know the growth dynamics of aggregates, and determine if they form at all in the first place, and then whether they reach a stable size or its growth could be indefinite, or at least too slow to cover in reasonable simulation times.

The study of aggregate size distributions $p(n)$ gives us a more detailed information than the mean size $\langle n \rangle$, which is just its first momentum. In those cases in which $\langle n \rangle$ has reached low values, it allows us to tell whether there is a coexistence of large aggregates with a significant population of particles not belonging to any cluster or no big aggregates appear. Something similar applies once $\langle n \rangle$ has reached high values; we can ensure that there are large aggregates in the system, but not if their mean size is enough to characterize their size or there could be more inhomogeneous distributions.

Besides characterizing aggregates size, we are very interested in their shape. We expect to observe the formation of three basic structures: worms, ribbons and walkers. A reminder with the basic geometries of these configurations is given in figure 4.1. We have made up two statistical identifiers to be able to tell apart these three basic cases. The procedure to compute both of them is pretty similar. We look for pairs of particles in the system that are near each other[2]. For each pair we compute the velocity of their center of masses as $\vec{v}_{CM} \equiv \frac{\vec{v}_2 - \vec{v}_1}{2}$, and the vector that unites them as $\vec{r} \equiv \vec{x}_2 - \vec{x}_1$. We can use these two vectors to compute our identifiers:

[1] With the exception of the largest confinement we tried there.
[2] Using the same distance criterion we used to identify aggregates.

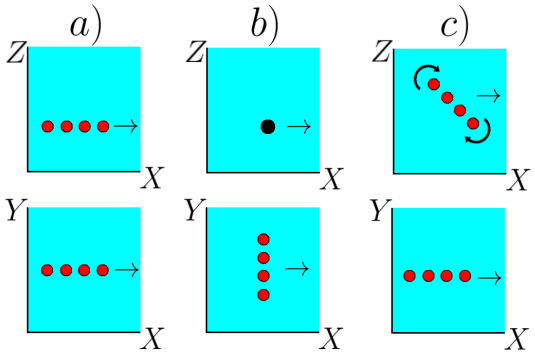

Figure 4.1: Scheme with the basic geometry of colloidal arrangements. **(a):** Worm. **(b):** Ribbon (black circle in the ZX projection represents all particles are superposed). Column **(c):** Walker.

$$\Theta^{3D} = \frac{1}{N_{pairs}} \sum_{pairs} \left(\frac{\vec{v}_{CM} \cdot \vec{r}}{v_{CM} r} \right)^2$$
$$\Theta^{2D} = \frac{1}{N_{pairs}} \sum_{pairs} \left(\frac{\vec{v}^{xy}_{CM} \cdot \vec{r}^{xy}}{v^{xy}_{CM} r^{xy}} \right)^2 \tag{4.1}$$

where N_{pairs} is the number of pairs accounted and the superindex ^{xy} indicates we only take the components (x, y) of those vectors.

Both Θ^{3D} and Θ^{2D} lie between 0 and 1. The parameter Θ^{2D} allows us to identify whether a pair is aligned along its displacement direction in the XY plane, which happens for worms and walkers, which have $\Theta^{2D} = 1$, but not for ribbons, which have $\Theta^{2D} = 0$. Extending it to three dimensions, we can discriminate worms from walkers, since the later perform an out of plane motion in which particles are not aligned along their velocity, thus only worms have $\Theta^{3D} = 1$. A static walker that only rotates keeping its center of masses at a constant position would have $\Theta^{3D} = 0$; however, since our colloids displace, they will have a non-zero Θ^{3D} value. Qualitatively, we can say the faster the walker rotates or the longer it is, the closer to 0 Θ^{3D} will be. Therefore, we can distinguish these three basic structures with these two quantities.

In section 3.3, windmills were also introduced. Windmills are formed when an array rolls over itself due to the flux created by its particles. They were easy to observe in that section because the initial condition of the system already was an array. Now, windmills would appear in a two-step process, in which particles should self-assemble in arrays in the first place, and then the arrays should roll over themselves. Windmills would have a value of $\Theta^{2D} \approx 1$, but due to its irregular shape, we cannot predict a priori its value of Θ^{3D}. Knowing their formation process, we can look the region of weak (but non-zero) dipolar interactions for cases with Θ^{2D} close to 1 and intermediate values of Θ^{3D} and then check whether windmills are formed there.

4.3 Results

We present the statistical identifiers we introduced in the previous section in figures 4.2, 4.3, 4.4 and 4.5. In each of those figures results are separated in different panels with data series corresponding to cases with the same value of $F_{m/h}$, varying $F_{g/h}$ in each of them. In figures displaying temporal evolutions, we applied a smoothing filtering to the data, plotting the average over 10 data points (10000 LB time steps) instead of the instantaneous value at each time step, to eliminate the noise and better visualize the results. Let us analyse them in more detail.

4.3.1 Mean aggregate size $\langle n \rangle$

We start by showcasing the time evolution of the mean aggregate size $\langle n \rangle(t)$ (figure 4.2). For $F_{m/h} = 0$ (figure 4.2 (a)), we see that aggregates do not reach large sizes. When $F_{g/h} \sim 1$ (pink and blue curves), they stabilize at sizes which are roughly above 2. For more extreme values of confinement (either stronger or lighter), $\langle n \rangle$ lies well below 2, which would suggest no structures appear. For $F_{m/h} = 0.43$ (figure 4.2 (b)), we have to differentiate the case with $F_{g/h} = 1.85$ (pink curve) from the rest: that case displays an almost flat curve at $\langle n \rangle = 1$. For the remaining values of $F_{g/h}$, there is an indefinite growth, which we could guess from the case $F_{g/h} = 0$ (red curve), which is the fastest growing one from the pack, could saturate at $\langle n \rangle \approx 3$.

For $F_{m/h} = 1.71$ and $F_{m/h} = 10.69$ (figure 4.2 (c) and (d)), we let the simulations run the longest, yet we cannot foresee in most cases the aggregates reaching a stationary size; however, their mean size never reaches double figures. We do not observe any peculiar dependency of $\langle n \rangle$ with $F_{g/h}$ in these two series of data, although for $F_{m/h} = 10.69$ (figure 4.2 (d)), the two curves with higher values of $F_{g/h}$ (grey and orange ones) are the ones which grow slower.

This particular trend is accentuated in the remaining three cases (figures 4.2 (e), (f) and (g)), corresponding to the highest values of $F_{m/h}$ we tried. In all three of them, the curve for $F_{g/h} = 185$ (grey curve) stabilizes to the lowest value of $\langle n \rangle$. On the other hand, the longest arrays appear for $F_{g/h} = 0.18$ (blue curve) in all three panels as well, with $F_{g/h} = 0.018$ (green curve) coming second in two of them, and not being an apparent order on how the three remaining curves are ordered. Grouping these three panels, we can say that in general, $\langle n \rangle$ increases with $F_{m/h}$, stabilizing at $\langle n \rangle = 5.5$ for $F_{m/h} = 42.8$ and $\langle n \rangle = 12$ for $F_{m/h} = 171.1$ when $F_{g/h} = 0.18$ (blue curves in figures 4.2 e) and g) respectively), and $\langle n \rangle = 2$ for $F_{m/h} = 42.8$ and $\langle n \rangle = 4$ for $F_{m/h} = 171.1$ when $F_{g/h} = 185$ (grey curves in figures 4.2 e) and g) respectively). It is also noteworthy that for some cases with high values of both dipolar interaction and confinement, $\langle n \rangle(t)$ is very oscillating, even after filtering the data. These oscillations are periodic with the field.

Summarizing, the general trend is that dipolar interaction eases the formation of larger aggregates. Highly magnetically interacting systems also reach steady mean aggregate sizes faster than lowly interacting ones. Confinement

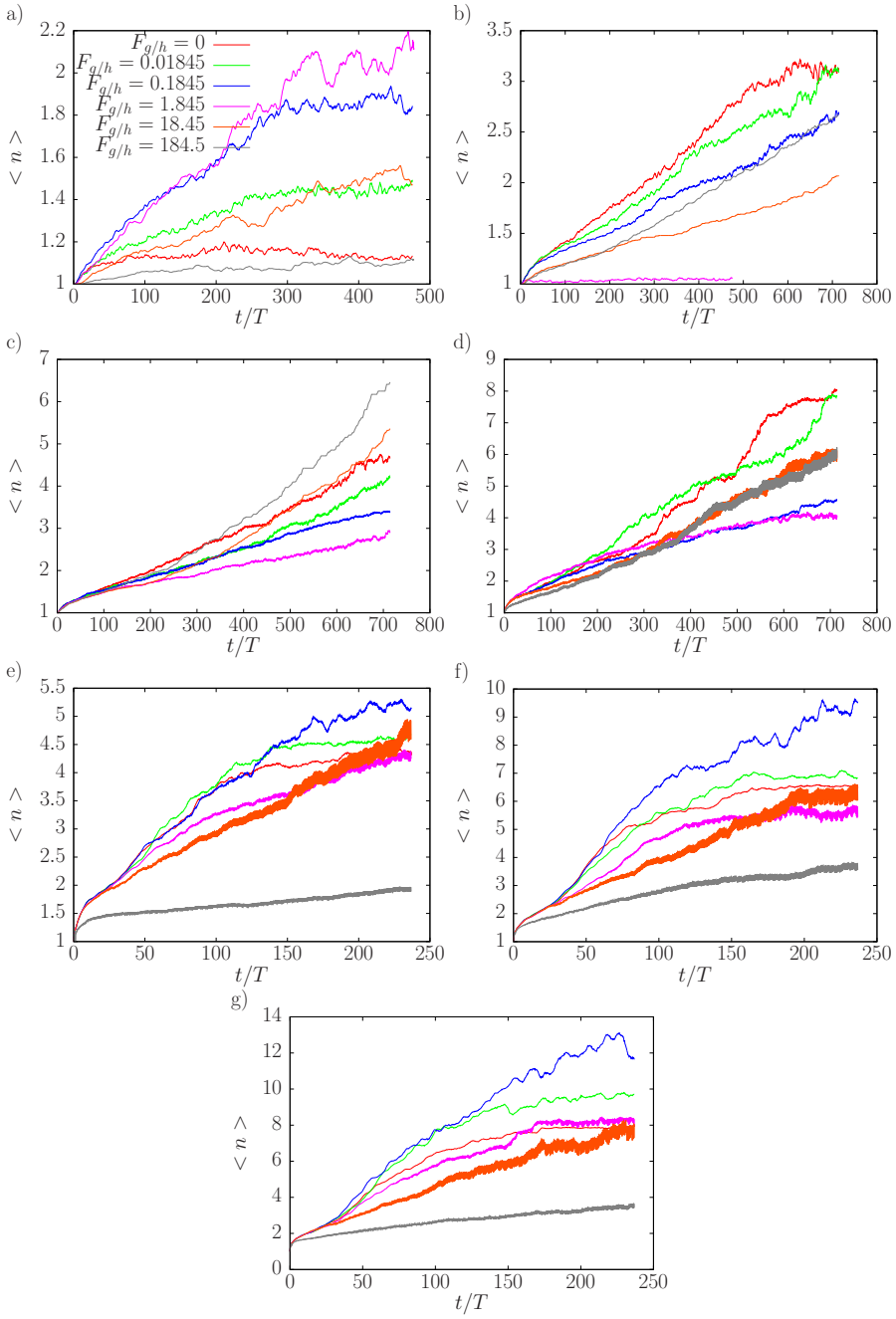

Figure 4.2: Time evolution of $\langle n \rangle$ for **(a):** $F_{m/h} = 0$. **(b):** $F_{m/h} = 0.43$. **(c):** $F_{m/h} = 1.71$. **(d):** $F_{m/h} = 10.69$. **(e):** $F_{m/h} = 42.8$. **(f):** $F_{m/h} = 96.2$. **(g):** $F_{m/h} = 171.1$. Time is normalized in all cases with the period of the applied magnetic field.

does not follow such a direct trend regarding aggregate size. When $F_{m/h} = 0$, there is an optimal range of values of $F_{g/h} \sim 1$ which allow the formation of aggregates, albeit small. On the other hand, for high values of $F_{m/h}$, confinement tends to hinder the formation of larger aggregates. However, for $F_{m/h} = 1.71$ it is quite the opposite, and the cases with higher values of $F_{g/h}$ are the ones with greater values of $\langle n \rangle$ associated.

4.3.2 Aggregate size distributions $p(n)$

We computed our size distributions once the system has reached a steady value of $\langle n \rangle$ or, when not possible, we limited it to the last 500000 LB time steps (roughly 80 field periods); we have only observed for one case (with $F_{m/h} = 1.71$ and $F_{g/h} = 185$, grey curve in figure 4.2 (c)) $\langle n \rangle$ growing past 1 in that time lapse, with the usual growth being well under the unity. We also limited the range of size distributions by ending them with $p(n \geq n_{cutoff})$. This approach is done in order to avoid plotting the noise associated to lack of statistics for large aggregates, which should not appear on a regular basis. The choice of this cut-off is completely arbitrary and depends on the information we are more interested in showcasing for each distribution, although we took the same for every curve in a same panel in figure 4.3 to prevent confusion.

For $F_{m/h} = 0$, $\langle n \rangle$ never reached values past 3. In figure 4.3 (a) we can see that effectively isolated particles are the most common in those systems. However, we should distinguish again the cases with $F_{g/h} = 1.85$ and 0.185 (pink and blue curves) from the rest, since the probability of finding a particle belonging to a structure with $n \geq 5$ is non-negligible, and the percentage of monomers, which reaches values around 80% for the most extreme values of $F_{g/h}$ (either in the lowest side (red curve) and the highest one we tried (grey curve)) are below 40% in both cases. As we get farther from these "optimal" values of $F_{g/h}$, the probability of particles aggregating to form any structure falls.

For $F_{m/h} = 0.43$ (figure 4.3 (b)), the case with $F_{g/h} = 1.85$ (pink curve) is completely different to the rest: we cannot say there is self-assembly of any structure, and if two particles ever get close enough to each other to be counted as belonging to a same aggregate it can be probably attributed to a casual event. Excluding this case, we can still distinguish two separate regimes for more confined particles (orange and grey curves), for which the maximum of $p(n)$ is located at 2 and fall to 0 for $n \geq 5$, and weakly confined particles (red, green and blue curves), whose maxima are located respectively at 5, 3 and 2 and present a significant amount of aggregates of size $n \geq 5$ and even $n \geq 10$ for $F_{g/h} = 0$ (red curve).

The cases with $F_{m/h} = 1.71$ and $F_{m/h} = 10.69$ (figure 4.3 (c) and (d)) correspond to those in which $\langle n \rangle$ did not reach steady values (or took longer to do it). In general, the obtained distributions look pretty noisy, with very serrated profiles and no apparent preferred sizes; except for $F_{g/h} = 0.185$ and $F_{g/h} = 1.85$ with $F_{m/h} = 1.71$ (blue and pink curves in figure 4.3 (c)) at $n \approx 3$, $p(n)$ never goes above 0.2; these two particular curves also fall to 0 before reaching $n = 10$, while for the remaining cases in these two panels there is a significant presence

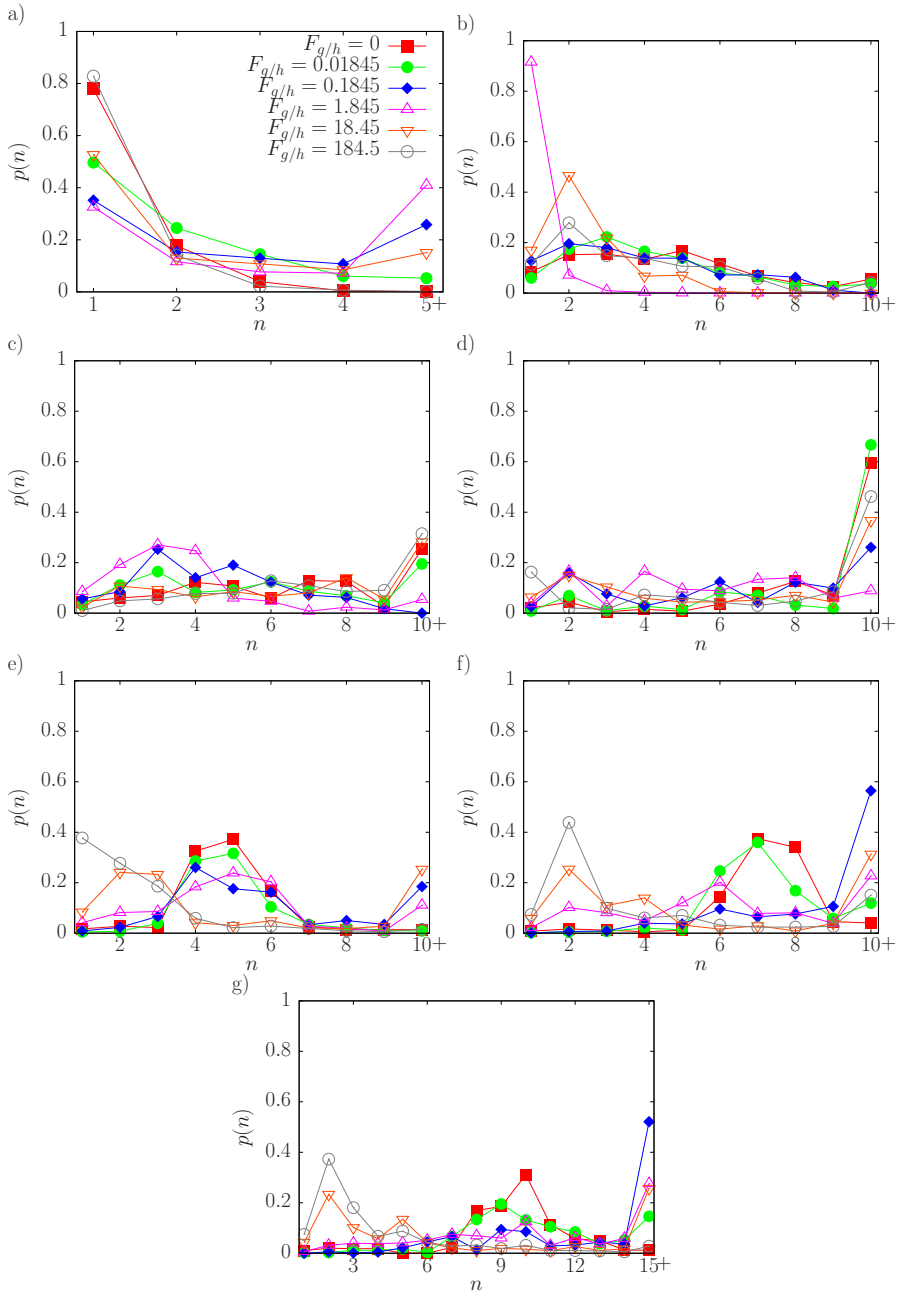

Figure 4.3: Cluster size distribution $p(n)$ for or **(a):** $F_{m/h} = 0$. **(b):** $F_{m/h} = 0.43$. **(c):** $F_{m/h} = 1.71$. **(d):** $F_{m/h} = 10.69$. **(e):** $F_{m/h} = 42.8$. **(f):** $F_{m/h} = 96.2$. **(g):** $F_{m/h} = 171.1$. The last point in each series represents the probability of a particle belonging to a cluster of size $n \geq N+$, with $N = 5$ in panel (a), $N = 15$ in panel (g) and $N = 10$ in the rest.

of aggregates of size $n \geq 10$.

For $F_{m/h} = 42.8$ (figure 4.3 (e)) we find more homogeneous size distributions. For $F_{g/h} = 185$ (grey curve), the most common structure are isolated particles, and $p(n)$ decays almost linearly from $p(1) \approx 0.4$ to $p(4) \approx 0$. For $F_{g/h} = 18.5$ (orange curve), aggregates are typically of 2 or 3 particles, although there are also aggregates of size $n \geq 10$. For $F_{g/h} = 1.85$ and $F_{g/h} = 0.185$ (pink and blue curves), the most common aggregate size range between 4 and 6, again with some presence of aggregates of size $n \geq 10$. For $F_{g/h} = 0.0185$ and $F_{g/h} = 0$ (green and red curves), distributions are very sharp, with its maximum at $n = 5$ and barely no particles belonging to aggregates with sizes $n > 6$ or $n < 4$.

The two cases with more highly interacting particles (figure 4.3 (f) and (g)) are pretty similar to each other, and they can be commented together. We already saw that most confined systems reached smaller values of $\langle n \rangle$, and effectively, for $F_{g/h} = 185$ and $F_{g/h} = 18.5$ (grey and orange curves), $p(n)$ has its maximum at $n = 2$, with $p(2) \approx 0.4$ for $F_{g/h} = 185$ (grey curves) and $p(2) \approx 0.25$ for $F_{g/h} = 18.5$. Size distribution for $F_{g/h} = 185$ (grey curves) decays to 0 before our cut-off is reached, while for $F_{g/h} = 18.5$ (orange curves) there are still aggregates of greater size. For $F_{g/h} = 1.85$ and $F_{g/h} = 0.185$ (pink and blue curves), distributions are pretty flat[3] and extend to large values of n, therefore getting noisy; the presence of particles not belonging to any aggregate in these cases is rare. For weakly confined particles (red and green curves), distributions are again sharp, although not as much as for $F_{m/h} = 42.8$. The maximum of $p(n)$ for these four cases is shifted towards greater values of n as the confinement decreases and the dipolar interaction increases, lying between 7 and 10.

4.3.3 Shape quantifiers Θ^{2D} and Θ^{3D}

The quantity Θ^{2D} tells us whether the arrays, in case they are formed, align in the direction of displacement of particles or perpendicular to it, allowing us to distinguish ribbons from other structures.

For particles without magnetic interaction between them ($F_{m/h} = 0$, figure 4.4 (a)), we already saw that it is very hard to self-assembly big particle arrangements. Only for $F_{g/h} = 1.85$ and $F_{g/h} = 0.185$ (pink and blue curves) we observed a significant presence of structures containing 5 or more particles. For these cases, Θ^{2D} reaches low values around 0.25, which could be indicative of the presence of ribbons, although they could either not be the only present structure in the system or not be perfectly shaped. We must note there is a slight drift towards increasing values of Θ^{2D}, indicative that the percentage of ribbons diminishes with time as alternative structures are formed in the system.

The rest of cases in which we observed the formation of aggregates have an associated value of Θ^{2D} close to 1. The system usually reaches that value almost instantaneously, which means that the first formed structures are already

[3]Do not get fooled by the apparent peak at the end, $p(n \geq 10)$ or $p(n \geq 15)$ covers a wide range of values.

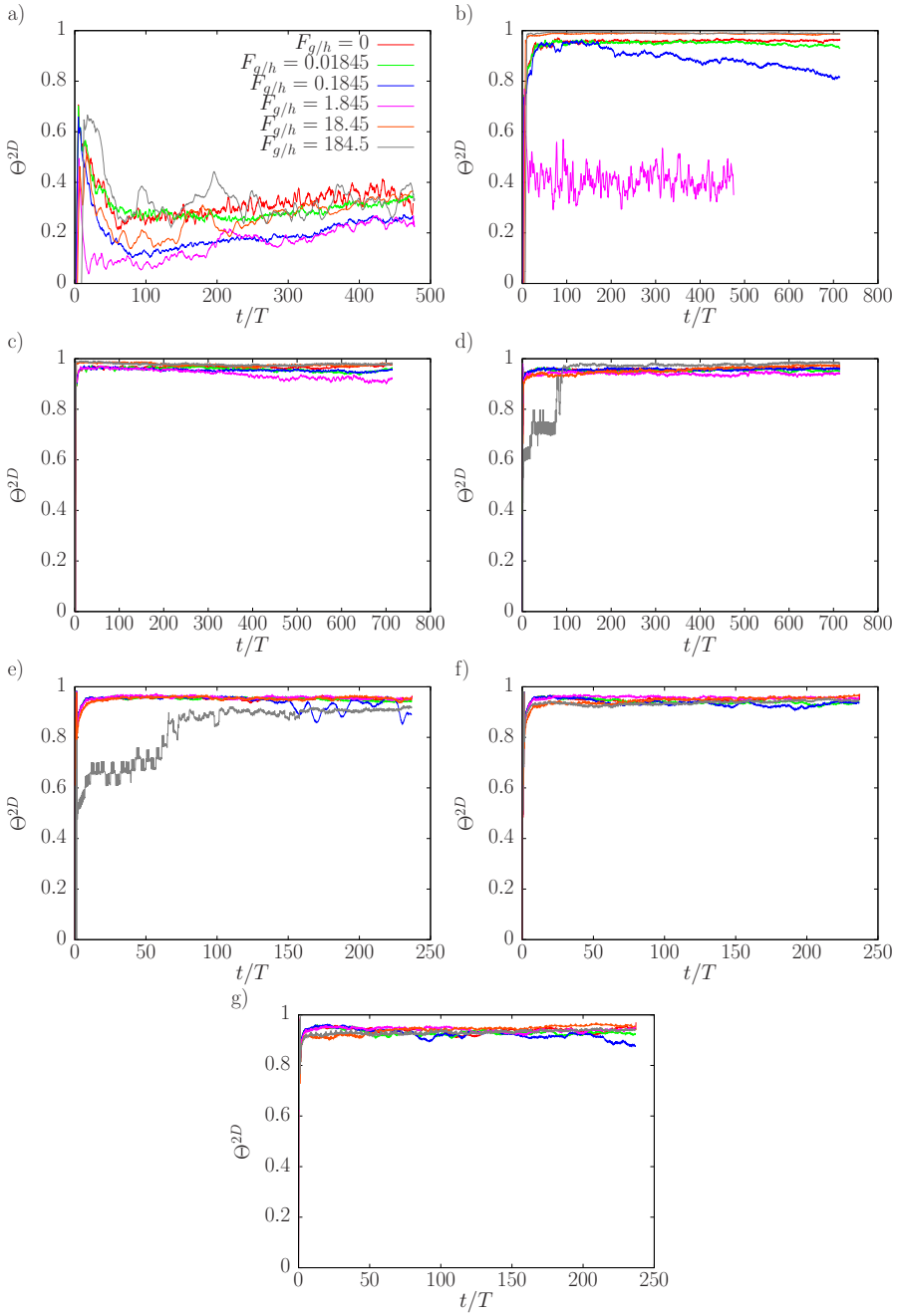

Figure 4.4: Time evolution of Θ^{2D} for **(a):** $F_{m/h} = 0$. **(b):** $F_{m/h} = 0.43$. **(c):** $F_{m/h} = 1.71$. **(d):** $F_{m/h} = 10.69$. **(e):** $F_{m/h} = 42.8$. **(f):** $F_{m/h} = 96.2$. **(g):** $F_{m/h} = 171.1$. Time is normalized in all cases with the period of the applied magnetic field.

aligned, and it tends to remain quite stable in time, thus arrays only grow but do not change its shape. The only cases that deviate from this trend are associated to $F_{g/h} = 185$ with $F_{m/h} = 10.69$ and $F_{m/h} = 42.8$ (grey curves in figures 4.4 d) and e)), which take longer to grow towards 1, and some cases with $F_{g/h} = 0.185$ (blue curves) for several values of $F_{m/h}$ for which there is a slight decay of Θ^{2D}.

Those cases in which we had not observed the formation of aggregates have noisy $\Theta^{2D}(t)$ curves with a value around 0.4, which means that in those rare events in which aggregates are casually formed, they are not aligned neither parallel or perpendicular to the privileged directions of the system.

We defined the parameter Θ^{3D} to identify whether the arrays with an associated value of $\Theta^{2D} \approx 1$ are walkers or worms. Therefore we can discard from this analysis those cases in which Θ^{2D} is small, although we also show them. They have associated values of Θ^{3D} far from 1 as well.

For $F_{m/h} = 0.43$ (figure 4.5 (b)), Θ^{3D} quickly reaches a stationary value close to 1 for the two greatest values of $F_{g/h}$ (grey and orange curves). For the low confinement cases (red, green and blue curves), Θ^{3D} takes longer to reach its steady value (around 200 field periods), which lies around 0.7 for $F_{g/h} = 0$ and $F_{g/h} = 0.0185$ (red and green curves), and slightly lower for $F_{g/h} = 0.185$ (blue curve). By the end of the simulation run (around 600 periods), there is a slight drift of Θ^{3D} towards lower values, which we cannot associate to any sudden change of the arrays size; for $F_{g/h} = 0$ it actually stops growing at that point. Therefore, it must be associated to a rearrangement of particles in the arrays.

For $F_{m/h} = 1.71$ and $F_{m/h} = 10.69$ (figures 4.5 c) and d)), $F_{g/h} = 185$ (grey curves) reaches values of Θ^{3D} above 0.9, indicative that worms are the most frequent structure in the system. The cases with $F_{g/h} = 18.5$ (orange curves) have a behaviour differentiated from those with lower values of confinement, reaching for $F_{m/h} = 1.71$ a value of 0.86, and 0.7 for $F_{m/h} = 10.69$, which do not seem to have reached steady values but to keep growing slowly with time. For lower confinements (red, green, blue and pink curves), all curves tend to stabilize at similar values of Θ^{3D}, around 0.6 for $F_{m/h} = 1.71$, and around 0.5 for $F_{m/h} = 10.69$. For these cases, we should check later by looking at the particle positions if effectively windmills appear.

Greater values of dipolar interaction (figures 4.5 e), f) and g)) show a clear dependence of Θ^{3D} with confinement, with Θ^{3D} being an almost monotonously growing function of $F_{g/h}$. With the exception of $F_{g/h} = 185$ for $F_{m/h} = 42.8$ (grey curve in figure 4.5 (e)), all of these cases stabilize at values of Θ^{3D} below 0.5, which indicates the dominant presence of walkers. The dependence of Θ^{3D} with confinement is consistent with the intuitive belief we could have that it hinders the rotation of walkers. As happened for $\langle n \rangle$, the cases with high values of both dipolar interaction and confinement display periodic oscillations.

The analysis of Θ^{3D} has allowed us to clearly identify those cases in which worms are the only dominant structure. Its dependence with $F_{g/h}$ for high val-

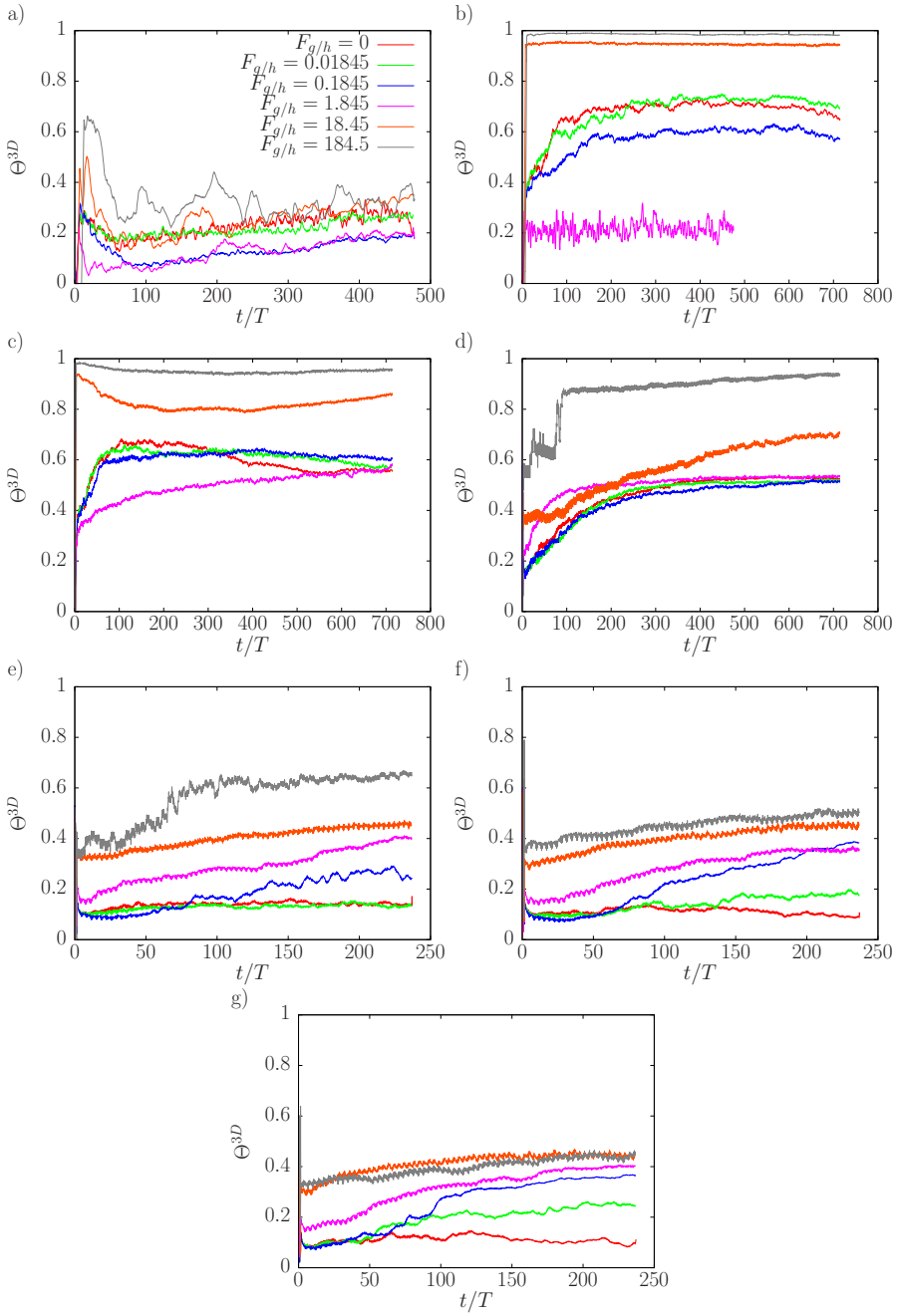

Figure 4.5: Time evolution of Θ^{3D} for **(a):** $F_{m/h} = 0$. **(b):** $F_{m/h} = 0.43$. **(c):** $F_{m/h} = 1.71$. **(d):** $F_{m/h} = 10.69$. **(e):** $F_{m/h} = 42.8$. **(f):** $F_{m/h} = 96.2$. **(g):** $F_{m/h} = 171.1$. Time is normalized in all cases with the period of the applied magnetic field.

ues of $F_{m/h}$ hints us the presence of walkers in the system. However, there are some dubious cases: on the one hand, those blurry cases in which the aggregates could take intermediate shapes between the well-defined geometries we presented, and on the other hand, windmills to which we did not assign an ideal value of Θ^{3D}.

4.3.4 Summary and discussion

We summarize the results showcased in figures 4.2, 4.4 and 4.5 in color diagrams in figure 4.6. This allows us to locate the regions of parameters at which there are similar behaviours. In all three diagrams, we can see a region composed by the points with $F_{m/h} = 0$ axis and the one with $F_{m/h} = 0.43$ and $F_{g/h} = 1.85$ with differentiated colours at which there is no self-assembly of arrays. We must subtract from this area a region represented by the points $F_{g/h} = 0.185$ and $F_{g/h} = 1.85$ with $F_{m/h} = 0$ at which the self-assembly of ribbons occurs. The area at which worms form appears clearly delimited when looking at the Θ^{3D} diagram (figure 4.6 (c)): when $F_{g/h} = 185$, for $F_{m/h}$ between 0.43 and 10.69, while for $F_{g/h} = 18.5$ just until $F_{m/h} = 1.71$. We can associate walkers to the lowest values of Θ^{3D} and largest values of $\langle n \rangle$, which delimit a clear region for $F_{g/h} \leq 1.85$ and $F_{m/h} \geq 42.8$.

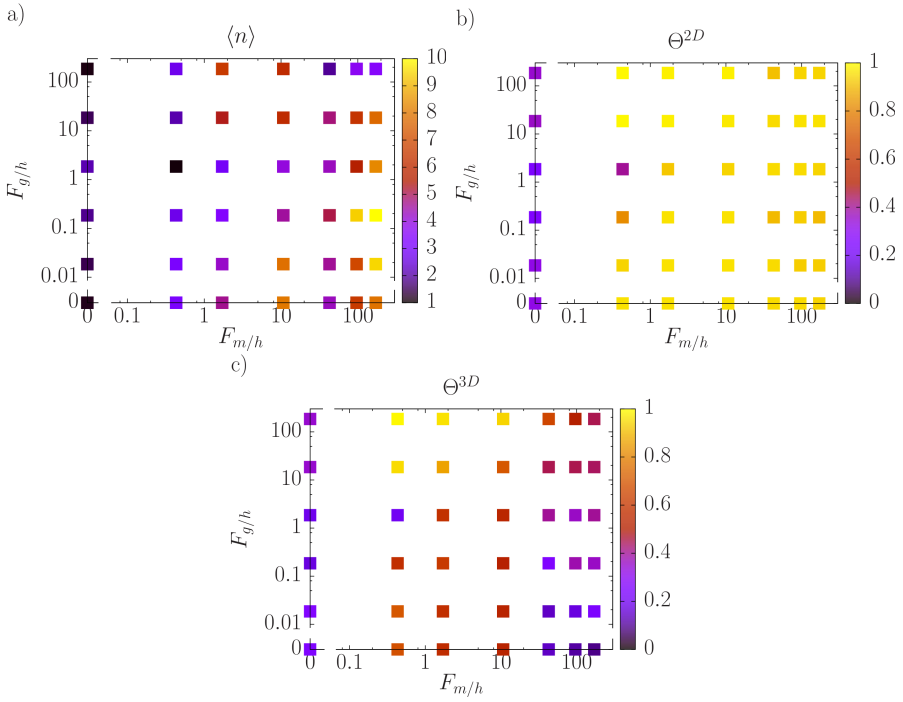

Figure 4.6: Diagram with the final value reached by statistical identifiers: **(a)** $\langle n \rangle$, **(b)** Θ^{2D}, **(c)** Θ^{3D}.

To complete the discussion, we present snapshots of the system at the final

state for some cases. The direct visualization of particle positions allows us to confirm we have been able to correctly identify the arrays formed in the system, observe the structures formed in those cases that were not clear and get some more insight of the particular dynamics of the system to better identify the mechanisms of self-assembly. In figure 4.7, we show those cases in which our statistical identifiers easily allowed us to identify the shape of the arrays self-assembled in the system. In panel 4.7 (a) we showcase the "outliner" case with $F_{m/h} = 0.43$ and $F_{g/h} = 1.85$. Just anecdotally, even if statistical parameters say these are the worse conditions from among those we tested to observe the self-assembly of any array, we can still observe two arrays of 4 and 5 particles aligned along y, although slightly tilted. For the same value of $F_{g/h}$ and $F_{m/h} = 0$ (figure 4.7 (b)), the formation of ribbons is favoured. However, ribbons can interact with each other and end up bending or forming more extensive structures which do not conserve their aligned disposition; this explains the drift we found for Θ^{2D}. On the other hand, worms (displayed in 4.7 (c)) present a very anisotropic interaction between each other; they can grow by trapping smaller worms with which they share the same y coordinate, which explain why their size grows indefinitely with time, but then repel other worms with different y coordinates. Worms have a plastic structure and can even bend in their motion to separate from other worms; these deformations then remain for long periods of time. We found walkers (displayed in figure 4.7 (d)) have associated very sharp size distributions. Even if they can grow with a mechanism similar to worms, they are not confined to two dimensions, but can move relatively freely in all three dimensions, thus making it harder for two of them to meet and fuse. Longer walkers tend to separate further from the interface, while individual particles remain at the initial height. Eventually, it is possible to see a large walker rotating over a smaller one or an isolated particle without interacting with it. As confinement increases, this ability to get further from the wall diminishes, and walkers can grow longer, therefore broadening size distributions functions.

In section 3.3, we discussed the dependence of the walker's length with $F_{m/h}$ (figure 3.9). New measurements made in this chapter allow us to check again whether we can recover Katz's prediction [Sing et al., 2010]. In figure 4.8 we display the results, by measuring both the mean $\langle n \rangle$ and mode of the size distributions $p(n)$. Our simulated points follow the growing dependency with $F_{m/h}$ we would expect, although systematically lie below the theoretical prediction. Moreover, those cases with greater confinement (blue points) reach greater sizes than those with no gravity (red points). This is indicative that the mechanism that stops the growth of walkers in our simulations is not them reaching its maximum size, but height scattering.

As for intermediate or dubious cases, we display four of them in figure 4.9. In panel (a), we display a case for low values of both dipolar interaction and confinement. We can see a diverse mixture of structures similar to windmills, small worms and aggregates with no array shape, in a case in which there is a clear competition between hydrodynamic interactions, which shape arrays as ribbons, and magnetic interactions, which aligns them perpendicularly, and the interplay between a low magnetic interaction and hydrodynamic interactions once particles are aligned along their direction of displacement, which tends to

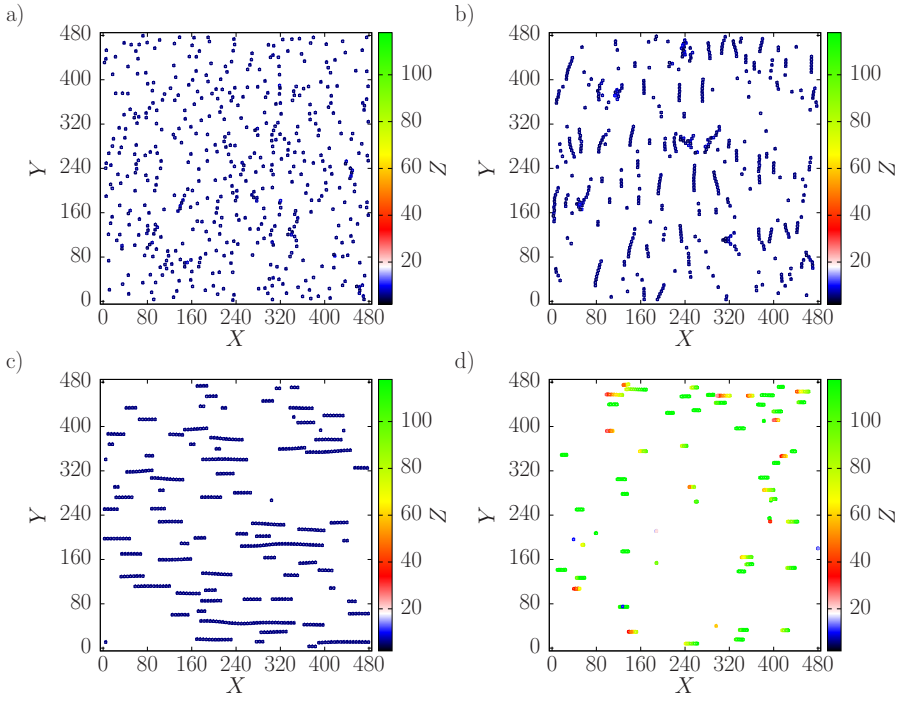

Figure 4.7: Snapshots displaying colloid positions for: **(a):** No arrays formed ($F_{m/h} = 0.43$ and $F_{g/h} = 1.85$). **(b):** Ribbons ($F_{m/h} = 0$ and $F_{g/h} = 1.85$). **(c):** Worms ($F_{m/h} = 1.71$ and $F_{g/h} = 185$). **(d):** Walkers ($F_{m/h} = 171$ and $F_{g/h} = 0$). Snapshots are taken at the last time step of each simulation run. Height is displayed with the colour scale (legend on the right).

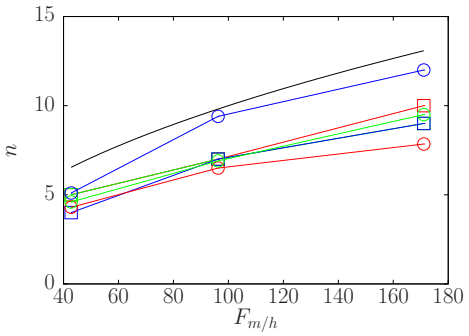

Figure 4.8: Walker length n as function of $F_{m/h}$ for $F_{g/h} = 0$ (in red), $F_{g/h} \sim 10^{-2}$ (green) and $F_{g/h} \sim 10^{-1}$ (blue). Results obtained as the mode of $p(n)$ are displayed as squares (□), while those obtained as the mean size $\langle n \rangle$ are displayed as circles (◯). Some points might be overlapped by other data series with identical values and not correctly displayed. Reference [Sing et al., 2010] prediction displayed as black solid line.

roll the array to end up forming a windmill. Next, we study what happens for high confined cases as we increase the dipolar interaction. In 4.9 (b) we go to a first level, in which the dipolar interaction is strong enough to appreciate the attractive and repulsive part of the cycle, evidenced by worms breaking and joining again as they displace; this leads to broad size distributions and explains the oscillations we saw in $\langle n \rangle(t)$. If we increase it even more, as in 4.9 (c), we can even observe the vertical motion induced by dipolar interaction partially breaking the confinement in z, so when worms split in pairs, a particle of the pair gets over the other. This leads not only to broad size distributions, but to oscillating curves for Θ^{3D}; there is an evident contrast between long worms in the plane and couples of particles over each other. Therefore, the displayed values of $\langle n \rangle$ and Θ^{3D} are not representative of the system, but the time average of the two states between which it alternates. We can also analyze the worm/walker crossover at lower values of both confinement and dipolar interaction in figure 4.9 (d). In this scenario we observe worms with some particles from its tail being able to elevate and form three-dimensional rotating structures.

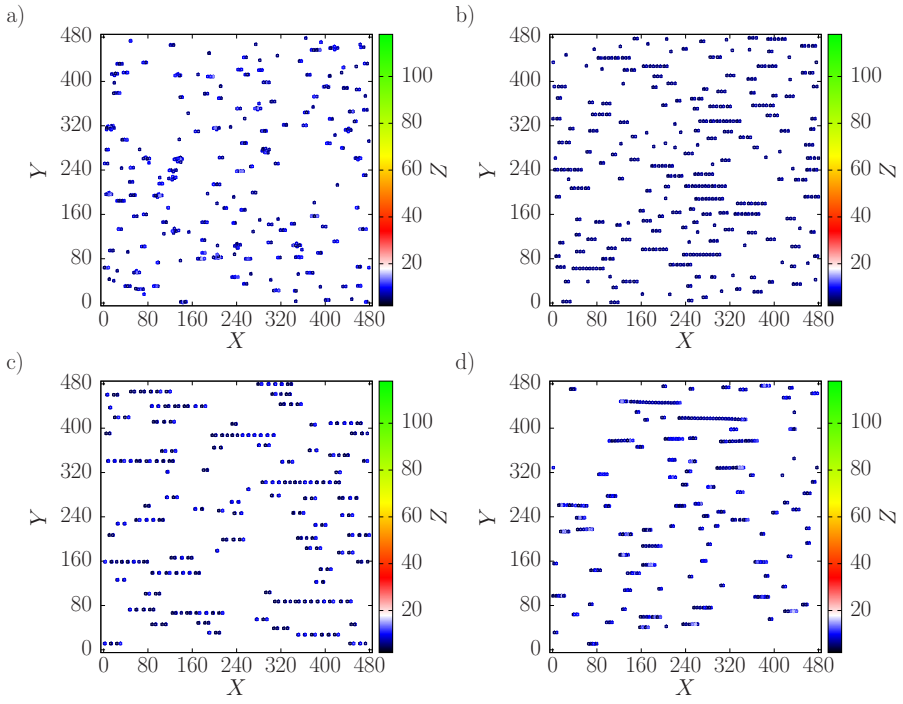

Figure 4.9: Snapshots displaying colloid positions for: **(a):** $F_{m/h} = 0.43$ and $F_{g/h} = 0.185$. **(b):** $F_{m/h} = 42.8$ and $F_{g/h} = 185$. **(c):** $F_{m/h} = 171$ and $F_{g/h} = 185$. **(d):** $F_{m/h} = 10.69$ and $F_{g/h} = 1.85$. Snapshots are taken at the last time step of each simulation run. Height is displayed with the colour scale (legend on the right).

4.4 Conclusions

With this computational study, we have been able to determine the conditions under which arrays of magnetic colloids can self-assemble. We have grouped them under a diagram (figure 4.10), which we can compare to figure 3.8 from the previous chapter. Both the walker and worm zones are located in the same area of the diagram, which proves the robustness of these structures, since we can not only shape them by controlling the force balances acting on magnetic colloids, but also assemble them from a disordered state. Worms can grow indefinitely, as long as they can keep absorving particles from its head, while they repel from their sides. On the other hand, the growth of walkers saturates to a finite size. We have found that the lack of confinement leads to a new mechanism to stop its growth before reaching the maximum size predicted in reference [Sing et al., 2010]: longer walkers can move further from the interface than smaller ones and isolated particles, thus preventing the growth of the walker by adding smaller aggregates to its structure.

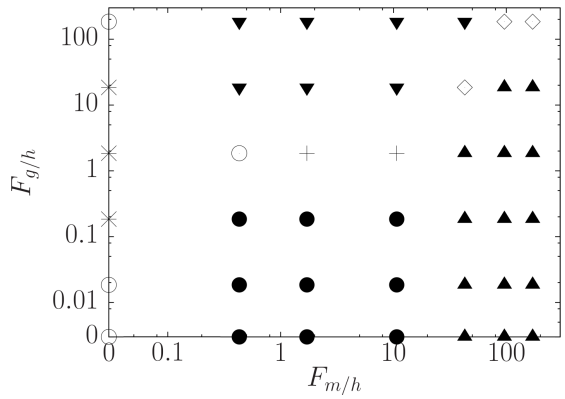

Figure 4.10: Confinement $F_{g/h}$ versus magnetic interaction $F_{m/h}$ diagram, with the observed morphologies. Different structures are: windmill (•), walker (▲), worm (▼), walker-worm mix (◇), worm-windmill mix (+), walker-windmill mix (×) and ribbons (∗). Cases in which no structure is self-assembled are displayed with circles (◯).

Once we move to regions where hydrodynamic interactions are dominant, the differences arise. Even if windmills can also self-assemble for weak values of confinement and magnetic interaction, the later cannot be null in order to form the precursor arrays which end up rolling to form this particular structure. It would have been interesting to reduce more gradually dipolar interaction to check if there is a threshold value of it at which particles pass from tending to align parallel to their motion to doing it perpendicularly.[4]

Finally, for null dipolar interaction, hydrodynamic interactions become dom-

[4]As a reminder, in [Martinez-Pedrero et al., 2018] dipolar interaction was not null and two-particle ribbons were more common than windmills, although particle shape could have played an important role at hindering its formation too.

inant, and we would have expected the formation of ribbons. However, the self-assemble of any structure under these conditions is harder, and the resulting ones are fragile and can easily be broken due to the distorting flux created by particles that may approach them. As we already saw in section 3.2, gravity has an important role in the formation of ribbons, and we found that those values for which it could help their formation display the longest arrays. Ribbons grow from precursor structures formed by a pair of particles aligned perpendicularly to their moving direction. They may incorporate new particles, which due to the rotating flux they create, will initially interact with the initial array by jumping over it. High values of gravity annul this growing mechanism, while for low values the particle can either get expelled up and not come back to the array plane or break it by pulling out one of the two particles forming the initial array.

Chapter 5

Anisotropically interacting squirmers

Li Wenzi always thinks three times before he acts. Twice is enough.

Confucius

Research on colloidal science has sprouted during this century. One of the most exciting applications is the design of colloidal crystals, in which colloidal particles act as atoms. Isotropic interactions between colloids ease the formation of these structures. However, we can also find cases in which anisotropy plays an important role in the system. Magnetic colloids, which we showcased in previous chapters, are a prime example of this, through the anisotropic dipolar interaction between them. It is possible to engineer other colloids which interact anisotropically with each other. Janus colloids, which are characterized by having two faces with different properties, are the most obvious example of this. These non-trivial interactions between colloids may also favour the formation of colloidal super structures with several shapes. In [Hong et al., 2008] we can find an experimental example of Janus particles with an hydrophobic attractive half and an hydrophilic charged repulsive one, and a catalogue of the structures into which they can self-assemble. Experimental results were supported by MC simulations.

Colloids in [Hong et al., 2008] were not self-propelled. In order to describe suspensions of self-propelled particles, there are plenty of both experimental [Cisneros et al., 2007, Palacci et al., 2013, Schwarz-Linek et al., 2012, Petroff et al., 2015, Theurkauff et al., 2012, Thutupalli et al., 2011] and simulation works [Ishikawa and Pedley, 2007, Ishikawa et al., 2008, Ishikawa and Pedley, 2008, Evans et al., 2011, Delmotte et al., 2015, Molina et al., 2013, Oyama et al., 2016, Oyama et al., 2017, Alarcón and Pagonabarraga, 2013, Zöttl and Stark, 2014, Blaschke et al., 2016, Matas-Navarro et al., 2014], just to mention a few in which they are described with the squirmer model. In most of these cases they interact with each other isotropically, or anisotropy is introduced elsewhere, like in particle shape [Theers et al., 2016, Kyoya et al., 2015].

In this chapter we aim at describing a system whose particles combine both the anisotropic interaction of Janus particles with the self-propelled character of active particles, with the explicit solvent effects. In order to describe the coupling between self-propulsion and hydrodynamic effects, we model our particles as squirmers (see section 1.2.7), which can provide a valid description if we prioritize far-field effects and do not look into the finer detail close to their surface. We will focus on quasi two-dimensional systems, in the sense that particles are confined to a plane but the fluid can move in the third dimension, following an approach similar to the one in [Alarcón et al., 2017].

This chapter is structured as follows: after this introduction, we explain the model used to describe our swimmers and the simulation scheme we use. Then, we define some of the numerical parameters we will analyse in the results section. Finally, we summarize the results and present the conclusions.

5.1 Model specifications

We model self-propelled spherical Janus colloids as squirmers [Lighthill, 1951, Blake, 1971, J. Pedley, 2016] interacting via an anisotropic pair potential dependent on the relative orientation and distance between particles. The competition between attractive and self-propelling forces is quantified through a dimension-

less parameter:

$$\xi = \frac{F_d}{F_{att}} \tag{5.1}$$

where $F_d = 6\pi\eta a v_s$ is the typical Stokes friction force for a sphere of radius a moving at velocity v_s, which for a squirmer will be given by equation (1.27), and F_{att} is the absolute value of the attractive force at the minimum of the potential. In the following subsections we will introduce the attractive potentials we have used and how we implemented it all into LB.

5.1.1 Anisotropic interactions

We have generalized the isotropic potential used on [Alarcón et al., 2017] to study isotropic attractive squirmers to make it anisotropic. To do so, we introduce a pair potential which depends on the distance r_{ij} between two squirmers and their attractive patches orientations $\hat{p}_i$ and $\hat{p}_j$, $V(r_{ij}, \hat{p}_i, \hat{p}_j)$, namely:

$$V(r_{ij}, \hat{p}_i, \hat{p}_j) = V_{rep}(r_{ij}) + V_{att}(r_{ij})\phi(\theta_i, \theta_j) \tag{5.2}$$

This potential is composed by a short range repulsive part $V_{rep}(\vec{r}_{ij})$ and an attractive term $V_{att}(\vec{r}_{ij})$, which in turn is weighted by a function $\phi(\theta_i, \theta_j)$ to give it its anisotropic behaviour.

The repulsive term $V_{rep}\,(r_{ij})$ is introduced to avoid particle overlap in LB simulations. It is valid only at very short distances. Specifically, we include a soft-sphere interaction [P. Allen and J. Tildesley, 1989] given by:

$$V_{rep}(r_s) = \begin{cases} \epsilon_s \left[\left(\frac{\sigma_s}{r_s}\right)^{\nu} - \left(\frac{\sigma_s}{h_0}\right)^{\nu} \left(1 - \frac{(r_s - h_0)^{\nu}}{h_0}\right) \right] & 0 < r_s \leq h_0 \\ 0 & \text{otherwise} \end{cases} \tag{5.3}$$

where the separation is defined as $r_s \equiv r_{ij} - \sigma$, with σ being the diameter of the particle; in order to avoid overlap, $r_s > 0$. The other parameters are $\nu = 2$, the energy scale $\epsilon_s = 1.5$, the characteristic gap between two particles $\sigma_s = 0.5$, and the cut-off of the potential h_0, whose value is tuned to ensure the potential vanishes smoothly there. Its value depends on the minimum of the attractive potential, although given the short range of this repulsive contribution, $h_0 < \sigma$.

The anisotropic attractive contribution is weighted by an orientational dependent function, $\phi(\hat{r}_{ij}, \hat{p}_i, \hat{p}_j) = \phi(\theta_i, \theta_j)$, where $\hat{r}_{ij} = \vec{r}_{ij}/r_{ij}$ is the unit vector joining the centres of mass of the squirmers, θ_i is the angle defined between the patch unit vector $\vec{p_i}$ and the inter-particle vector $\vec{r}_{ji} = \vec{r}_j - \vec{r}_i$; similarly θ_j is the angle between the patch unit vector $\vec{p_j}$ and the inter-particle vector $\vec{r}_{ij} = -\vec{r}_{ji}$. The geometry of the interacting pair is illustrated in figure 5.1, which shows a pair of Janus squirmers for two types of anisotropic interactions.

We consider two different types of attractive potentials, depending on the

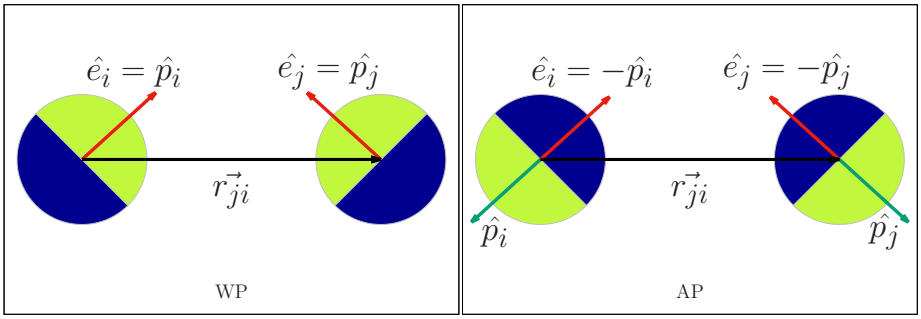

Figure 5.1: Sketch of the interaction between two Janus Swimmers, attractive patch is in green, while repulsive patch is in blue. The direction of the swimming is represented by a red vector $\vec{e}$, the green vectors represents the direction of the attractive patch $\vec{p}$ and the black vector is the center-center distance between two swimmers $\vec{r_{ij}}$. In the left panel, the patch direction coincides with the swimming direction, thus we call them Janus simmers with the patch (WP), while in the right panel, the patch direction is pointing against the swimming direction, such Janus swimmers are called against the patch (AP).

potential range. For a larger cut-off radius, $r_{cutoff} = 2.5\sigma$, we take

$$V_{att}(r_{ij}) = \begin{cases} 4\epsilon\left[\left(\frac{\sigma}{r_{ij}}\right)^{12} - \left(\frac{\sigma}{r_{ij}}\right)^{6}\right] & (2^{1/6}\sigma) < r_{ij} < r_{cutoff} = 2.5\sigma \\ -\epsilon & r_{ij} < (2^{1/6}\sigma) \\ 0 & \text{otherwise} \end{cases} \tag{5.4}$$

while for a shorter-range potential, $r_{cutoff} = r_c = 1.5\sigma$, we take the classic LJ-potential as in equation (5.4), adding a smooth transition function that brings potential to zero at r_c.

$$V_{att}(r_{ij}) = 4\epsilon\left[\left(\frac{\sigma}{r_{ij}}\right)^{12} - \left(\frac{\sigma}{r_{ij}}\right)^{6}\right] + 4\epsilon\left[6\left(\frac{\sigma}{r_c}\right)^{12} - 3\left(\frac{\sigma}{r_c}\right)^{6}\right]\left(\frac{r_{ij}}{r_c}\right)^{2} - 4\epsilon\left[7\left(\frac{\sigma}{r_c}\right)^{12} + 4\left(\frac{\sigma}{r_c}\right)^{6}\right] \tag{5.5}$$

for $(2.2033^{1/6}\sigma) < r_{ij} < r_c$, $V_{att} = -0.30492\epsilon$ for $r_{ij} < (2.2033^{1/6}\sigma)$ and $V_{att} = 0$ otherwise. Both V_{att} and dV_{att}/dr vanish continuously as r_{ij} approaches r_c [Stoddard and Ford, 1973], avoiding a jump in the force at the cutoff distance. Figure 5.2 compares the total potential using the short range potential given by equation (5.5) (red curves) and the classical LJ potential (equation (5.4)) and cut-off distance of 2.5σ (blue curves).

The anisotropic interaction is controlled by the angular potential:

$$\phi(\theta_i, \theta_j) = \begin{cases} \cos(\theta_i)\cos(\theta_j) & \text{if } (\hat{p}_i \cdot \hat{r}_{ij}) > 0 \text{ and } (\hat{p}_j \cdot \hat{r}_{ij}) > 0 \\ 0 & \text{otherwise} \end{cases} \tag{5.6}$$

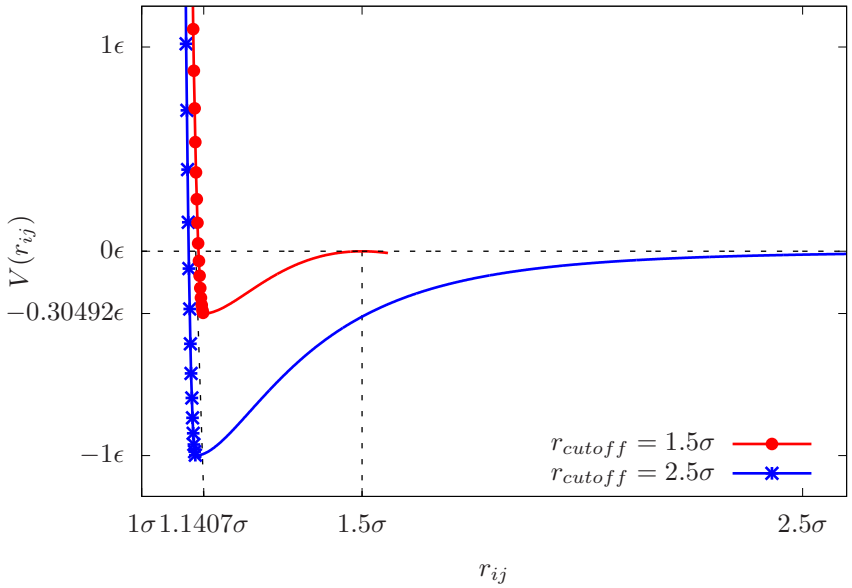

Figure 5.2: Graphic representation of the total potential $V(r_{ij})$ with $\phi = 1$, using the Lennard-Jones potential with a smooth transition function given in (5.5) as the attractive part of $V(r_{ij})$ (red curve), the repulsive soft sphere potential at short separation distance with $h_0 = (2.2033^{1/6} - 1)\sigma$ (red crosses) is using with this cut-off potential. The blue curve is using (5.4), with the repulsive soft sphere potential at short separation distance with $h_0 = (2^{1/6} - 1)\sigma$ (blue circles).

inspired by [Hong et al., 2008], where such orientation-dependent interaction was applied to model amphiphilic colloidal spheres with an hydrophobic hemisphere and the other one charged. This anisotropic potential ensures a non-vanishing torque when $(\hat{p}_i \cdot \hat{\mu}_{ji}) > 0$ and $(\hat{p}_j \cdot \hat{\mu}_{ij}) > 0$.

5.1.2 Simulation details

We will study the self-assembly of suspensions of Janus swimmers computationally. The method we will employ is LB (see section 1.3.1, 1.3.2 and 1.3.3). The squirmer model is introduced by modifying the boundary condition on the colloids surface (equation 1.37) to include the tangential surface slip velocity created by squirmers (equation 1.26 with $A_n = 0\ \forall n$ and $B_n = 0$ when $n > 2$). Accounting for all forces acting on each squirmer allows us to to update dynamically. The torque exerted by the fluid determines how the squirmer direction of self-propulsion will rotate.

We simulate $N = 888$ spheres of diameter $\sigma = 4.6$ (corresponding to lateral box sizes of $L \approx 83\sigma$) and prepare a dilute squirmer suspension at $\phi = 0.10$ (where $\phi = \frac{\pi}{4}\rho\sigma^2$ and $\rho = N/L^2$) with periodic boundary conditions in a quasi 2D system with a thickness larger than the particle diameter ($k = 5$) ($L \times L \times k\sigma$), in order to be able to capture three dimensional hydrodynamics effects. Given that a squirmer travels its own size in $\tau = \frac{\sigma}{v_s}$, we have performed simulations from 1450 up to 3000 τ. Once the system reaches steady state, in a time window

between 1000 and 2000 τ, we carry out a systematic analysis of the dynamics of the squirmer suspension, considering ξ from 0.1 to 10 and β from -3 up to 3.

For cases with $\xi = 1$ we simulate instead 3552 spheres while keeping ϕ constant by adapting the system size.

5.2 Analysis Tools

We quantify particle aggregation studying the emergent structures in suspensions of Janus swimmers in the absence of any external force. We measure the degree of aggregation analyzing the cluster size distribution based on a distance criterion. Specifically, two particles belong to the same cluster whenever their distance is smaller than $r_{cl} = 1.75\sigma$, corresponding to the the minimum of the $g(r)$ (see appendix C for details). To calculate the cluster-size distribution $f(s)$ we apply a criterion based on [Valeriani et al., 2012]: (i) We arbitrarily subdivide the range of s-values into intervals $\Delta s_i = (s_{i,max} - s_{i,min})$, where we define the total number of clusters within each interval Δs as n_i^t; (ii) we assign the value $n_i = n_i^t/\Delta s_i$ to every s within Δs_i, and compute the fraction of clusters of size s as $f(s) = n_i/N_c$, where $N_c = \sum_i n_i \Delta s_i$ is the total number of clusters.

We analyze both the properties of the cluster size distribution themselves as a function of the degree of activity, β and its competition with the Janus interaction, ξ. We also analyze global quantities associated to the cluster geometry, such as the cluster radius of gyration

$$R_g(s) = \sqrt{\sum_{i,j=1}^{s} \frac{\left(\vec{r}_i - \vec{r}_j\right)^2}{2s}}\,, \tag{5.7}$$

(dividing by 2 to avoid double counting), as well as the average degree of ordering quantifies by the polar order

$$P(s) = \left| \frac{\sum_{i=1}^{s} \hat{e}_i}{s} \right|\,, \tag{5.8}$$

Moreover, the tensor order parameter is

$$Q_{hk}(t) = \frac{1}{N} \sum_{i=1}^{N} \left(2 e_{ih}(t) e_{ik}(t) - \delta_{hk}\right)\,; \tag{5.9}$$

for a two-dimensional system [Stariolo and Barci, 2010], where h and k are x, y and N the total amount of squirmers. The nematic order parameter $\lambda(t)$ correspond to the largest eigenvalue of Q_{hk} [Eppenga and Frenkel, 1984]. All quantities have been computed when the system reaches a steady state.

5.3 Results

5.3.1 Observed morphologies

From a purely qualitative analysis of the observed morphologies, we can classify them into seven different types: coarsening, finite size rounded clusters, chains,

gas with polar order, gas with nematic order and disordered gas. The emerging structures are very sensitive to the patch direction, *i.e.* whether the patch is pointing toward (WP from here onwards), or against (AP from here onwards), the squirmer propulsion direction. A sample snapshot of the former six morphologies is shown in figure 5.3.

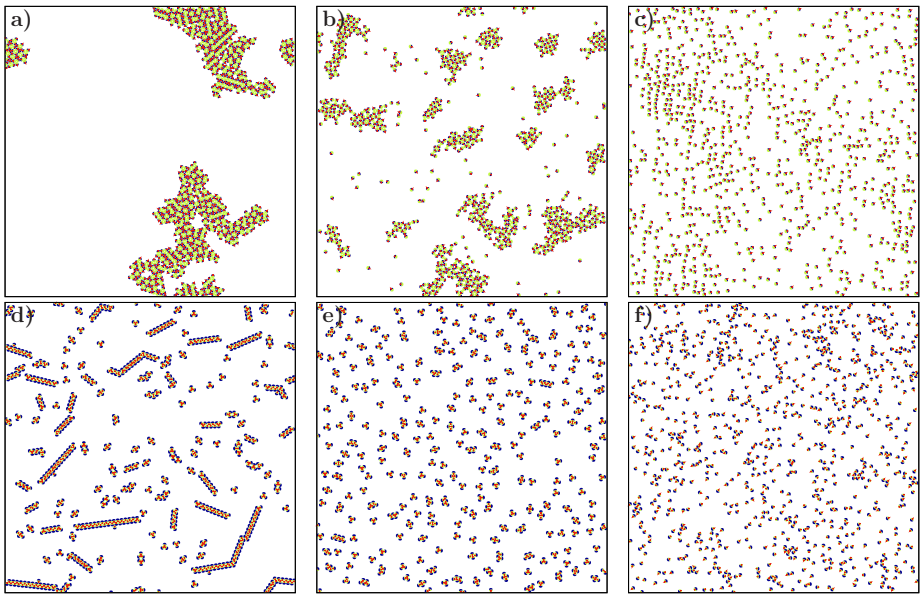

Figure 5.3: Simulation snapshots of different phases observed in this study. The attractive hemisphere is represented in green, while pure repulsive in blue and the fixed orientation vector is shown in red. (a), (b) and (c) are AP squirmer suspensions with $\xi = \{0.1, 1, 10\}$ respectively, while (d), (e) and (f) are WP squirmer suspensions with $\xi = \{0.1, 1, 10\}$ respectively. $r_{cutoff} = 2.5\sigma$ in all the cases. **(a):** Coarsening state with $\beta = 3$. **(b):** Finite clusters state with $\beta = 3$. **(c):** Gas state with polar order (polar gas phase) with $\beta = 0$. **(d):** Chains state with $\beta = 0$. **(e):** Trimers state with $\beta = -3$. **(f):** Gas state with nematic order (nematic gas phase) with $\beta = 0$.

In coarsening cases (figure 5.3 (a)), clusters do not reach a stationary mean value $\langle s \rangle$. Coarsening is observed in most cases in which attraction dominates over viscous effects. In those cases in which clusters reach a large yet finite mean value, we can distinguish the rounded clusters (figure 5.3 (b)) and elongated chains (figure 5.3 (d)). Chains can coexist with simpler structures, consisting of aggregates of three or four particles. These structures can also be observed as the only structure present in the system (figure 5.3 (e)), and they act as the precursor structure that leads to the formation of longer chains; they appear only when the sign of the interaction is WP. Finally, even if in some cases, in which hydrodynamic effects dominate over particle interaction, there is no aggregate formation, we can still measure polar order (figure 5.3 (c)) or nematic order (figure 5.3 (f)) in the resulting gas of swimmers. Whether gases can or not exhibit internal order depends on the hydrodynamic signature of the squirmers, while the kind of order depends on the sign of the interaction. In

the next sections we will introduce the quantitative measurements which allow us to better identify each morphology.

5.3.2 Mean cluster size

We compute the mean cluster size as a function of time to identify when the system reaches a steady state. In absence of thermal fluctuations (as in this work), passive Janus suspensions would coarsen; active suspensions can either coarsen or reach a steady state characterized by a distribution of cluster of different sizes, depending on the magnitude of β and ξ.

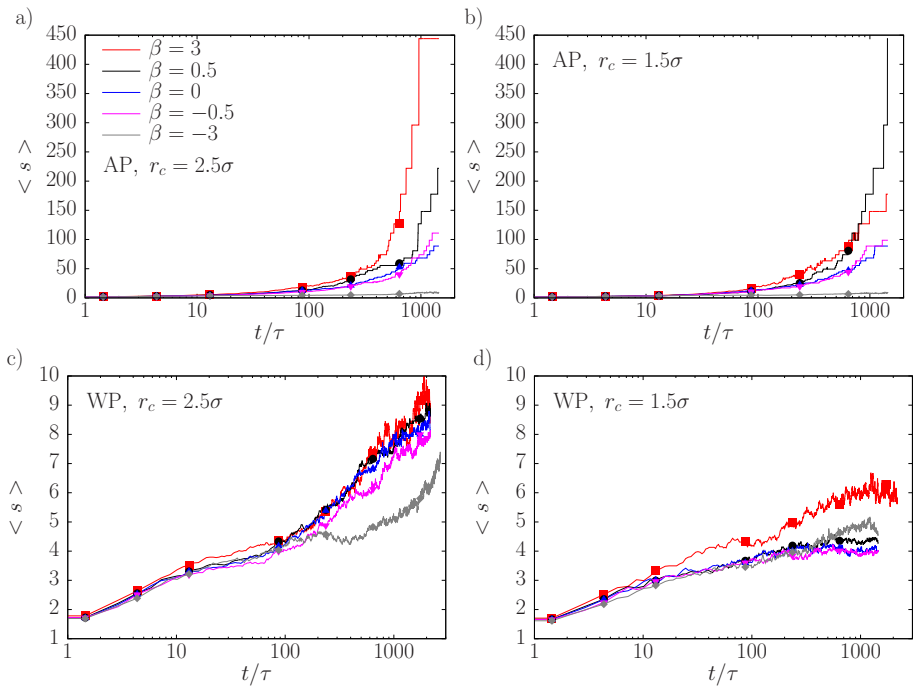

Figure 5.4: Time evolutions of the mean cluster size for suspensions with $\xi = 0.1$. **(a):** AP squirmers with $r_c = 2.5\sigma$. **(b):** AP squirmers with $r_c = 1.5\sigma$. **(c):** WP squirmers with $r_c = 2.5\sigma$. **(d):** WP squirmers $r_c = 1.5\sigma$. Curves for pullers are red and black, while pushers are pink and grey and $\beta = 0$ in blue.

In figure 5.4 we show the temporal evolution of the mean cluster size $\langle s \rangle$ as a function of time for weakly active Janus suspensions ($\xi = 0.1$). Coarsening cases, in which the mean cluster size does not reach a steady value, thus they tend to coalesce asymptotically to form a unique cluster, are possible for AP suspensions, independently of the interaction reach r_c (figures 5.4 (a) and (b)). There is a positive dependency of the growth velocity with β, as higher values show a faster coarsening process. Eventually, for $\beta = -3$ (grey curves) we observe the mean cluster size saturating at a value $\langle s \rangle \approx 10$ for both values of r_c.

It is not clear if particles interacting WP with $r_c = 2.5\sigma$ (figure 5.4 (c)) could eventually reach a finite cluster size, although in our simulation window

they did not. The cluster growth rate has again a positive dependence with β, reaching a value of $\langle s \rangle \approx 9$ for $\beta = 3$ (red curve) and $\langle s \rangle \approx 7$ for $\beta = -3$ (grey curve) at the end of our simulations. On the other hand, when $r_c = 1.5\sigma$ (figure 5.4 (d)) we can assure mean cluster size reaches a steady value for all values of β within the simulation window, with $\beta = 3$ reaching a higher value than the other cases, which show a slight dependency with $|\beta|$.

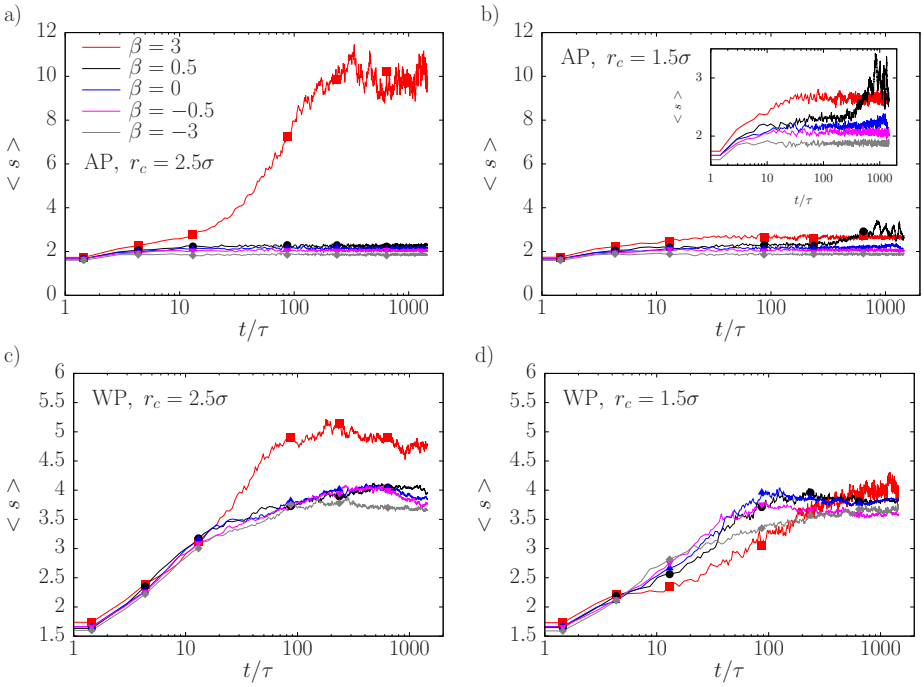

Figure 5.5: Time evolutions of the mean cluster size for suspensions with $\xi = 1$. **(a):** AP squirmers with $r_c = 2.5\sigma$. **(b):** AP squirmers with $r_c = 1.5\sigma$. **(c):** WP squirmers with $r_c = 2.5\sigma$. **(d):** WP squirmers $r_c = 1.5\sigma$. Curves for pullers are red and black, while pushers are pink and grey and $\beta = 0$ in blue.

In figure 5.5 we showcase the temporal evolution of the mean cluster size $\langle s \rangle$ for $\xi = 1$. In all cases, clusters reach a steady mean size. The growth rate and final size depend on β and the reach r_c. For AP squirmers with $r_c = 2.5\sigma$ (figure 5.5 (a)), the case $\beta = 3$ (red curve) outstands over the rest, reaching $\langle s \rangle \approx 10$, while the other cases barely pass $\langle s \rangle = 2$, with a positive dependence of the final size with β. When $r_c = 1.5\sigma$ (figure 5.5 (b)), all mean cluster sizes lie between 2 and 3 (see the inset for more detail), with pullers forming larger aggregates than pushers. WP squirmers show an analogous behaviour to their AP counterpart for this value of ξ. When $r_c = 2.5\sigma$ (figure 5.5 (c)), suspensions with $\beta = 3$ (red curve) form slightly larger aggregates than the rest ($\langle s \rangle \approx 5$ versus $\langle s \rangle \approx 4$), while for $r_c = 1.5\sigma$ all values of β reach similar values, lying between 3.5 and 4.

Finally, in figure 5.6 we display the temporal evolution of the mean cluster size $\langle s \rangle$ for those cases in which hydrodynamic interaction is dominant ($\xi = 10$).

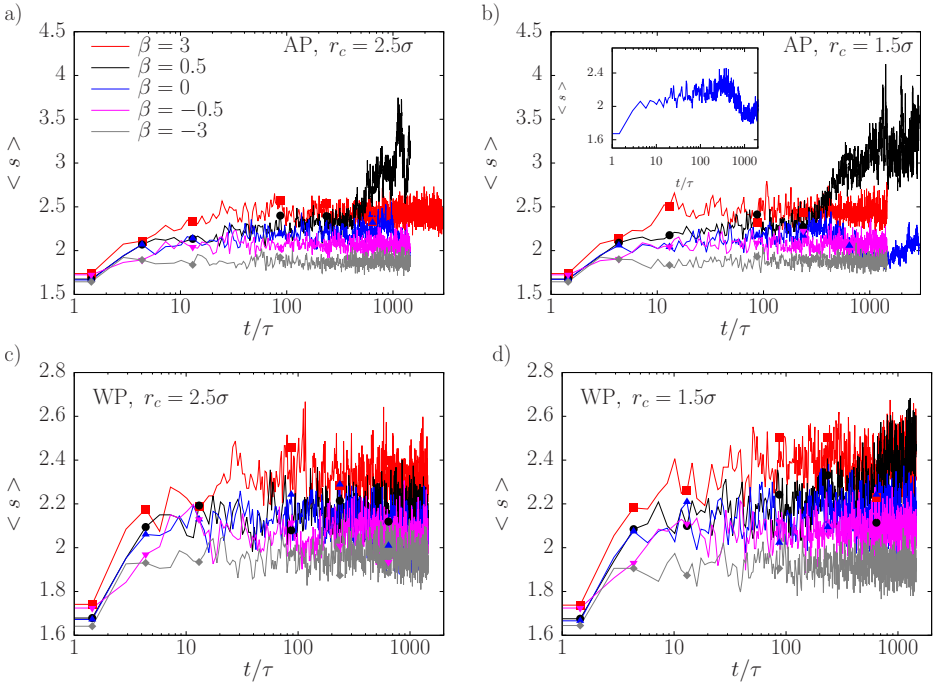

Figure 5.6: Time evolutions of the mean cluster size for suspensions with $\xi = 10$. **(a):** AP squirmers with $r_c = 2.5\sigma$. **(b):** AP squirmers with $r_c = 1.5\sigma$. **(c):** WP squirmers with $r_c = 2.5\sigma$. **(d):** WP squirmers $r_c = 1.5\sigma$. Curves for pullers are red and black, while pushers are pink and grey and $\beta = 0$ in blue.

The dependency with r_c in these cases is barely appreciable, as pairs of panels (a) and (b) (AP cases) and (c) and (d) (WP cases) are almost identical. For the AP cases, suspensions with $\beta = 0.5$ (black curve) form slightly larger aggregates, with $\langle s \rangle > 3$, while for the rest of cases $\langle s \rangle < 2.5$. This sudden growth appears late on the simulation (around ~ 500 time periods), while the other cases reach their final value almost immediately (less than 100 periods). For WP cases, all curves follow the same trend, reaching their steady value almost immediately (20 time periods), with $\langle s \rangle < 3$. Due to the low size of aggregates under these conditions, their mean value is more sensible to occasional collisions between particles, thus resulting in noisier curves.

In figure 5.7 we summarize these results by plotting the mean cluster size as a function of β, separating $r_c = 2.5\sigma$ (panel (a)) from $r_c = 1.5\sigma$ (panel (b)) when $xi = 10$ and $\xi = 1$. Overall, a longer interaction range leads to the formation of slightly larger aggregates. For AP interaction and $\xi = 1$ (pink triangles), we observe the most notorious difference. In both cases, $\langle s \rangle$ stays around 2 for pushers and neutral swimmers ($\beta = 0$). However, differences arise for pullers, with a continued growth with β when $r_c = 2.5\sigma$, while for $r_c = 1.5\sigma$ there is a peak at $\beta = 0.5$ equivalent to the one observed (for both interaction ranges) when $\xi = 10$. For WP squirmers, the differences induced by the interaction range are more subtle. For $\xi = 1$, $\langle s \rangle$ remains roughly around 4 for all values of β, while for $\xi = 10$ it goes down to 2, with a peak at $\beta = 0.5$ when $r_c = 1.5\sigma$

not observed when $r_c = 2.5\sigma$. Besides this peak, the general trend is that $\langle s \rangle$ grows slightly with β.

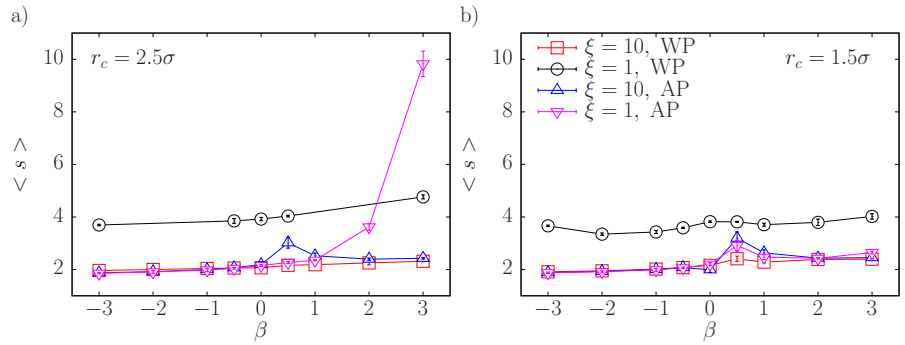

Figure 5.7: Mean cluster size at the steady state. Suspensions with **(a):** $r_c = 2.5\sigma$ and **(b):** $r_c = 1.5\sigma$. Coarsening cases (AP with $\xi = 0.1$) have been excluded from representation.

5.3.3 Cluster size distribution

As we did in the previous chapter (4.3.2), after computing the mean cluster size we compute the cluster size distribution (abbreviated CSD in this chapter). From here on, we will limit the results to the cases with $\xi = 10$ and $\xi = 1$, as for $\xi = 0.1$ it was either clear there was coarsening or at least it was not clear the system had reached a steady state (with the exception of WP squirmers with $r_c = 1.5\sigma$ and few others). Following previous studies [Alarcón et al., 2017] where CSDs were calculated, we have used the same analytical function to fit them:

$$\frac{f(s)}{f(1)} = A\,\frac{\exp(-(s-1)/s_0)}{s^{\gamma_0}} + B\,\frac{\exp(-(s-1)/z_0)}{s^{-\gamma_0}}, \tag{5.10}$$

with γ_0, s_0, z_0 and B constants such that $A = 1 - B$.

In figure 5.8, we show the cases with $\xi = 1$. These simulations were run with four times more particles precisely to obtain smoother CSD. The AP cases display a majority of monomers, and the probability of clusters belonging to greater clusters decays with its size. They can generally be fitted by a function of the form of equation 5.10; we display in panels (a) and (b) $f(s) = f(1)\exp(-(s-1)/4)/s^{5/4}$ as a guide to the eye, though it fits pretty well the cases with $\beta = 0$ when $r_c = 2.5\sigma$ (blue triangles in figure 5.8 (a)) and $\beta = -0.5$ when $r_c = 1.5\sigma$ (pink triangles in figure 5.8 (b)). When $r_c = 2.5\sigma$ (panel (a)), only the case with $\beta = 3$ (red squares) follows a different trend, as it exhibits a second peak (or at least a plateau) for $s \approx 30$. The other four CSD are pretty similar to each other, with their width (which can be controlled by adjusting the parameter s_0 in equation (5.10)) increasing slightly with β. For $r_c = 1.5\sigma$ (panel (b)), pullers have more narrow CSD, while for pushers, specially $\beta = 0.5$ (black circles), and neutral swimmers (blue triangles), CSD

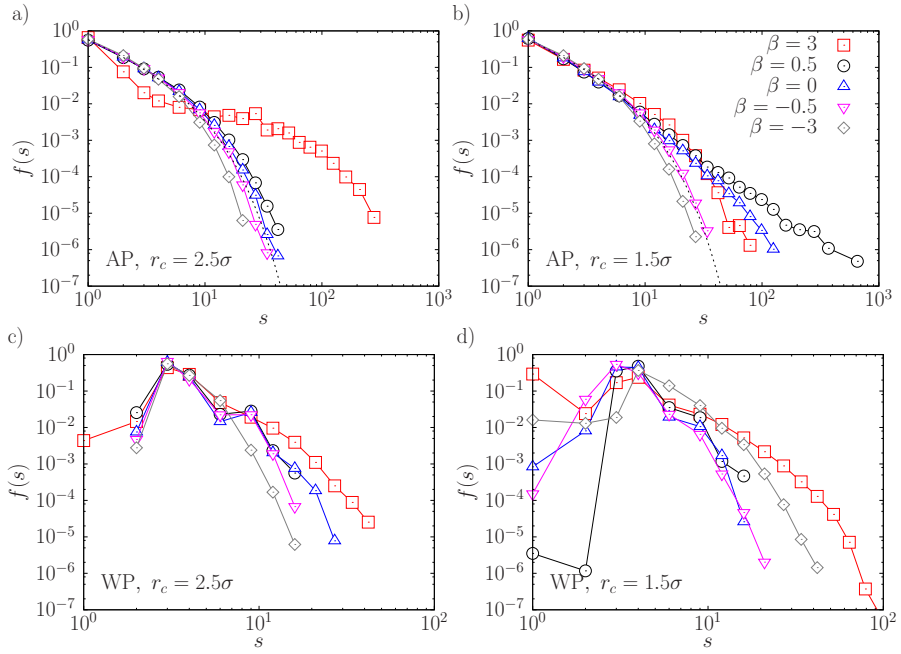

Figure 5.8: Cluster size distributions for suspensions with $\xi = 1$. **(a):** AP squirmers with $r_c = 2.5\sigma$. **(b):** AP squirmers with $r_c = 1.5\sigma$. **(c):** WP squirmers with $r_c = 2.5\sigma$. **(d):** WP squirmers $r_c = 1.5\sigma$. Grey dashed line in (a) and (b) represent the analitical function for a CSD given by (5.10) with $B = 0$, it is plotted as guide to the eye for the results, with $s_0 = 4$, $\gamma_0 = 5/4$.

are wider.

On the other hand, CSD for WP particles (figure 5.8 (c) and (d)) cannot be fitted by equation (5.10). In these cases, CSD have a maximum for $s = 3$ associated to the formation of micelles of three and four particles, which also have an associated value pretty high in all the CSD we display; these structures are the basic building blocks which lead to the formation of larger aggregates (chains in figure 5.3 (d)) for lower values of ξ. When $r_c = 2.5\sigma$ (panel (c)), the sharpness of the CSD depends on β, thus pushers have narrow distributions with no monomers and which quickly decay with size, while the opposite case of $\beta = 3$ (red squares) has a significant presence of both monomers and aggregates of tens of particles. This trend on the sharpness of distributions is kept for $r_c = 1.5\sigma$ (figure 5.8 (d)). The main difference is that the presence of isolated particles is increased respect to the longer interaction range, and distributions are cut at shorter values of s.

When activity dominates, as shown in figure 5.9, corresponding to $\xi = 10$, the resulting CSD are more adjustable by equation (5.10) with $B = 0$. For AP swimmers (panels (a) and (b)), the behaviour for both interaction ranges ($r_c = 2.5\sigma$ and $r_c = 1.5\sigma$) are pretty similar to each other and analogous to what we already observed for $\xi = 1$ with $r_c = 1.5\sigma$ (figure 5.9 b)). Pushers have distributions that decay faster to 0, while the tail for $\beta = 0.5$ is longer,

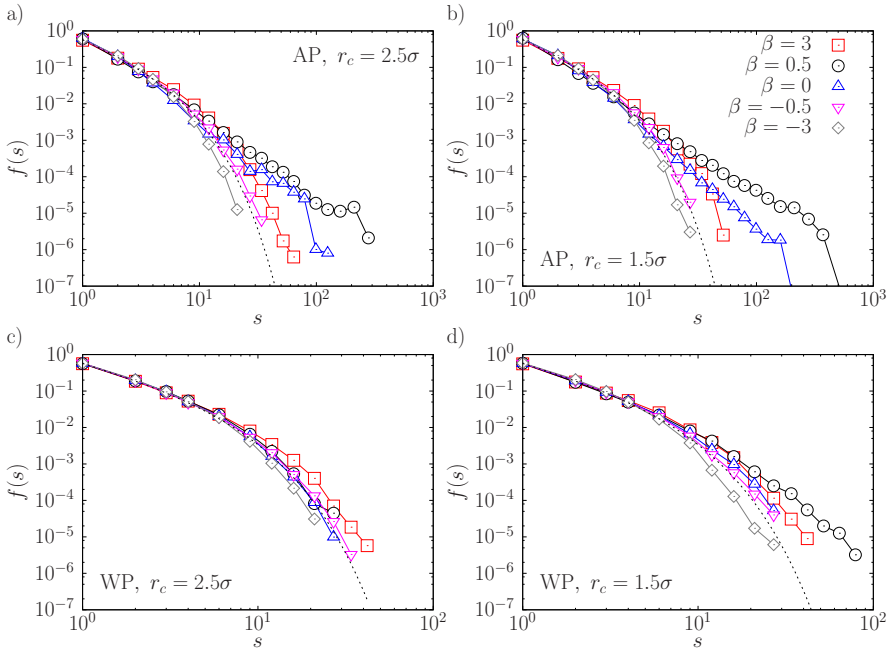

Figure 5.9: Cluster size distributions for suspensions with $\xi = 10$. **(a):** AP squirmers with $r_c = 2.5\sigma$. **(b):** AP squirmers with $r_c = 1.5\sigma$. **(c):** WP squirmers with $r_c = 2.5\sigma$. **(d):** WP squirmers $r_c = 1.5\sigma$. Grey dashed line in (a) and (b) represent the analytical function for a CSD given by equation (5.10) with $B = 0$, it is plotted as guide to the eye for the results, with $s_0 = 4$, $\gamma_0 = 5/4$.

indicating the presence of larger aggregates in the system; additional peaks at high values of s are likely due to lack of statistics.

At this level of activity, WP swimmers do not longer exhibit a preference to form micelles of three or four particles, exhibiting instead an exponential decay of their cluster size which can be fitted by equation (5.10). For $r_c = 2.5\sigma$ (figure 5.9 (c)), β barely makes any difference, with all five curves being almost coincidental, although pullers can form slightly greater aggregates than pushers. For $r_c = 1.5\sigma$ (panel (d)), pullers with $\beta = 0.5$ have a longer tail, while the distribution for strong pushers is cut before.

5.3.4 Radius of gyration

The cluster morphology is characterized by computing the dependence of the radius of gyration of the clusters $R_g(s)$ with their size, s, using equation (5.7).

Both in figures 5.10 and 5.11, the radius of gyration is fitted to a power law with the cluster size, $R_g(s) \propto s^{0.64}$, which is followed by most of the curves. In figure 5.10 (c) and (d), corresponding to WP squirmers with $\xi = 1$, we observe a crossover past $s = 4$ for which there is a sudden growth in $R_g(s)$ before returning to its typical growth. We can associate it to a transition from micelles to clusters

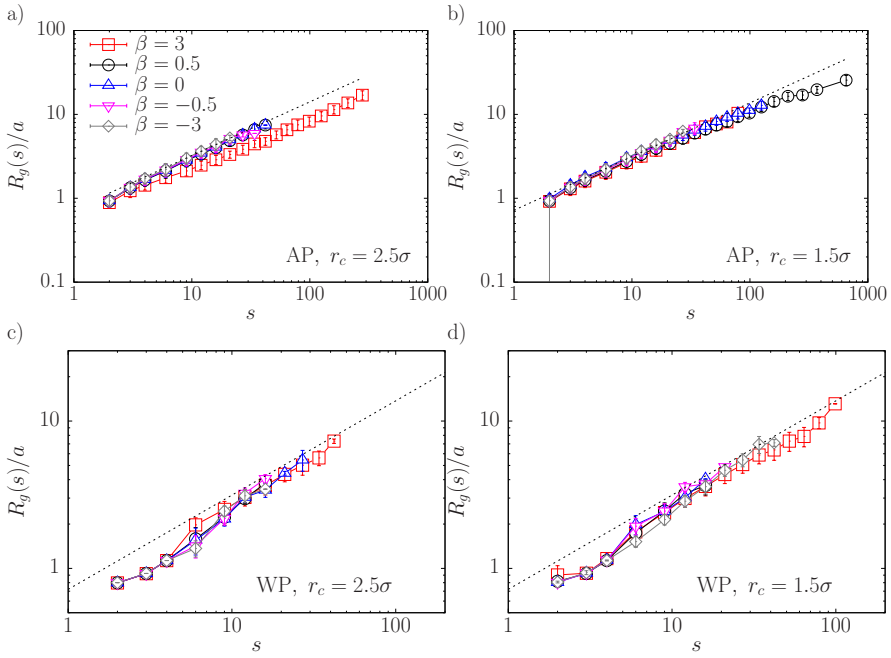

Figure 5.10: Radius of gyration normalized by particle radius as a function of cluster size for suspensions with $\xi = 1$. **(a):** AP squirmers with $r_c = 2.5\sigma$. **(b):** AP squirmers with $r_c = 1.5\sigma$. **(c):** WP squirmers with $r_c = 2.5\sigma$. **(d):** WP squirmers $r_c = 1.5\sigma$. Grey dashed lines in all panels are the function $R_g \propto s^{0.64}$ and most of the curves fit with this power law function.

with elongated shapes. We do not observe this crossover for any other case, neither for AP swimmers with the same value of ξ (panels (a) and (b) in figure 5.10, nor for any of the observed cases with $\xi = 10$ (figure 5.11), for which there is no chain formation and clusters tend to be more isotropic. For AP swimmers with $\xi = 10$, there is a drop in the growth rate of the radius of gyration for large sizes.

The radius of gyration is a parameter that should help us identify the morphology of clusters, thus it would have been more interesting computing it for the cases with low values of ξ, as in those cases chains are more frequent and it would have showed significant differences between the AP and WP cases. However, the fact that steady states are rarely reached for such simulations prevented us from having a more interesting analysis of this parameter, being limited to a collection of more isotropic cases.

5.3.5 Global polar and nematic order

So far, we have characterized Janus squirmer suspensions by studying the clustering of the suspensions, its morphological properties and statistics. Now we also want to study the orientational properties. To do so, we have calculated the global polar order parameter at long time, following a similar procedure as in [Alarcón and Pagonabarraga, 2013]. Additionally, we also calculated another

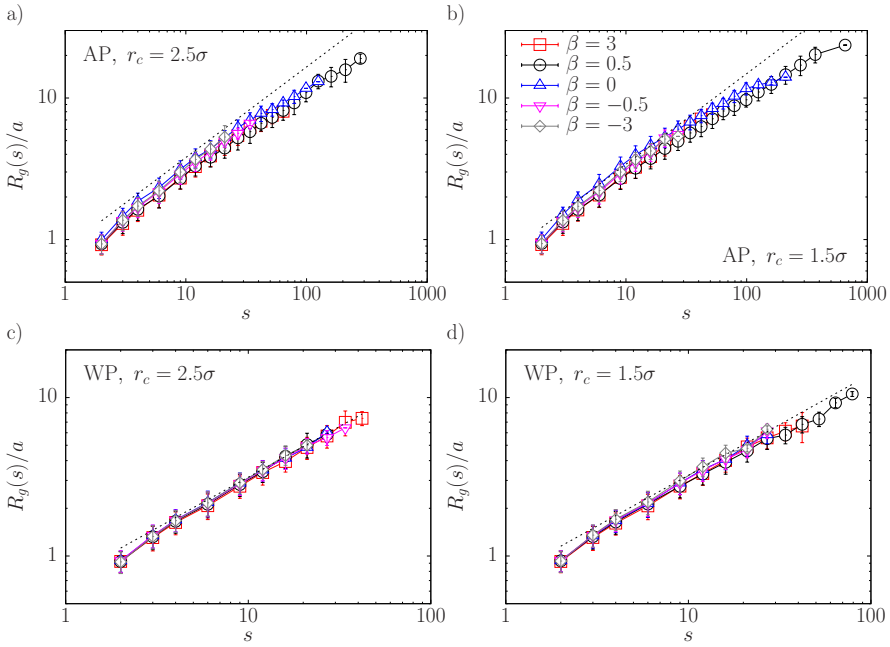

Figure 5.11: Radius of gyration normalized by particle radius as a function of cluster size for suspensions with $\xi = 10$. **(a):** AP squirmers with $r_c = 2.5\sigma$. **(b):** AP squirmers with $r_c = 1.5\sigma$. **(c):** WP squirmers with $r_c = 2.5\sigma$. **(d):** WP squirmers $r_c = 1.5\sigma$. Grey dashed lines in all panels are the function $R_g \propto s^{0.64}$ and most of the curves fit with this power law function.

orientational parameter using the nematic order tensor (equation (5.9)).

In figure 5.12 we plot the value of both global order parameters as a function of β. We separate AP cases from WP in our exposition. For the former, we find that those cases that already exhibited clusters with internal alignment also keep it for the whole system. Global polar order is maximized for suspensions with $\beta = 0$ for $\xi = 10$ and $\xi = 1$ for the shorter interaction range $r_c = 1.5\sigma$. In those cases, it still displays non-null values for weak pullers, which decay to 0 at $\beta > 1$. No pushers have polar order. Cases with $\xi = 1$ and $r_c = 2.5\sigma$ do not exhibit polar order either. For AP swimmers, there is an almost one on one correlation between polar and nematic order.

Global polar order also follows the trend of local polar order we already discussed for WP swimmers. Therefore, it is null for all cases except weak pullers with $\xi = 10$ and $r_c = 1.5\sigma$, corresponding this later pair of parameters to the most activity dominated scenario. However, we do observe the apparition of nematic order for weak $\beta = 0$ and $\beta = -0.5$ for $\xi = 10$ and $r_c = 2.5\sigma$.

5.3.6 Local polar and nematic order

We measure the degree of alignment inside a cluster as a function of its size. Polar order is computed using equation (5.8). It is defined as 1 for isolated par-

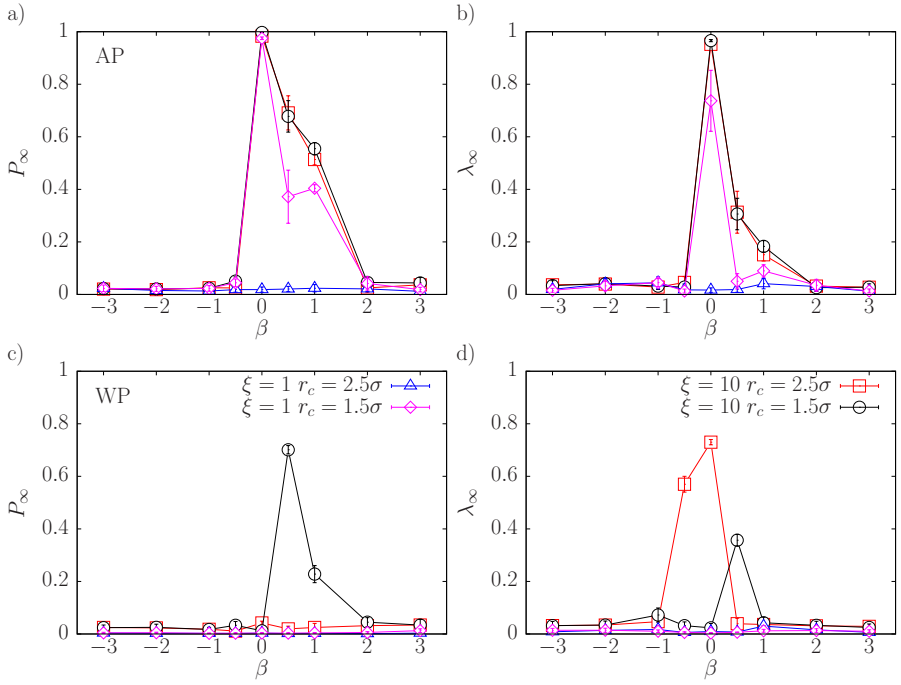

Figure 5.12: Global polar and nematic order parameters. **(a):** Polar order parameter P_∞ for AP squirmers. **(b):** Nematic order parameter λ_∞ for AP squirmers. **(c):** Polar order parameter P_∞ for WP squirmers. **(d):** Nematic order λ_∞ for WP squirmers.

ticles, and then decreases with cluster size. This decay usually follows a power law of the cluster size for isotropically interacting squirmers [Alarcón et al., 2017].

As we could expect, anisotropically interacting squirmers do not follow such a bland behaviour. Let us begin analyzing the cases with $\xi = 1$ (figure 5.13). Local polar order for AP squirmers with $r_c = 2.5\sigma$ decays quickly with the cluster size, almost identically for all values of β but $\beta = 3$ (red squares in panel (a)), which exhibits an even faster decay. Differences arise when reducing the interaction range for AP swimmers to $r_c = 1.5\sigma$ (figure 5.13 (b)). Local polar order remains close to 1 for sizes of up to roughly 80 particles for $\beta = 0$ (blue triangles), and also shows a slower decay for $\beta = 0.5$ (black circles). The other cases (including $\beta = 3$) show a similar behaviour, equivalent to the general trend observed for $r_c = 2.5\sigma$.

WP squirmers (figure 5.13 (c) and (d)), on the other hand, exhibit an abrupt decay to an almost null local polar order for sizes greater than one. The only exception to this trend is the case $\beta = 3$ with $r_c = 1.5\sigma$ (red squares in panel (d)), which has non-null polar order for dimers, and after a minimum for trimers decays smoothly for $s \geq 4$. This general behaviour of WP squirmers can be easily explained by the formation of micelles of three and four particles with their director vectors pointing at each other, thus cancelling the polar order.

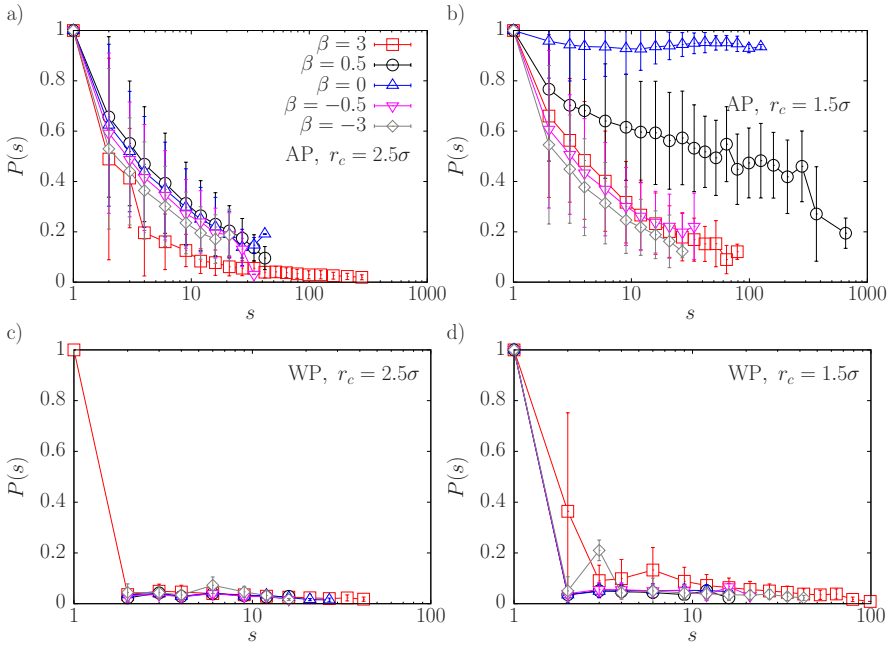

Figure 5.13: Polar order as a function of cluster size for suspensions with $\xi = 1$. **(a):** AP squirmers with $r_c = 2.5\sigma$. **(b):** AP squirmers with $r_c = 1.5\sigma$. **(c):** WP squirmers with $r_c = 2.5\sigma$. **(d):** WP squirmers $r_c = 1.5\sigma$.

In figure 5.14 we display the local polar order as a function of cluster size for activity dominated scenarios ($\xi = 10$). For AP swimmers (panels (a) and (b)), the interaction range barely makes any difference, as its role is subdominant. For neutral swimmers ($\beta = 0$, blue triangles), particles inside a cluster are always aligned in the same direction, while the cases with $\beta = 0.5$ (black circles) also show a significant amount of polar order. The rest of values of β exhibit a more standard decay of their local polar order with cluster size.

Interaction range plays a role for WP squirmers (figure 5.14 (c) and (d)). For this value of ξ, there is no formation of micelles and polar order no longer decays abruptly with cluster size. In most cases, it does so smoothly, with the exception of weak pullers ($\beta = 0.5$) for $r_c = 1.5\sigma$ (black circles in panel (d)), in which there is a persistent polar order around 0.7 for all cluster sizes.

Nematic order λ is measured as the largest eigenvalue of the tensor Q_{hk} given by equation (5.9). In figures 5.15 and 5.16 we depict the internal nematic order inside a cluster as a function of its size. As happened with polar order, the general trend is that it decays monotonously with the cluster size.

For AP swimmers with $\xi = 1$ and $r_c = 2.5\sigma$ (figure 5.15 (a)), λ is a decreasing function of s for all values of β, and with the exception of $\beta = 3$ (red squares) all curves are overlapped, thus hydrodynamic effects are barely noticeable. However, they arise when reducing the interaction range to $r_c = 1.5\sigma$

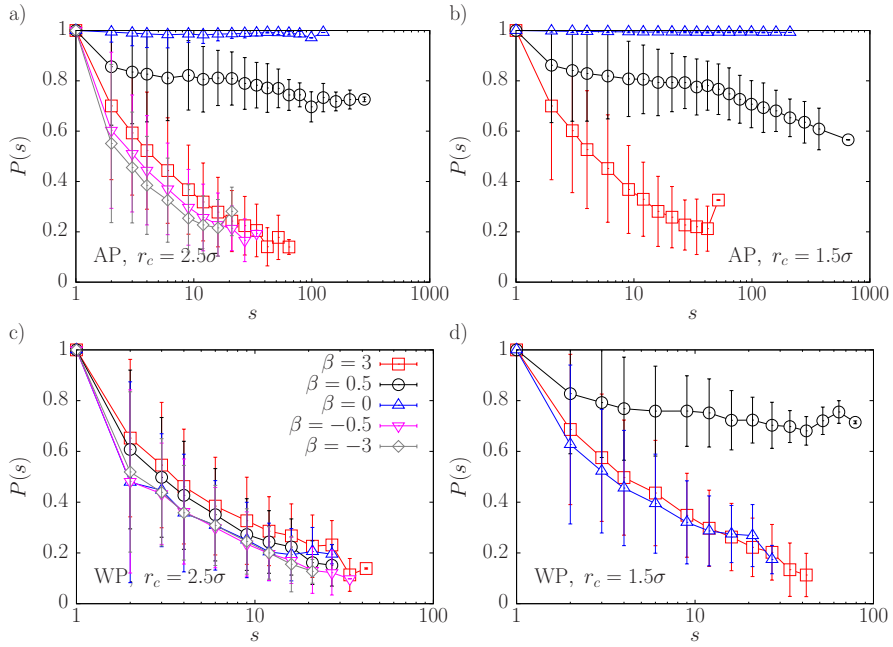

Figure 5.14: Polar order as a function of cluster size for suspensions with $\xi = 10$. **(a):** AP squirmers with $r_c = 2.5\sigma$. **(b):** AP squirmers with $r_c = 1.5\sigma$. **(c):** WP squirmers with $r_c = 2.5\sigma$. **(d):** WP squirmers $r_c = 1.5\sigma$.

(figure 5.15 (b)). Under these conditions, $\beta = 0$ (blue triangles) has an anomalous behaviour, following a trend similar to other cases up to $s \approx 20$, which presents a minimum of λ followed by a growth up to a maximum located at $s \approx 80$. For this particular value of β, the nematic order behaves differently to the polar one (figure 5.13 (b)), which remains constant until the value at which we found this maximum. For $\beta = 0.5$, the nematic order decays slower than for the rest of values.

For this value of ξ, WP swimmers typically form micelles of 3 or 4 particles with null nematic order associated, which is evidenced by the minima in curves in figures 5.15 (c) and (d). For $r_c = 2.5\sigma$, $\beta = 3$ is the only case which differs from the rest, remaining close to 0 also for greater values of s. For $r_c = 1.5\sigma$, the most remarkable case is $\beta = -3$, which after the minimum at 3 and 4 keeps a nematic order $\lambda \approx 0.3$ constant up to ≈ 40 particles, while other values of β have almost overlapping curves.

The description of figure 5.15 (b) could be applied to figure 5.16 (a), implying that the reduction in the intensity of the interaction between particles is compensated by the increase in the interaction range. Shortening the interaction range with $\xi = 10$ (panel (b)), the case $\beta = 0$ keeps a constant nematic order value for all cluster sizes (except our last outlier point). Again, $\beta = 0.5$ decays slower than the rest of values of β.

For $\xi = 10$, the nematic order for WP squirmers always decays with cluster

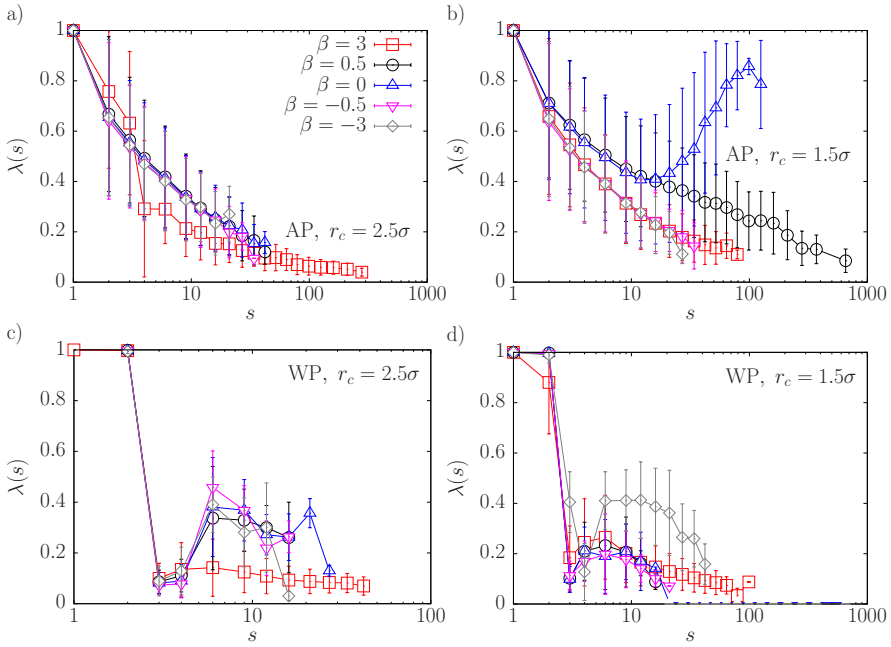

Figure 5.15: Nematic order as a function of cluster size for suspensions with $\xi = 1$. **(a):** AP squirmers with $r_c = 2.5\sigma$. **(b):** AP squirmers with $r_c = 1.5\sigma$. **(c):** WP squirmers with $r_c = 2.5\sigma$. **(d):** WP squirmers $r_c = 1.5\sigma$.

size. However, we should highlight the lack of concavity of the curves $\lambda(s)$ for $\beta = 0$ (blue triangles) and $\beta = -0.5$ (pink triangles) when $r_c = 2.5\sigma$ (figure 5.16 (c)).

5.4 Conclusions

In this chapter we have studied numerically semi-dilute quasi-two-dimensional suspensions of active Janus swimmers. The active character of swimmers was modelled through the squirmer model, while their Janus character led to an anisotropic interaction between them, modelled by a Lennard-Jones interaction weighted by a function dependent on the relative orientation of particles. This has allowed us to study systematically the effect of anisotropy on the formation of aggregates of swimmers, as well as their morphology and the alignment in the system. We have weighted the effect of this interaction against active stresses, as well as studied the effect of its range of action.

Janus squirmers show a richer variety of morphologies than the isotropic case [Alarcón et al., 2017], allowing us to identify six different morphologies (listed in section 5.3.1), associated either to particle aggregation or the emergence of spontaneous ordering in the system.

The formation of aggregates is mainly dominated by the interaction strength,

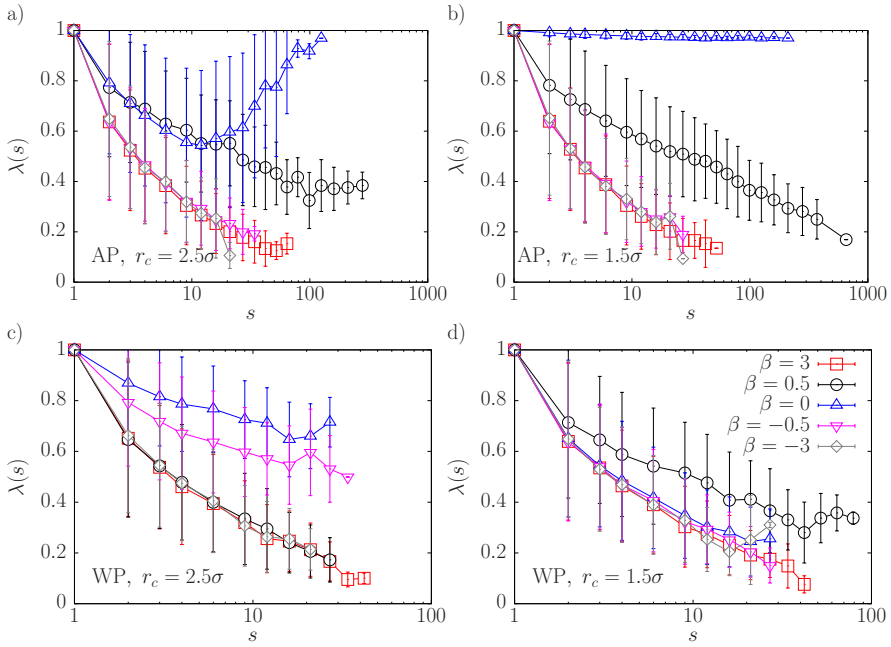

Figure 5.16: Nematic order as a function of cluster size for suspensions with $\xi = 10$. **(a):** AP squirmers with $r_c = 2.5\sigma$. **(b):** AP squirmers with $r_c = 1.5\sigma$. **(c):** WP squirmers with $r_c = 2.5\sigma$. **(d):** WP squirmers $r_c = 1.5\sigma$.

measured by the parameter ξ (equation 5.1). When it is dominant (low values of ξ), large aggregates appear, eventually leading to the coalescence of the system into a single aggregate under certain conditions; on the other hand, when hydrodynamic effects dominate (high values of ξ), there is no aggregate formation and we observe a gas of particles. Finer details on the cluster size, shape and ordering then depend on the sign of the attraction, its reach and the hydrodynamic signature of the swimmers. We have summarized the results in figure 5.17.

The sign of the interaction (whether it is AP or WP) determines the aggregation mechanism. WP squirmers can form micelles of three or four particles with the director vector of their particles pointing at each other at moderate values of interaction strength ($\xi \sim 1$). Under these conditions, it will be a frustrated structure that can no longer grow, leading to their proliferation into the system. Increasing the interaction strength or its reach, these micelles can merge into larger aggregates, which usually have elongated shapes. Chain formation is also favoured by low values of $|\beta|$. In some cases ($\xi = 0.1$ and $r_c = 2.5\sigma$), we have not been able to determine whether this growth mechanism eventually stops at a finite size or leads to an indefinite growth of the chains (and eventually its coalescence); nonetheless, we can claim the growth of chains is a slow process.

On the other hand, AP squirmers do not form any finite size structure, and once the attraction becomes dominant, the system coarsens. β determines the growth rate, with a positive dependence (pullers grow faster than pushers). We observe the growth for strong pushers ($\beta \geq 3$) to stop at finite sizes, with ag-

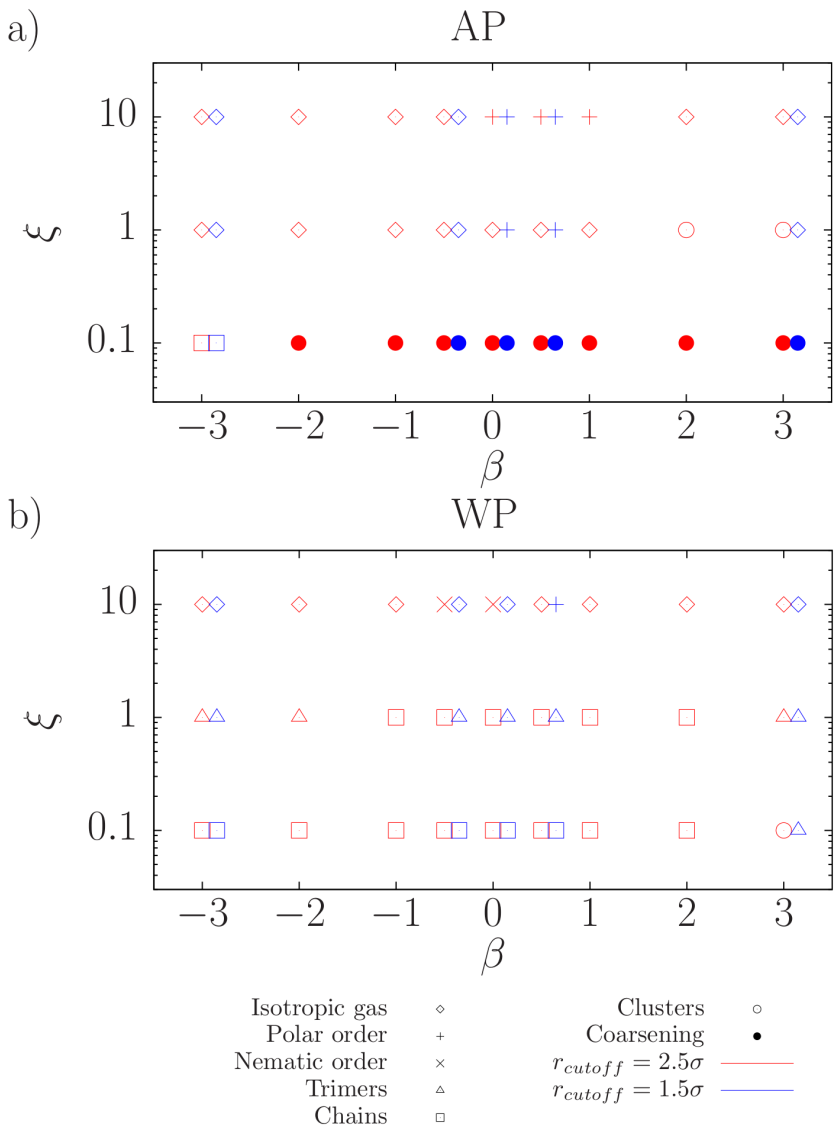

Figure 5.17: Diagram with the observed morphologies for: **(a)** AP interacting particles and **(b)** WP interacting particles. The possible morphologies are: isotropic gas ($\diamond$), gas with global polar order ($+$), gas with global nematic order ($\times$), micelles of three and four particles ($\triangle$), elongated clusters ($\square$), finite size rounded clusters ($\circ$) and coarsening ($\bullet$). Cases with $r_c = 2.5\sigma(1.5\sigma)$ are represented with red (blue) symbols.

gregates with elongated shapes as well.

When the particle interaction is not dominant, no aggregates are formed, but spontaneous order can still emerge in the gaseous squirmer suspension. For the AP attraction, neutral squirmers ($\beta = 0$) and weak pullers ($0 < \beta < 1$)

swim in a coherent way when hydrodynamic effects are more dominant ($\xi = 10$ and $r_c = 1.5\sigma$ with $\xi = 1$), while their motion is disordered in the other cases. For WP squirmers, we find more surprising results, as the resulting order does not only depend on β but also on the potential reach. For this sign of the interaction, we have only observed gases for $\xi = 10$. For $r_c = 1.5\sigma$, we observed polar order for weak pullers. However, for $r_c = 2.5\sigma$, this order is destroyed for weak pullers, but instead we observe nematic order (squirmer population is split into two groups that displace in opposite directions) for $\beta = 0$ and $\beta = -0.5$.

Chapter 6

Conclusions

What fools call "wasting time" is most often the best investment.

Nassim Taleb

There is a conclusions section at the end of each chapter. It is time to summarize them and add future perspectives in the research lines we have opened with this thesis.

Chapter 2 was pretty introductory. We introduced the dynamic equations that describe the coupled rotation of the magnetic moment of a colloid and the particle itself, taking into account different magnetic properties the particle could have. We limited the resolution of these models to cases in which the magnetic moment rotates synchronously with a circularly oscillating magnetic field; however, the presented equations are more general than that, and could be used for other applied magnetic fields. We implemented some of these models (ferromagnetic, paramagnetic simple and paramagnetic with two magnetic moments) into our LB simulation scheme. Even if we argued that the ferromagnetic model is enough to have a collection of identical colloids rotating with the same angular velocity, paramagnetic models offer us the possibility to in the future study colloidal suspensions with inhomogeneous angular velocities. The particular dynamics of the magnetic moment might be a side bonus of our models that we might not be interested in at the scale at which we deal with magnetic colloids; however, studying the discrepancies between the predicted phase shift of the magnetic moment respect the field and the one found in LB simulations allowed us to find an interesting method to determine the hydrodynamic radius of a spherical colloid in LB simulations. We also introduced the forces acting on a suspension of magnetic colloids and defined two dimensionless parameters to estimate their relative importance.

In chapter 3 we introduced several arrays of magnetic colloids that can be formed. In section 3.1, we gave a review about magnetic worms [Martinez-Pedrero et al., 2015], and tested the validity of the simple hydrodynamic model given to describe them. Even if there was no complete agreement between model and simulations, it still is pretty surprising that a far-field model could capture so well the physics of a system of particles that are very close to each other and to the interface they creep over.

In section 3.2, we introduced the scenario in which hydrodynamic interactions are dominant over magnetic dipolar ones. Under these conditions, we found it is still possible to have bound states between couples of particles [Martinez-Pedrero et al., 2018], which have a tendency to align in a direction non-favoured by magnetic dipolar interaction. We proposed an hydrodynamic model to describe the motion of two rotors, based on the same far-field approximation of the previous section, but now allowing the particles to freely displace with a velocity induced by their neighbour. This model allows us to describe the motion of two rotors as a combined movement of the displacement of its centre of mass with a periodic oscillatory movement of one particle around the other. Two identical particles (same radius and angular velocity) aligned perpendicularly to the direction of their motion suppress this later mode of movement and displace while keeping this relative arrangement, a configuration observed experimentally but with a finite lifetime (which may be attributable to inhomogeneities in particle properties). We also studied the role of gravity in the system, which can hinder this periodic oscillatory relative motion of the pair and favour their alignment.

We also studied the flow created by longer structures with this particular geometry, called ribbons, [Massana-Cid et al., 2017], which can be used to transport passive particles. Finally, in section 3.3, we presented a first computational study to know under which conditions (characterized by the balances of forces we defined in the previous chapter), each array is favoured.

We pushed this study further in chapter 4, by studying the formation of arrays from a disordered initial state. Summarizing the results, we found that worms are formed for moderate magnetic interaction and high confinement; walkers appear for high magnetic interaction; ribbons for null magnetic interaction and moderate levels of confinement; windmills for low levels of magnetic interaction and confinement, while there is no self-assembly for high confinements and low magnetic interaction. Overall, we were capable of grouping under one theoretical framework the reports of several self-assembled arrays of magnetic colloids found in the literature, and elucidate under which conditions each of them is formed.

Directly controlling confinement is pretty hard, as it depends on buoyancy and electrostatic repulsion between particles and the substrate. This could be controlled varying the salt concentration in the fluid. Experimentally, confinement is enhanced by applying elliptic magnetic fields instead of circular ones [Martinez-Pedrero et al., 2015]. Our LB code could allow us to directly test the effect of field ellipticity, a work that could be worth a final degree project or a master thesis, either testing the conditions of section 3.3 or those of chapter 4.

Finally, in chapter 5 we changed our subject of study to Janus squirmers. We studied how the propulsion mechanism (characterized by the parameter β), the sign of the interaction between them (whether they swam with their attractive patches in front (WP) or behind (AP)) and the balance between anisotropic interactions and viscous forces affected to the formation of ordered states. We were capable of finding six different structures which present any degree of order: coarsening, finite size rounded clusters, chains, micelles of three or four particles, and gaseous phases with polar or nematic order. The strength of the interaction between particles tends to favour the formation of larger aggregates. The sign of the interaction (whether particles swim AP or WP) determines the mechanism of particle aggregation. WP swimmers tend to form micelles of three to four colloids pointing at each other; high levels of interaction and/or a long reach of the interaction that goes beyond first neighbours may promote the merging of several of these basic structures into larger aggregates, which tend to have elongated shapes. On the other hand, AP squirmers have a more radical behaviour, and they either coalesce or remain as a gas. β is the parameter with the least impact of the studied, although it does not mean it is negligible. When hydrodynamic effects are dominant, it determines whether squirmers can swim or not coherently. In cases in which there is particle aggregation, it qualifies the size of the resulting clusters. The presented study intends to be pretty complete in its regard, although the inconsistency in the choice of the potential is particularly troubling. This chapter was done in collaboration with the group led by Dr. Chantal Valeriani at the Universidad Complutense de Madrid, who

are already studying modifications of the interaction potential to make further comparisons to other results found in the literature, such as [Mallory et al., 2017].

Chapter 7

Resumen en castellano

El presente trabajo puede englobarse en el campo de la materia activa. Este campo es relativamente reciente y multidisciplinario, solapándose la física de no equilibrio, la biología y otras ciencias. Está centrado en el estudio de sistemas con componentes móviles capaces de transformar energía (almacenada internamente o del medio) en trabajo de manera sistemática. Dentro de la materia activa, se pueden diferenciar dos tipos: materia activa húmeda y seca. A pesar de que estos nombres hagan referencia al medio en el que se mueven los elementos activos, desde el punto de vista físico hacen referencia a sistemas en los que hay o no conservación del momento, respectivamente. Esta distinción también termina afectando a la escala de los sistemas estudiados y al enfoque que se hace de los mismos. Así, la materia activa seca suele lidiar con sistemas macroscópicos y hace hincapié en las interacciones entre sus componentes; el ejemplo más célebre es el modelo de Vicsek [Vicsek et al., 1995]. Sin embargo, también existen modelos secos para lidiar con agentes microscópicos, el más célebre de los cuales son las partículas brownianas activas (ABP por sus siglas en inglés). Por su parte, la materia activa húmeda también trata la interacción de los elementos móviles con el medio que los rodea, normalmente un fluido viscoso. El fluido también actúa como vector de una interacción adicional de largo alcance entre los agentes activos, las interacciones hidrodinámicas. La comparación directa entre resultados obtenidos con ambas descripciones puede permitir conocer el papel del solvente en los fenómenos observados.

Uno de los fenómenos más estudiados en el campo de la materia activa es el de la autoorganización. La autoorganización es un fenómeno apasionante, presente en todas las escalas, desde la formación de galaxias a la de los mismos átomos a partir de partículas elementales, pasando por la aparición de la vida y la evolución hacia organismos eucariotas y pluricelulares, amén de varias aplicaciones más mundanas en la industria química. Desde el punto de vista de la materia activa, se investiga cómo a partir de unas leyes elementales que se limitan a regir únicamente el movimiento individual de cada componente del sistema, estos luego pueden dar lugar a la formación de patrones o estructuras colectivos.

Como hemos mencionado con anterioridad, el medio a través del que los elementos activos se mueven cuando tratamos con materia activa húmeda es un

fluido viscoso. Desplazarse a través de un fluido viscoso es un reto no trivial. En esas condiciones, los efectos inerciales desaparecen, obligando al nadador a hacer trabajo constantemente para no quedarse parado. Los movimientos que haga un nadador en estas condiciones tampoco pueden ser cualesquiera. Para desplazarse, el nadador deberá deformar su cuerpo de manera que pueda impulsarse, y hacerlo cíclicamente para que su movimiento sea persistente. Sin embargo, un ciclo completamente reversible, en el que el nadador vuelva a su posición original siguiendo los mismos pasos que dio para impulsarse en orden inverso, daría lugar a un desplazamiento idéntico hacia atrás, sin importar cuán rápido se impulsase hacia adelante o cuán despacio regresara hacia atrás [Purcell, 1977]. Estas dificultades obligan a las células a buscar estrategias más sofisticadas para poder desplazarse.

Las suspensiones coloidales ofrecen muchas posibilidades como sistemas modelo para el estudio de la materia activa. Dentro de los mismos, aquellos con propiedades magnéticas son especialmente atractivos. Los coloides magnéticos tienen la ventaja de que pueden manipularse con un campo magnético externo, lo que permite desplazar a varios miles de ellos simultáneamente y de manera no invasiva. Entender cómo se desplazan con más detalle nos puede permitir optimizar su movimiento. Una estrategia habitual suele ser emplear campos magnéticos rotatorios. Al estudio de coloides magnéticos sometidos a un campo magnético circular hemos dedicado los capítulos segundo, tercero y cuarto de la tesis.

En el primero de esos capítulos hemos introducido los fundamentos de la dinámica de los coloides magnéticos sometidos a un campo magnético rotatorio. Combinando una ecuación de equilibrio de los momentos de fuerzas viscoso y magnético con la ecuación dinámica del momento magnético del coloide, podemos resolver la dinámica completa del coloide, hallando su velocidad angular y el giro de su momento magnético siguiendo al campo aplicado. Esto nos ha permitido estudiar cómo varía la dependencia de la velocidad angular del coloide con la frecuencia del campo magnético aplicado para distintas naturalezas magnéticas del momento del coloide. Cuando sacamos este coloide ideal de un medio aislado para colocarlo en un sistema más realista, aparecen interacciones adicionales: de un lado, otros coloides rotando crean un flujo que puede inducir una velocidad al coloide; por otro, dos momentos magnéticos interaccionan entre si mediante la interacción dipolar magnética, y por último, está el efecto de las anisotropías espaciales, creadas por la gravedad y la interfase del recipiente donde estén contenidos los coloides. La competición entre estas fuerzas será la que cambie las condiciones a las que están sometidas los coloides y determine cómo se organizan para desplazarse.

En el tercer capítulo de la tesis hacemos un estudio más detallado de casos en los que los coloides se desplazan alineados en hileras. En una primera sección, mostramos los efectos cooperativos de origen hidrodinámico que permiten primero que un coloide que rote sobre si mismo pueda desplazarse sobre una interfase con otro fluido o un sólido, y luego cómo este efecto es incrementado cuando dicho coloide se halla en una hilera alineada en la dirección de su movimiento (como un gusano). Hemos validado computacionalmente el modelo teórico y las observaciones experimentales presentadas en [Martinez-Pedrero

et al., 2015]. En una segunda sección, hemos estudiado una alineación perpendicular a la planteada en el caso anterior. Esta disposición no se ve favorecida por la interacción dipolar magnética entre coloides, ergo hemos planteado las ecuaciones dinámicas del sistema para un caso en el que no esté presente. De esta manera, hemos visto la formación de estados ligados de origen puramente hidrodinámico [Martinez-Pedrero et al., 2018] y calculado el flujo que una hilera con esta geometría crea [Massana-Cid et al., 2017]. Este hecho evidencia el rol de la competición de fuerzas presente en el sistema a la hora de determinar la organización que adoptan los coloides, lo que nos ha motivado en la tercera sección del capítulo a llevar a cabo un estudio computacional sistemático de cómo los distintos balances entre las fuerzas viscosa, magnética y gravitacional afectan a la forma de una hilera de coloides, permitiéndonos identificar cuatro estructuras básicas para hileras alineadas en la dirección del movimiento y las condiciones en las que aparecen.

Siguiendo el hilo del capítulo anterior, en el último capítulo dedicado a los coloides magnéticos hemos estudiado de manera más explícita su autoorganización, partiendo de suspensiones desordenadas de coloides. De nuevo, el estudio ha sido llevado a cabo computacionalmente, aunque a diferencia del capítulo anterior, el análisis de los resultados ha sido más cuantitativo, analizando el comportamiento de varios identificadores estadísticos que nos permiten estudiar la morfología de los agregados que se forman en el sistema, en función de los balances de fuerzas que introdujimos con anterioridad.

En el último capítulo de la tesis, cambiamos el sistema físico a tratar por nadadores Janus. Las partículas Janus se caracterizan por tener dos caras con propiedades químicas y físicas diferenciadas. Esto da lugar a que el potencial de interacción entre ellas no sea isótropo, sino que dependa de la orientación relativa de sus caras. El otro ingrediente del sistema es el método de autopropulsión de las partículas, que hemos modelizado empleando el modelo de squirmer [Lighthill, 1951, Blake, 1971]. Este modelo, basado en sistemas biológicos (células ciliadas), describe el flujo creado por tales nadadores en su desplazamiento, el cual, como ya hemos visto con anterioridad, tiene un efecto sobre sus vecinos. Hemos llevado a cabo un estudio computacional bastante completo, analizando el efecto de parámetros como el balance entre interacciones entre partículas y fuerzas viscosas, el rango de interacción entre partículas y el signo de esta interacción (considerando que las partículas se desplazan siempre con un parche en su parte delantera, la preferencia que tienen los parches por atraerse o repelerse) a la autoorganización de estos sistemas, permitiéndonos identificar seis estructuras que presentan algún tipo de orden intrínseco.

Appendices

Appendix A

Finite size effects in worm simulations

We can check whether the discrepancies between theory and simulation observed in figures 3.1 and 3.2 are due to simulation finite size effects and/or which share of responsibility they hold. We run our tests for an individual particle. To account the effect of periodic boundary conditions, we consider the colloid will displace with the velocity of a worm (equation (3.4)) of three particles separated $\Delta' = L_x$. In a first level of correction, we can account the effect of the upper wall by subtracting to the velocity of an individual colloid (equation I haven't written it yet) the velocity of a colloid at height $h' = L_z - h$. Going a level up, we could consider to actually subtract the velocity of a worm of three particles separated $\Delta' = L_x$ and at height $h' = L_z - h$. All these contributions are showcased in figure A.1 and accounted in equation (A.1).

$$\begin{aligned} v_0 = \frac{\omega a^5}{8h^4}\left(1 + 2\theta_-^2\left[\frac{4\epsilon_-^2}{(1+\epsilon_-^2)^{5/2}} + \frac{8\epsilon_-^2}{(1+4\epsilon_-^2)^{5/2}}\right]\right) \\ -\frac{\omega a^5}{8(L_z-h)^4}\left(1 + 2\theta_+^2\left[\frac{4\epsilon_+^2}{(1+\epsilon_+^2)^{5/2}} + \frac{8\epsilon_+^2}{(1+4\epsilon_+^2)^{5/2}}\right]\right) \end{aligned} \tag{A.1}$$

with $\epsilon_- = \frac{L_x}{2h}$, $\epsilon_+ = \frac{L_x}{2(L_z-h)}$, $\theta_- = \frac{h}{a}$ and $\theta_+ = \frac{L_z-h}{a}$.

In order to test the importance of finite size effects, we measure in LB simulations the translational velocity of an isolated colloid of nominal radius $a = 3.7$ in a fluid of viscosity $\eta = 0.5$ (thus the hydrodynamic radius becomes $a_h = 3.41$) rotating with angular velocity $\omega = 0.002$ at several heights and for several system sizes. In figure 4.4 we compute the obtained velocity and compare it to equations (3.2) and (A.1).

A system of size $40\times40\times40$ (panel (a)) is roughly $\sim 10a$ in all its dimensions, thus it should serve as the more extreme case in which finite size effects can play a relevant role. The velocity decay with h we find with LB is stopped at height $\sim 2a$. The finite size correction partly captures this fact, but its prediction still lies in between the simulation results and the isolated far-field theory of

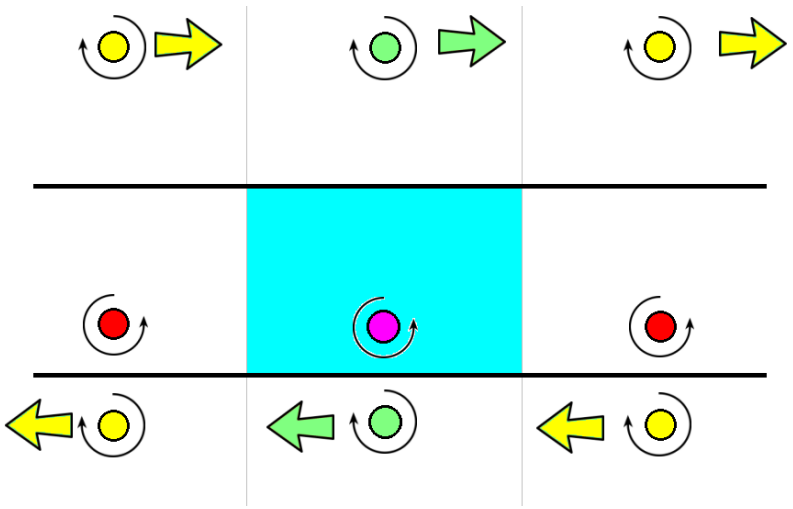

Figure A.1: Schematic view of the simulated system (cyan background) and its images, due to the presence of walls (green circles), periodic boundary conditions in the x direction (red circles), and their corresponding images due to walls (yellow circles). The contribution of each image to the velocity of the particle is represented with a solid arrow indicating its sign.

equation (3.2). In panels (d) and (g) we test cubic systems of bigger size. At these sizes the finite size correction is practically indistinguishable from the isolated theory, although the discrepancies with LB simulations are also reduced. Curiously, they do not decay linearly with height, as $h = 5.5$ is always the value in which we find a greater reduction of velocity respect theory. For the cubic system of side 80, the LB velocity becomes larger than the prediction at heights greater than $2a$.

The elongated shape of worms could motivate the use simulation boxes with L_x greater than the other sides. We test this scenario in panels (c) and (f), with systems of size $80 \times 40 \times 40$ and $160 \times 80 \times 80$. We find two results that repeat from previous cases: the corrections included due to finite size effects are not enough to recover the observed discrepancies, and the height that presents a greater divergence is $h = 5.5$. The results do not improve substantially in the greater system.

Finally, in case we thought of using a simulation box with a greater height to further the upper wall as much as possible, panel (b) proves this is ill-advised when working with small system sizes, as particles far from the lower wall actually displace much faster than the theoretical prediction, when the finite size effect correction suggests (3.2) should be an overestimation of the velocity. Not only that, but after $h \approx 2a$, the velocity does not only decay slower nor saturate, but actually increases with height! A similar effect, although less dramatic, as velocity at least does not increase with h, is observed for a system box with doubled sides in panel (e).

After this analysis, finite size effects do not look the main source of discrepancy between theory and simulations. Increased friction near the wall might be a more relevant effect to explain velocity reductions at low heights, while an hypothesis to explain the increases found at higher distances from the wall is not so evident.

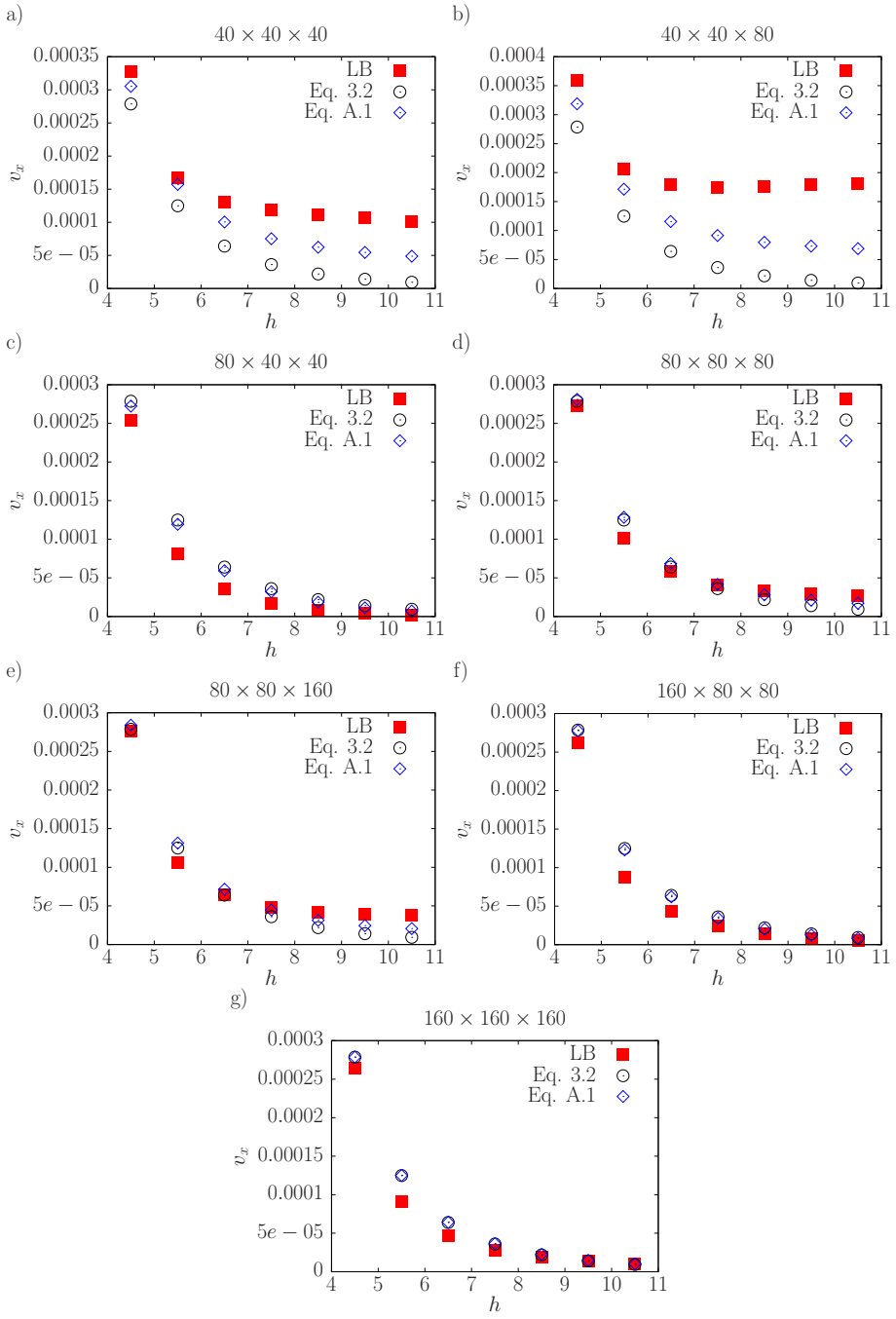

Figure A.2: Comparison of the translational velocity computed in LB (red squares), for an isolated particle given by equation (3.2) (black circles), and taking into account system finite size corrections (equation (A.1), blue diamonds) for systems of size: **(a):** $40 \times 40 \times 40$. **(b):** $40 \times 40 \times 80$. **(c):** $80 \times 40 \times 40$. **(d):** $80 \times 80 \times 80$. **(e):** $80 \times 80 \times 160$. **(f):** $160 \times 80 \times 80$. **(g):** $160 \times 160 \times 160$. All units are given in LB units.

Appendix B

Stability of bound states

In section 3.2, we conducted a linear stability analysis to study whether two purely hydrodynamically interacting rotors with angular velocities pointing in the y direction over a solid interface at $z = 0$ present a stable equilibrium point when they are aligned along the y direction.

The velocity at which each rotor displaces comes from the combination of its self-propulsion velocity (equation (3.2)) and the velocity induced by the flow created by the second particle (equation (1.24)). In section 3.2 we gave the resulting expression for two identical particles (with the same radius a and angular velocity ω) (equation (3.5)), although the results can be easily generalized to inhomogeneous particles.

$$
\begin{cases}
v_{x,CM} = \dfrac{\omega_1 a_1^5}{16(z_{CM}-z_{rel})^4} + \dfrac{\omega_2 a_2^5}{16(z_{CM}+z_{rel})^4} + \\
\quad \dfrac{\omega_2 a_2^3}{8}\left(\dfrac{3x_{rel}^2(z_{CM}-z_{rel})}{(x_{rel}^2+y_{rel}^2+z_{CM}^2)^{5/2}} - \dfrac{z_{rel}}{(x_{rel}^2+y_{rel}^2+z_{rel}^2)^{3/2}} + \dfrac{z_{rel}}{(x_{rel}^2+y_{rel}^2+z_{CM}^2)^{3/2}}\right) + \\
\quad \dfrac{\omega_1 a_1^3}{8}\left(\dfrac{3x_{rel}^2(z_{CM}+z_{rel})}{(x_{rel}^2+y_{rel}^2+z_{CM}^2)^{5/2}} + \dfrac{z_{rel}}{(x_{rel}^2+y_{rel}^2+z_{rel}^2)^{3/2}} - \dfrac{z_{rel}}{(x_{rel}^2+y_{rel}^2+z_{CM}^2)^{3/2}}\right) \\
v_{x,rel} = \dfrac{\omega_2 a_2^5}{16(z_{CM}+z_{rel})^4} - \dfrac{\omega_1 a_1^5}{16(z_{CM}-z_{rel})^4} + \\
\quad \dfrac{\omega_1 a_1^3}{8}\left(\dfrac{3x_{rel}^2(z_{CM}+z_{rel})}{(x_{rel}^2+y_{rel}^2+z_{CM}^2)^{5/2}} + \dfrac{z_{rel}}{(x_{rel}^2+y_{rel}^2+z_{rel}^2)^{3/2}} - \dfrac{z_{rel}}{(x_{rel}^2+y_{rel}^2+z_{CM}^2)^{3/2}}\right) - \\
\quad \dfrac{\omega_2 a_2^3}{8}\left(\dfrac{3x_{rel}^2(z_{CM}-z_{rel})}{(x_{rel}^2+y_{rel}^2+z_{CM}^2)^{5/2}} - \dfrac{z_{rel}}{(x_{rel}^2+y_{rel}^2+z_{rel}^2)^{3/2}} + \dfrac{z_{rel}}{(x_{rel}^2+y_{rel}^2+z_{CM}^2)^{3/2}}\right) \\
v_{y,CM} = \dfrac{3}{8}\left(\dfrac{\omega_2 a_2^3(z_{CM}-z_{rel})x_{rel}y_{rel}}{(x_{rel}^2+y_{rel}^2+z_{CM}^2)^{5/2}} + \dfrac{\omega_1 a_1^3(z_{rel}+z_{CM})x_{rel}y_{rel}}{(x_{rel}^2+y_{rel}^2+z_{CM}^2)^{5/2}}\right) \\
v_{y,rel} = \dfrac{3}{8}\left(-\dfrac{\omega_2 a_2^3(z_{CM}-z_{rel})x_{rel}y_{rel}}{(x_{rel}^2+y_{rel}^2+z_{CM}^2)^{5/2}} + \dfrac{\omega_1 a_1^3(z_{rel}+z_{CM})x_{rel}y_{rel}}{(x_{rel}^2+y_{rel}^2+z_{CM}^2)^{5/2}}\right) \\
v_{z,CM} = \dfrac{\omega_1 a_1^3}{8}\left(\dfrac{x_{rel}}{(x_{rel}^2+y_{rel}^2+z_{CM}^2)^{3/2}} - \dfrac{x_{rel}}{(x_{rel}^2+y_{rel}^2+z_{rel}^2)^{3/2}} + \dfrac{3(z_{CM}+z_{rel})x_{rel}z_{CM}}{(x_{rel}^2+y_{rel}^2+z_{CM}^2)^{5/2}}\right) + \\
\quad \dfrac{\omega_2 a_2^3}{8}\left(\dfrac{x_{rel}}{(x_{rel}^2+y_{rel}^2+z_{rel}^2)^{3/2}} - \dfrac{x_{rel}}{(x_{rel}^2+y_{rel}^2+z_{CM}^2)^{3/2}} - \dfrac{3(z_{CM}-z_{rel})x_{rel}z_{CM}}{(x_{rel}^2+y_{rel}^2+z_{CM}^2)^{5/2}}\right) \\
v_{z,rel} = \dfrac{\omega_1 a_1^3}{8}\left(\dfrac{x_{rel}}{(x_{rel}^2+y_{rel}^2+z_{CM}^2)^{3/2}} - \dfrac{x_{rel}}{(x_{rel}^2+y_{rel}^2+z_{rel}^2)^{3/2}} + \dfrac{3(z_{CM}+z_{rel})x_{rel}z_{CM}}{(x_{rel}^2+y_{rel}^2+z_{CM}^2)^{5/2}}\right) - \\
\quad \dfrac{\omega_2 a_2^3}{8}\left(\dfrac{x_{rel}}{(x_{rel}^2+y_{rel}^2+z_{rel}^2)^{3/2}} - \dfrac{x_{rel}}{(x_{rel}^2+y_{rel}^2+z_{CM}^2)^{3/2}} - \dfrac{3(z_{CM}-z_{rel})x_{rel}z_{CM}}{(x_{rel}^2+y_{rel}^2+z_{CM}^2)^{5/2}}\right)
\end{cases}
\tag{B.1}
$$

Linear stability theory applies to systems which can be described by a linear set of equations of the form $\dot{\vec{x}} = A\vec{x}$, where A is a linear operator. If all the eigenvalues of A have a negative real part, the system is linearly stable. If any of the eigenvalues of A has a positive real part, the system is unstable. If there exists any eigenvalue equal to 0, the linear stability analysis is inconclusive.

Equation (B.1) is not linear, thus it must be linearized first by taking the first term of its Taylor expansion.

$$
\dot{\vec{x}} = \dot{\vec{x}}_0 + \frac{\partial \dot{\vec{x}}}{\partial \vec{x}}(\vec{x} - \vec{x}_0) + \mathcal{O}(2) \tag{B.2}
$$

Equation (B.2) must be evaluated at the steady point where $\dot{\vec{x}}_0 = 0$. Since the self-propulsion velocity, which contributes to $v_{x,CM}$ will never be null and neither of the velocity components depends on x_{CM} and y_{CM} explicitly, it is sensible to limit the problem just to the coordinates z_{CM}, x_{rel}, y_{rel} and z_{rel}[1]. We are interested in evaluating steady points with $x_{rel} = 0$, *i.e.* both particles

[1] This also justifies working with this choice of coordinates.

are aligned along the y direction.

For identical particles, $z_{rel} = 0$ and y_{rel} and z_{CM} can take any value. There are two null eigenvalues and two pure imaginary eigenvalues, therefore the stability of the configuration cannot be inferred from linear stability analysis.

We introduce inhomogeneities by considering the particles can rotate with different angular velocities, while keeping $a_1 = a_2$ for both of them. In this case, there are additional constraints to the values the other coordinates can take. As an illustrative case, we have analyzed the linear stability for a system with $\omega_2 = 2\omega_1$. By construction, $|z_{rel}| < z_{CM}$. We arbitrarily fix $z_{CM} = 2a$ and compute the relation $y_{rel}(z_{rel})$ for steady points. For those relative heights that admit a steady solution, we compute the eigenvalues of the linearized matrix that describes the system to test its stability. The results are shown in figure B.1.

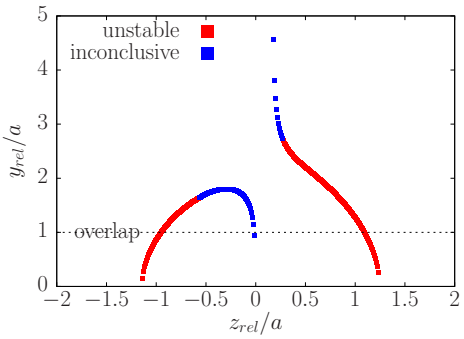

Figure B.1: Coordinate y_{rel} as a function of z_{rel} for steady points with $\omega_2 = 2\omega_1$, $z_{CM} = 2a$ and $x_{rel} = 0$. Unstable configurations are plotted in red, those whose stability cannot be determined by linear analysis in blue. Line $y_{rel} = a$ marks the situation in which there would be particle overlap.

There is a subset of steady configurations, represented as red dots, which present a positive real value, thus are unstable. Blue points correspond to null and purely imaginary eigenvalues, from which we cannot tell the stability of the configuration. However, introducing particle inhomogeneities to our simple hydrodynamic model we can justify the finite life of hydrodynamically bound states without recurring to physical elements we could have neglected in the theory.

Appendix C

Identifying clusters in suspensions

In chapters 4 and 5 we identified aggregates or clusters of particles based on a distance criterion: if a particle was at distance $d < r_{cl}$, where r_{cl} is a threshold distance, from any particle belonging to a cluster, it also belongs to that cluster. The choice of r_{cl} was not arbitrary. We computed the radial distribution function $g(r)$ and looked for the position of the first minimum after the maximum. To illustrate the procedure, we show the details on how we did it for chapter 5.

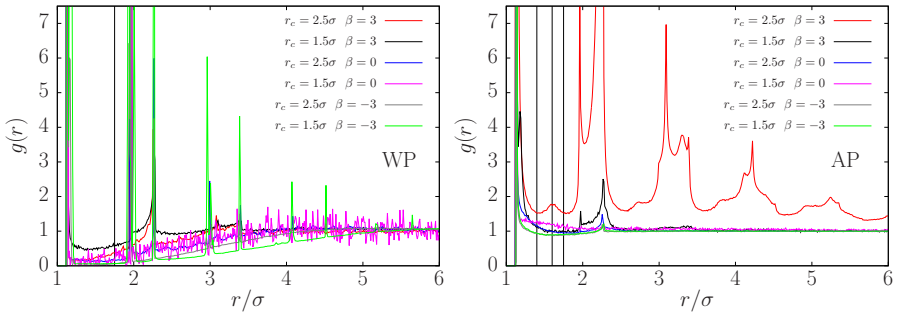

Figure C.1: Radial distribution functions $g(r)$ with $\xi = 1$ for WP swimmers (left) and AP swimmers (right).

Even if $g(r)$ are pretty similar from case to case, they do not necessarily have to share the same minimum position. Usually, taking the highest value will be the most conservative choice, although in this case we observe a small peak at $r = 1.6\sigma$ for $\beta = 3$ with $r_c = 2.5\sigma$ for AP swimmers. In this chapter, we took $r_{cl} = 1.75\sigma$ for all cases, although this choice might be wrong for this particular case. We show in figure C.2 how the computed mean cluster size and cluster size distribution vary for this troublesome case with the choice of r_{cl}, by comparing the choice of $r_{cl} = 1.75\sigma$ to cut-offs of $r_{cl} = 1.6\sigma$ and $r_{cl} = 1.4\sigma$, marked with vertical lines in figure C.1.

We observe that as we reduce r_{cl}, the mean cluster size is reduced, being

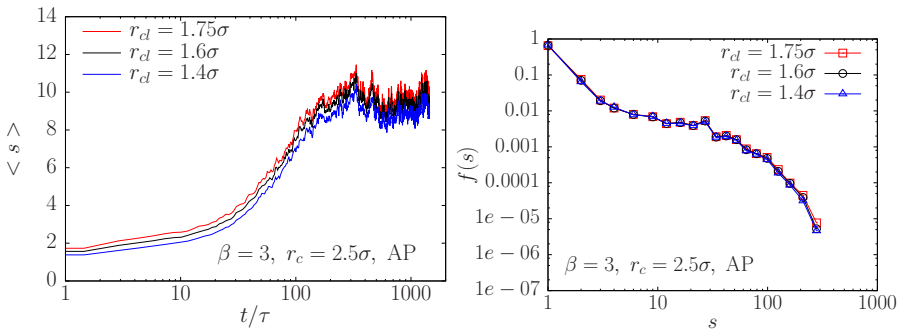

Figure C.2: Left: time evolution of the mean cluster size. Right: cluster size distribution.

the difference between $r_{cl} = 1.75\sigma$ and $r_{cl} = 1.4\sigma$ of 0.9 units ($\approx 10\%$). As for the cluster size distribution, we find that all three of them are very similar. Even if the frequencies for the largest observed clusters are reduced with r_{cl}, all distributions are cut at the same bin (clusters sized between 240 and 318 particles), with a frequency $7.7 \cdot 10^{-6}$ for $s = 279$ and $r_{cl} = 1.75\sigma$, and $4.6 \cdot 10^{-6}$ for the same size with $r_{cl} = 1.4\sigma$. The monomer frequency goes from 0.680 for $r_{cl} = 1.4\sigma$ to 0.656 for $r_{cl} = 1.75\sigma$, and all three curves have a very similar shape, sharing even local maxima and minima along the whole profile.

In chapter 4 we used a similar procedure to choose $r_{cl} = 2.65a$.

Bibliography

[Agayan et al., 2008] Agayan, R. R., Smith, R. G., and Kopelman, R. (2008). Slipping friction of an optically and magnetically manipulated microsphere rolling at a glass-water interface. *Journal of Applied Physics*, 104(5):054915.

[Alarcón and Pagonabarraga, 2013] Alarcón, F. and Pagonabarraga, I. (2013). Spontaneous aggregation and global polar ordering in squirmer suspensions. *Journal of Molecular Liquids*, 185:56 – 61. Molecular Simulations of Complex Systems.

[Alarcón et al., 2017] Alarcón, F., Valeriani, C., and Pagonabarraga, I. (2017). Morphology of clusters of attractive dry and wet self-propelled spherical particle suspensions. *Soft Matter*, 13:814–826.

[Alder and Wainwright, 1970] Alder, B. J. and Wainwright, T. E. (1970). Decay of the Velocity Autocorrelation Function. *Phys. Rev. A*, 1:18–21.

[Allan and Mason, 1962] Allan, R. S. and Mason, S. G. (1962). Particle behaviour in shear and electric fields i. deformation and burst of fluid drops. *Proceedings of the Royal Society of London A: Mathematical, Physical and Engineering Sciences*, 267(1328):45–61.

[Aranson, 2013] Aranson, I. S. (2013). Collective behavior in out-of-equilibrium colloidal suspensions. *Comptes Rendus Physique*, 14(6):518 – 527. Living fluids / Fluides vivants.

[Aranson and Tsimring, 2006] Aranson, I. S. and Tsimring, L. S. (2006). Theory of self-assembly of microtubules and motors. *Phys. Rev. E*, 74:031915.

[Avron et al., 2005] Avron, J. E., Kenneth, O., and Oaknin, D. H. (2005). Pushmepullyou: an efficient micro-swimmer. *New Journal of Physics*, 7(1):234.

[Bacri et al., 1995] Bacri, J., Cebers, A., Lacis, S., and Perzynski, R. (1995). Dynamics of a magnetic fluid droplet in a rotating field. *Journal of Magnetism and Magnetic Materials*, 149(1):143 – 147. Proceedings of the Seventh International Conference on Magnetic Fluids.

[Berg, 2002] Berg, H. C. (2002). How spiroplasma might swim. *Journal of Bacteriology*, 184(8):2063–2064.

[Bhatnagar et al., 1954] Bhatnagar, P. L., Gross, E. P., and Krook, M. (1954). A model for collision processes in gases. i. small amplitude processes in charged and neutral one-component systems. *Phys. Rev.*, 94:511–525.

[Blake, 1971] Blake, J. R. (1971). A spherical envelope approach to ciliary propulsion. *Journal of Fluid Mechanics*, 46(1):199–208.

[Blake and Chwang, 1974] Blake, J. R. and Chwang, A. T. (1974). Fundamental singularities of viscous flow. *Journal of Engineering Mathematics*, 8(1):23–29.

[Blaschke et al., 2016] Blaschke, J., Maurer, M., Menon, K., Zottl, A., and Stark, H. (2016). Phase separation and coexistence of hydrodynamically interacting microswimmers. *Soft Matter*, 12:9821–9831.

[Blickle et al., 2005] Blickle, V., Babič, D., and Bechinger, C. (2005). Evanescent light scattering with magnetic colloids. *Applied Physics Letters*, 87(10):101102.

[Bruus, 2012] Bruus, H. (2012). Acoustofluidics 7: The acoustic radiation force on small particles. *Lab Chip*, 12:1014–1021.

[Cates et al., 2004] Cates, M. E., Stratford, K., Adhikari, R., Stansell, P., Desplat, J.-C., Pagonabarraga, I., and Wagner, A. J. (2004). Simulating colloid hydrodynamics with lattice boltzmann methods. *Journal of Physics: Condensed Matter*, 16(38):S3903.

[Cates and Tailleur, 2015] Cates, M. E. and Tailleur, J. (2015). Motility-induced phase separation. *Annual Review of Condensed Matter Physics*, 6(1):219–244.

[Cisneros et al., 2007] Cisneros, L., Cortez, R., Dombrowski, C., Goldstein, R. E., and Kessler, J. O. (2007). Fluid dynamics of self-propelled microorganisms, from individuals to concentrated populations. *Exp. Fluids*, 43:737–753.

[Delmotte et al., 2015] Delmotte, B., Keaveny, E. E., Plouraboué, F., and Climent, E. (2015). Large-scale simulation of steady and time-dependent active suspensions with the force-coupling method. *J. Comput. Phys.*, 302(C):524–547.

[Deseigne et al., 2010] Deseigne, J., Dauchot, O., and Chaté, H. (2010). Collective motion of vibrated polar disks. *Phys. Rev. Lett.*, 105:098001.

[Desplat et al., 2001] Desplat, J.-C., Pagonabarraga, I., and Bladon, P. (2001). Ludwig: A parallel lattice-boltzmann code for complex fluids. *Computer Physics Communications*, 134(3):273 – 290.

[Dombrowski et al., 2004] Dombrowski, C., Cisneros, L., Chatkaew, S., Goldstein, R. E., and Kessler, J. O. (2004). Self-concentration and large-scale coherence in bacterial dynamics. *Phys. Rev. Lett.*, 93:098103.

[Drescher et al., 2011] Drescher, K., Dunkel, J., Cisneros, L. H., Ganguly, S., and Goldstein, R. E. (2011). Fluid dynamics and noise in bacterial cell–cell and cell–surface scattering. *Proceedings of the National Academy of Sciences*, 108(27):10940–10945.

[Dreyfus et al., 2005] Dreyfus, R., Baudry, J., L Roper, M., Fermigier, M., A Stone, H., and Bibette, J. (2005). Microscopic artificial swimmers. *Nature*, 437:862–5.

[Eppenga and Frenkel, 1984] Eppenga, R. and Frenkel, D. (1984). Monte carlo study of the isotropic and nematic phases of infinitely thin hard platelets. *Molecular Physics*, 52(6):1303–1334.

[Ermak and McCammon, 1978] Ermak, D. L. and McCammon, J. A. (1978). Brownian dynamics with hydrodynamic interactions. *The Journal of Chemical Physics*, 69(4):1352–1360.

[Español and Warren, 1995] Español, P. and Warren, P. (1995). Statistical mechanics of dissipative particle dynamics. *EPL (Europhysics Letters)*, 30(4):191.

[Evans et al., 2011] Evans, A. A., Ishikawa, T., Yamaguchi, T., and Lauga, E. (2011). Orientational order in concentrated suspensions of spherical microswimmers. *Physics of Fluids*, 23(11):111702.

[Frisch et al., 1987] Frisch, U., D'Humières, D., Hasslacher, B., Lallemand, P., Pomeau, Y., and P. Rivet, J. (1987). Lattice gas hydrodynamics in two and three dimensions. *Complex Systems*, 1.

[Frisch et al., 1986] Frisch, U., Hasslacher, B., and Pomeau, Y. (1986). Lattice-gas automata for the navier-stokes equation. *Phys. Rev. Lett.*, 56:1505–1508.

[Gor'kov, 1962] Gor'kov, L. P. (1962). On the Forces Acting on a Small Particle in an Acoustical Field in an Ideal Fluid. *Soviet Physics Doklady*, 6:773.

[Groot and Warren, 1997] Groot, R. D. and Warren, P. B. (1997). Dissipative particle dynamics: Bridging the gap between atomistic and mesoscopic simulation. *The Journal of Chemical Physics*, 107(11):4423–4435.

[Hardy et al., 1973] Hardy, J., Pomeau, Y., and de Pazzis, O. (1973). Time evolution of a two dimensional model system. i. invariant states and time correlation functions. *Journal of Mathematical Physics*, 14(12):1746–1759.

[Helgesen et al., 1990] Helgesen, G., Pieranski, P., and Skjeltorp, A. T. (1990). Nonlinear phenomena in systems of magnetic holes. *Physical Review Letters*, 64:1425–1428.

[Higuera and Jiménez, 1989] Higuera, F. J. and Jiménez, J. (1989). Boltzmann approach to lattice gas simulations. *Europhys. Lett.*, 9:663.

[Higuera et al., 1989] Higuera, F. J., Succi, S., and Benzi, R. (1989). Lattice gas dynamics with enhanced collisions. *EPL (Europhysics Letters)*, 9(4):345.

[Hong et al., 2008] Hong, L., Cacciuto, A., Luijten, E., and Granick, S. (2008). Clusters of amphiphilic colloidal spheres. *Langmuir*, 24(3):621–625. PMID: 18181655.

[Hoogerbrugge and Koelman, 1992] Hoogerbrugge, P. J. and Koelman, J. M. V. A. (1992). Simulating microscopic hydrodynamic phenomena with dissipative particle dynamics. *EPL (Europhysics Letters)*, 19(3):155.

[Howse et al., 2007] Howse, J. R., Jones, R. A. L., Ryan, A. J., Gough, T., Vafabakhsh, R., and Golestanian, R. (2007). Self-motile colloidal particles: From directed propulsion to random walk. *Phys. Rev. Lett.*, 99:048102.

[Ishikawa et al., 2008] Ishikawa, T., Locsei, J. T., and Pedley, T. J. (2008). Development of coherent structures in concentrated suspensions of swimming model micro-organisms. *Journal of Fluid Mechanics*, 615:401–431.

[Ishikawa and Pedley, 2007] Ishikawa, T. and Pedley, T. J. (2007). Diffusion of swimming model micro-organisms in a semi-dilute suspension. *Journal of Fluid Mechanics*, 588:437–462.

[Ishikawa and Pedley, 2008] Ishikawa, T. and Pedley, T. J. (2008). Coherent structures in monolayers of swimming particles. *Phys. Rev. Lett.*, 100:088103.

[Ishikawa et al., 2006] Ishikawa, T., Simmonds, M. P., and Pedley, T. J. (2006). Hydrodynamic interaction of two swimming model micro-organisms. *Journal of Fluid Mechanics*, 568:119–160.

[J. Pedley, 2016] J. Pedley, T. (2016). Spherical squirmers: Models for swimming micro-organisms. *IMA Journal of Applied Mathematics*, 81:hxw030.

[Janssen et al., 2009] Janssen, X., Schellekens, A., van Ommering, K., van IJzendoorn, L., and Prins, M. (2009). Controlled torque on superparamagnetic beads for functional biosensors. *Biosensors and Bioelectronics*, 24(7):1937 – 1941.

[King, 1934] King, L. V. (1934). On the acoustic radiation pressure on spheres. *Proceedings of the Royal Society of London A: Mathematical, Physical and Engineering Sciences*, 147(861):212–240.

[Klingenberg et al., 2007] Klingenberg, D. J., Ulicny, J. C., and Golden, M. A. (2007). Mason numbers for magnetorheology. *Journal of Rheology*, 51(5):883–893.

[Kudrolli et al., 2008] Kudrolli, A., Lumay, G., Volfson, D., and Tsimring, L. S. (2008). Swarming and swirling in self-propelled polar granular rods. *Phys. Rev. Lett.*, 100:058001.

[Kumacheva et al., 2003] Kumacheva, E., Garstecki, P., Wu, H., and Whitesides, G. M. (2003). Two–dimensional colloid crystals obtained by coupling of flow and confinement. *Phys. Rev. Lett.*, 91:128301.

[Kyoya et al., 2015] Kyoya, K., Matsunaga, D., Imai, Y., Omori, T., and Ishikawa, T. (2015). Shape matters: Near-field fluid mechanics dominate the collective motions of ellipsoidal squirmers. *Phys. Rev. E*, 92:063027.

[Ladd and Verberg, 2001] Ladd, A. and Verberg, R. (2001). Lattice boltzmann simulations of particle-fluid suspensions. *Journal of Statistical Physics*, 104:1191.

[Ladd, 1994a] Ladd, A. J. C. (1994a). Numerical simulations of particulate suspensions via a discretized boltzmann equation. part 1. theoretical foundation. *Journal of Fluid Mechanics*, 271:285–309.

[Ladd, 1994b] Ladd, A. J. C. (1994b). Numerical simulations of particulate suspensions via a discretized boltzmann equation. part 2. numerical results. *Journal of Fluid Mechanics*, 271:311.

[Lighthill, 1951] Lighthill, M. J. (1951). On the squirming motion of nearly spherical deformable bodies through liquids at very small reynolds numbers. *Communications on Pure and Applied Mathematics*, 5(2):109–118.

[Liverpool, 2003] Liverpool, T. B. (2003). Anomalous fluctuations of active polar filaments. *Phys. Rev. E*, 67:031909.

[Llopis, 2010] Llopis, I. (2010). *Hydrodynamic cooperativity in microswimmer suspensions*. PhD thesis, Universitat de Barcelona.

[Llopis and Pagonabarraga, 2006] Llopis, I. and Pagonabarraga, I. (2006). Dynamic regimes of hydrodynamically coupled self-propelling particles. *EPL (Europhysics Letters)*, 75(6):999.

[Llopis and Pagonabarraga, 2010] Llopis, I. and Pagonabarraga, I. (2010). Hydrodynamic interactions in squirmer motion: Swimming with a neighbour and close to a wall. *Journal of Non-Newtonian Fluid Mechanics*, 165(17):946 – 952. Proceedings of the 5th International Workshop on Non-Equilibrium Thermodynamics IWNET 2009.

[Lowe et al., 1995] Lowe, C. P., Frenkel, D., and Masters, A. J. (1995). Long time tails in angular momentum correlations. *The Journal of Chemical Physics*, 103(4):1582–1587.

[Mallory et al., 2017] Mallory, S. A., Alarcón, F., Cacciuto, A., and Valeriani, C. (2017). Self-assembly of active amphiphilic janus particles. *New Journal of Physics*, 19(12):125014.

[Marchetti et al., 2013] Marchetti, M. C., Joanny, J. F., Ramaswamy, S., Liverpool, T. B., Prost, J., Rao, M., and Simha, R. A. (2013). Hydrodynamics of soft active matter. *Rev. Mod. Phys.*, 85:1143–1189.

[Martinez-Pedrero et al., 2018] Martinez-Pedrero, F., Navarro-Argemí, E., Ortiz-Ambriz, A., Pagonabarraga, I., and Tierno, P. (2018). Emergent hydrodynamic bound states between magnetically powered micropropellers. *Science Advances*, 4(1).

[Martinez-Pedrero et al., 2015] Martinez-Pedrero, F., Ortiz-Ambriz, A., Pagonabarraga, I., and Tierno, P. (2015). Colloidal microworms propelling via a cooperative hydrodynamic conveyor belt. *Phys. Rev. Lett.*, 115:138301.

[Massana-Cid et al., 2017] Massana-Cid, H., Martinez-Pedrero, F., Navarro-Argemí, E., Pagonabarraga, I., and Tierno, P. (2017). Propulsion and hydrodynamic particle transport of magnetically twisted colloidal ribbons. *New Journal of Physics*, 19(10):103031.

[Matas-Navarro et al., 2014] Matas-Navarro, R., Golestanian, R., Liverpool, T. B., and Fielding, S. M. (2014). Hydrodynamic suppression of phase separation in active suspensions. *Phys. Rev. E*, 90:032304.

[McNamara and Zanetti, 1988] McNamara, G. R. and Zanetti, G. (1988). Use of the boltzmann equation to simulate lattice-gas automata. *Phys. Rev. Lett.*, 61:2332–2335.

[Melle et al., 2003] Melle, S., Calderón, O. G., Rubio, M. A., and Fuller, G. G. (2003). Microstructure evolution in magnetorheological suspensions governed by mason number. *Phys. Rev. E*, 68:041503.

[Metropolis et al., 1953] Metropolis, N., Rosenbluth, A. W., Rosenbluth, M. N., Teller, A. H., and Teller, E. (1953). Equation of State Calculations by Fast Computing Machines. *Journal of Chemical Physics*, 21:1087–1092.

[Molina et al., 2013] Molina, J. J., Nakayama, Y., and Yamamoto, R. (2013). Hydrodynamic interactions of self-propelled swimmers. *Soft Matter*, 9:4923–4936.

[Morimoto et al., 2008] Morimoto, H., Ukai, T., Nagaoka, Y., Grobert, N., and Maekawa, T. (2008). Tumbling motion of magnetic particles on a magnetic substrate induced by a rotational magnetic field. *Phys. Rev. E*, 78:021403.

[Najafi and Golestanian, 2004] Najafi, A. and Golestanian, R. (2004). Simple swimmer at low reynolds number: Three linked spheres. *Physical review E*, 69:062901.

[Narayan et al., 2007] Narayan, V., Ramaswamy, S., and Menon, N. (2007). Long-lived giant number fluctuations in a swarming granular nematic. *Science*, 317(5834):105–108.

[Néel, 1949] Néel, L. (1949). Théorie du traînage magnétique des ferromagnétiques en grains fins avec application aux terres cuites. *Annales de Géophysique*, 5:99–136.

[Nguyen and Ladd, 2002] Nguyen, N.-Q. and Ladd, A. J. C. (2002). Lubrication corrections for lattice-boltzmann simulations of particle suspensions. *Phys. Rev. E*, 66:046708.

[Osterman et al., 2009] Osterman, N., Poberaj, I., Dobnikar, J., Frenkel, D., Ziherl, P., and Babić, D. (2009). Field-induced self-assembly of suspended colloidal membranes. *Phys. Rev. Lett.*, 103:228301.

[Oyama et al., 2016] Oyama, N., Molina, J. J., and Yamamoto, R. (2016). Purely hydrodynamic origin for swarming of swimming particles. *Phys. Rev. E*, 93:043114.

[Oyama et al., 2017] Oyama, N., Molina, J. J., and Yamamoto, R. (2017). Simulations of model microswimmers with fully resolved hydrodynamics. *Journal of the Physical Society of Japan*, 86(10):101008.

[P. Allen and J. Tildesley, 1989] P. Allen, M. and J. Tildesley, D. (1989). *Computer Simuation of Liquids*. Oxford University Press.

[Pagonabarraga and Llopis, 2013] Pagonabarraga, I. and Llopis, I. (2013). The structure and rheology of sheared model swimmer suspensions. *Soft Matter*, 9:7174–7184.

[Palacci et al., 2013] Palacci, J., Sacanna, S., Steinberg, A. P., Pine, D. J., and Chaikin, P. M. (2013). Living crystals of light-activated colloidal surfers. *Science*, 339(6122):936–940.

[Paxton et al., 2006] Paxton, W. F., Baker, P. T., Kline, T. R., Wang, Y., Mallouk, T. E., and Sen, A. (2006). Catalytically induced electrokinetics for motors and micropumps. *Journal of the American Chemical Society*, 128(46):14881–14888.

[Paxton et al., 2004] Paxton, W. F., Kistler, K. C., Olmeda, C. C., Sen, A., St. Angelo, S. K., Cao, Y., Mallouk, T. E., Lammert, P. E., and Crespi, V. H. (2004). Catalytic nanomotors: Autonomous movement of striped nanorods. *ChemInform*, 35(52).

[Petroff et al., 2015] Petroff, A. P., Wu, X.-L., and Libchaber, A. (2015). Fast-moving bacteria self-organize into active two-dimensional crystals of rotating cells. *Phys. Rev. Lett.*, 114:158102.

[Purcell, 1977] Purcell, E. M. (1977). Life at low reynolds number. *American Journal of Physics*, 45(1):3–11.

[Qian et al., 1992] Qian, Y. H., D'Humières, D., and Lallemand, P. (1992). Lattice bgk models for navier-stokes equation. *EPL (Europhysics Letters)*, 17(6):479.

[Ramaswamy et al., 2003] Ramaswamy, S., Simha, R. A., and Toner, J. (2003). Active nematics on a substrate: Giant number fluctuations and long-time tails. *EPL (Europhysics Letters)*, 62(2):196.

[Romanczuk et al., 2012] Romanczuk, P., Bär, M., Ebeling, W., Lindner, B., and Schimansky-Geier, L. (2012). Active brownian particles. *The European Physical Journal Special Topics*, 202(1):1–162.

[Schnitzer, 1993] Schnitzer, M. J. (1993). Theory of continuum random walks and application to chemotaxis. *Phys. Rev. E*, 48:2553–2568.

[Schwarz-Linek et al., 2012] Schwarz-Linek, J., Valeriani, C., Cacciuto, A., Cates, M. E., Marenduzzo, D., Morozov, A. N., and Poon, W. C. K. (2012). Phase separation and rotor self-assembly in active particle suspensions. *Proceedings of the National Academy of Sciences*, 109(11):4052–4057.

[Settnes and Bruus, 2012] Settnes, M. and Bruus, H. (2012). Forces acting on a small particle in an acoustical field in a viscous fluid. *Phys. Rev. E*, 85:016327.

[Sing et al., 2010] Sing, C. E., Schmid, L., Schneider, M. F., Franke, T., and Alexander-Katz, A. (2010). Controlled surface-induced flows from the motion of self-assembled colloidal walkers. *Proceedings of the National Academy of Sciences*, 107(2):535–540.

[Snezhko and Aranson, 2011] Snezhko, A. and Aranson, I. S. (2011). Magnetic manipulation of self-assembled colloidal asters. *Nature Materials*, 10:698.

[Snezhko et al., 2005] Snezhko, A., Aranson, I. S., and Kwok, W.-K. (2005). Structure formation in electromagnetically driven granular media. *Phys. Rev. Lett.*, 94:108002.

[Solon et al., 2015a] Solon, A. P., Fily, Y., Baskaran, A., Cates, M. E., Kafri, Y., Kardar, M., and Tailleur, J. (2015a). Pressure is not a state function for generic active?fluids. *Nature Physics*, 11:673 EP –. Article.

[Solon et al., 2015b] Solon, A. P., Stenhammar, J., Wittkowski, R., Kardar, M., Kafri, Y., Cates, M. E., and Tailleur, J. (2015b). Pressure and phase equilibria in interacting active brownian spheres. *Phys. Rev. Lett.*, 114:198301.

[Stariolo and Barci, 2010] Stariolo, D. A. and Barci, D. G. (2010). Orientational order in systems with competing interactions. *Journal of Physics: Conference Series*, 246(1):012021.

[Stoddard and Ford, 1973] Stoddard, S. D. and Ford, J. (1973). Numerical experiments on the stochastic behavior of a lennard-jones gas system. *Phys. Rev. A*, 8:1504–1512.

[Stratford and Pagonabarraga, 2008] Stratford, K. and Pagonabarraga, I. (2008). Parallel simulation of particle suspensions with the lattice boltzmann method. *Computers and Mathematics with Applications*, 55(7):1585 – 1593. Mesoscopic Methods in Engineering and Science.

[Straube and Tierno, 2013] Straube, A. V. and Tierno, P. (2013). Synchronous vs. asynchronous transport of a paramagnetic particle in a modulated ratchet potential. *EPL (Europhysics Letters)*, 103(2):28001.

[Strogatz, 1994] Strogatz, S. H. (1994). *Nonlinear dynamics and chaos.* Addison-Wesley, Reading MA.

[Succi, 2001] Succi, S. (2001). *The Lattice Boltzmann Equation: For Fluid Dynamics and Beyond*. Oxford University Press.

[Takatori and Brady, 2015] Takatori, S. C. and Brady, J. F. (2015). Towards a thermodynamics of active matter. *Phys. Rev. E*, 91:032117.

[Takatori et al., 2014] Takatori, S. C., Yan, W., and Brady, J. F. (2014). Swim pressure: Stress generation in active matter. *Physical Review Letters*, 113:028103.

[Taylor, 1951] Taylor, G. I. (1951). Analysis of the swimming of microscopic organisms. *Proceedings of the Royal Society of London A: Mathematical, Physical and Engineering Sciences*, 209(1099):447–461.

[Theers et al., 2016] Theers, M., Westphal, E., Gompper, G., and Winkler, R. G. (2016). Modeling a spheroidal microswimmer and cooperative swimming in a narrow slit. *Soft Matter*, 12:7372–7385.

[Theurkauff et al., 2012] Theurkauff, I., Cottin-Bizonne, C., Palacci, J., Ybert, C., and Bocquet, L. (2012). Dynamic clustering in active colloidal suspensions with chemical signaling. *Phys. Rev. Lett.*, 108:268303.

[Thutupalli et al., 2011] Thutupalli, S., Seemann, R., and Herminghaus, S. (2011). Swarming behavior of simple model squirmers. *New Journal of Physics*, 13(7):073021.

[Tierno, 2014] Tierno, P. (2014). Recent advances in anisotropic magnetic colloids: realization, assembly and applications. *Phys. Chem. Chem. Phys.*, 16:23515–23528.

[Tierno et al., 2008] Tierno, P., Golestanian, R., Pagonabarraga, I., and Sagués, F. (2008). Magnetically actuated colloidal microswimmers. *The Journal of Physical Chemistry B*, 112(51):16525–16528.

[Toner and Tu, 1998] Toner, J. and Tu, Y. (1998). Flocks, herds, and schools: A quantitative theory of flocking. *Phys. Rev. E*, 58:4828–4858.

[Valeriani et al., 2012] Valeriani, C., Sanz, E., Pusey, P. N., Poon, W. C. K., Cates, M. E., and Zaccarelli, E. (2012). From compact to fractal crystalline clusters in concentrated systems of monodisperse hard spheres. *Soft Matter*, 8:4960–4970.

[Vicsek et al., 1995] Vicsek, T., Czirók, A., Ben-Jacob, E., Cohen, I., and Shochet, O. (1995). Novel type of phase transition in a system of self-driven particles. *Phys. Rev. Lett.*, 75:1226–1229.

[Vicsek and Zafeiris, 2012] Vicsek, T. and Zafeiris, A. (2012). Collective motion. *Physics Reports*, 517(3):71 – 140. Collective motion.

[Winkler et al., 2015] Winkler, R. G., Wysocki, A., and Gompper, G. (2015). Virial pressure in systems of spherical active brownian particles. *Soft Matter*, 11:6680–6691.

[Wolgemuth et al., 2002] Wolgemuth, C., Hoiczyk, H., Kaizer, D., and Oster, G. (2002). How myxobacteria glide. *Current Biology*, 12:369–377.

[Yamada et al., 2003] Yamada, D., Hondou, T., and Sano, M. (2003). Coherent dynamics of an asymmetric particle in a vertically vibrating bed. *Phys. Rev. E*, 67:040301.

[Yellen et al., 2007] Yellen, B. B., Erb, R. M., Son, H. S., Hewlin, Jr., R., Shang, H., and Lee, G. U. (2007). Traveling wave magnetophoresis for high resolution chip based separations. *Lab Chip*, 7:1681–1688.

[Yosioka and Kawasima, 1955] Yosioka, K. and Kawasima, Y. (1955). Acoustic radiation pressure on a compressible sphere. *Acta Acustica united with Acustica*, 5(3):167–173.

[Zerrouki et al., 2008] Zerrouki, D., Baudry, J., Pine, D., Chaikin, P., and Bibette, J. (2008). Chiral colloidal clusters. *Nature*, 455(7211):380–382.

[Zöttl and Stark, 2014] Zöttl, A. and Stark, H. (2014). Hydrodynamics determines collective motion and phase behavior of active colloids in quasi-two-dimensional confinement. *Phys. Rev. Lett.*, 112:118101.